UNIVERSITY FOR DEVELOPMENT STUDIES

DETECTION AND CHARACTERIZATION OF CLIMATE-RESILIENT MULTIPURPOSE NATIVE TREE SPECIES IN NORTHERN SAVANNA ECOLOGICAL ZONE, GHANA

FRANKLIN XAVIER DONO

2026

UNIVERSITY FOR DEVELOPMENT STUDIES

DETECTION AND CHARACTERIZATION OF CLIMATE-RESILIENT MULTIPURPOSE NATIVE TREE SPECIES IN NORTHERN SAVANNA ECOLOGICAL ZONE, GHANA

BY

FRANKLIN XAVIER DONO

(BSc. Geodetic Engineering; MBA Finance - Derivatives)

UDS/DES/0004/21

THESIS SUBMITTED TO THE DEPARTMENT OF ENVIRONMENT AND SUSTAINABILITY SCIENCE, FACULTY OF NATURAL RESOURCES AND ENVIRONMENT, UNIVERSITY FOR DEVELOPMENT STUDIES IN PARTIAL FULFILMENT OF THE REQUIREMENTS FOR THE AWARD OF DOCTOR OF PHILOSOPHY DEGREE IN ENVIRONMENTAL MANAGEMENT AND SUSTAINABILITY

MARCH 2026

DECLARATION

I hereby declare that this dissertation is the result of my own original work and that no part of it has been presented for another degree in this University or elsewhere:

Signature: ……………………………… Date: March 30, 2026
Name: Franklin Xavier Dono

Supervisors'

I hereby declare that the preparation and presentation of the dissertation/thesis was supervised in accordance with the guidelines on supervision of dissertation/thesis laid down by the University for Development Studies.

Principal Supervisor

Signature: ……………………………… Date: March 30, 2026
Name: Prof. Bernard N. Baatuuwie

Co-Supervisor

Signature: ……………………………… Date: March 30, 2026
Name: Ing. Prof. Felix K. Abagale

Co-Supervisor

Signature: Anne Mette Lykke ……………………………… Date: March 30, 2026
Name: Dr. Anne Mette Lykke

Co-Supervisor

Signature: ……………………………… Date: March 30, 2026
Name: Dr. Peter Borgen Sørensen

Head of Department

Signature: ……………………………… Date: March 30, 2026
Name: Prof. Ebenezer Owusu-Sekyere

WACWISA Director

Signature: ……………………………… WACWISA-UDS NYANKPALA, TAMALE Date: March 30, 2026
Name: Ing. Prof. Felix K. Abagale

ABSTRACT

Climate-resilient multipurpose native tree species such as *Adansonia digitata* (baobab) and *Parkia biglobosa* (African locust bean) play critical ecological and livelihood roles in Ghana. However, their sustainable utilization is constrained by limited scalable methods for fruit detection, morphological characterization, and yield estimation, which are essential for value chain development and resource management. Advances in computer vision and remote sensing offer new opportunities to address these gaps. This study develops a computer vision system to detect and characterize *Adansonia digitata* fruits from images acquired with a smartphone camera, estimate their mass, volume, and density, and categorize them by size. It also formulates the relationship between *Parkia biglobosa* pod yield, crown radius, soil, and spectral properties from drone and satellite images, while accounting for locality constraints. It further investigates the effect of interactions between variables. The smartphone-based computer vision system achieved high accuracy in detecting (97 %) and characterizing (99.8 %) *Adansonia digitata* fruits. With respect to estimating *Parkia biglobosa* pod yield, integrating drone, satellite, and soil data improved accuracy by 5 % compared to the base model, which explained 63 % of the variation in yield using crown radius alone while accounting for location. Adding interaction terms further enhanced performance by 7 %. The fruit samples were sorted and categorized by size (small, medium, and large). The results demonstrate that images from low-cost, easily accessible smartphones can be used for fruit analysis, deployable into a web application. It also highlights the importance of multi-source image data fusion for modelling the yield of native tree species. The work contributes to theoretical and methodological advancements for agroforestry management and supports digital innovations in climate-resilient native tree product value chains. The study recommends the adoption of smartphone-based tools in the *Adansonia digitata* fruit production value chain and multi-source remote sensing approaches for landscape-scale *Parkia biglobosa* pod yield estimation. Future research should explore model generalization across ecological zones and expand applications to other economically important native species in Ghana and sub-Saharan Africa.

Keywords: Remote Sensing, Machine Learning, Bayesian Statistics, Native Species, Yield

ACKNOWLEDGMENTS

My deepest gratitude is to God Almighty, whose divine guidance, strength, and wisdom have enabled me to complete this research journey. I extend my sincere appreciation to my distinguished academic supervisors: Prof. Bernard N. Baatuuwie, Ing. Prof. Felix K. Abagale, Dr. Anne Mette Lykke, and Dr. Peter Borgen Sørensen, whose scholarly expertise, unwavering support, and constructive guidance were instrumental in shaping this research. Their commitment to academic excellence has been a constant source of inspiration. I am also grateful to the academic committee members who monitored my progress and provided invaluable feedback. Their expert insights and scholarly contributions significantly enhanced the quality of this study.

I acknowledge, with deep appreciation, the West African Centre for Water, Irrigation, and Sustainable Agriculture (WACWISA), Climate Change Resilience of Ecosystem Services (CRES), University for Development Studies (UDS), and Aarhus University for their financial support, research facilities, and essential resources that facilitated this investigation. A special note of thanks to the dedicated staff at UDS, Ghana, and Aarhus University in Denmark, whose hospitality, technical expertise, and consistent support were invaluable during the study period.

This work is funded by the Ministry of Foreign Affairs of Denmark and administered by the Danida Fellowship *Centre through the Climate Change Resilience of Ecosystem Services* (CRES) Project with Grant No. DCF File No. 20- 13-GHA. I therefore extend my heartfelt gratitude for the financial support in this regard.

I also appreciate the assistance the Ghana Atomic Energy Commission (GAEC) provided, for their unwavering support and resources, which have significantly contributed to the successful completion of this study.

My special appreciation goes to my wife and children, whose patience, love, and steadfast support have been my greatest source of strength and motivation. Their presence and encouragement have made this journey even more meaningful, and to my parents and siblings, and the entire family for their selfless dedication and unwavering support throughout this journey. I am also grateful to my colleagues and friends who offered encouragement and support throughout this academic journey

DEDICATION

To my beloved wife and precious children, whose unwavering support and love have been my constant source of inspiration throughout this academic journey, and to my parents, whose enduring legacy of values and aspirations continue to guide me. Their influence endures through the principles they instilled in me, which have molded my path to success.

TABLE OF CONTENTS

LIST OF FIGURES

LIST OF TABLES

LIST OF ACRONYMS

AMMI	Additive Main Effect and Multiplicative Interactive
ACE R-CNN	Attention Complementary and Edge Detection Region-based Convolutional Neural Network
BSROC	Bayesian Summary Receiver Operating Characteristic
BD	Bulk Density
CHMs	Canopy Height Models
CEC	Cation Exchange Capacity
CCD	Charge-Coupled Device
CRES	Climate Change Resilience of Ecosystem Services
CFVO	Coarse Fragments Volumetric
CSV	Comma-Separated Value
CMOS	Complementary Metal-Oxide Semiconductor
CV	Computer vision
CRF	Conditional Random Fields
CNNs	Convolutional Neural Networks
DBNs	Deep Belief Networks
DL	Deep Learning
DETR	Detection Transformer
DBH	Diameter at Breast Height
ESRGAN	Enhanced Super-Resolution Generative Adversarial Network
FP	False Positive
FPN	Feature Pyramid Network
FCN	Fully Convolutional Network
FCN	Fully Convolutional Network
GPR	Gaussian Process Regression
GAN	Generative Adversarial Network
GGE	Genotype and Genotype x Environment
GIS	Geographic Information Systems
GAEC	Ghana Atomic Energy Commission
GPS	Global Positioning Systems
GBM	Gradient Boosting Machine
GNDVI	Green Normalized Difference Vegetation Index
HDR	High Dynamic Range
ITCs	Individual Tree Crowns
ISRIC	International Soil Reference and Information Centre
KNN	K-Nearest Neighbor
LULC	Land Use Land Cover
LAI	Leaf Area Index

LASAP	Light Aided Spectral Absorption Photometry
LSTM	Long Short-Term Memory
ML	Machine Learning
MAV	Manned Aerial Vehicles
Mask RCNN	Mask Region-based Convolutional Neural Network
MLC	Maximum Likelihood Criteria
MAE	Mean Average Error
MAPE	Mean Average Percentage Error
MET	Multi-Environmental Trial
MADAN	Multi-level Attention Domain Adaptation Network
FN	Negative
NeRF	Neural Radiance Field
NDVI	Normalized Difference Vegetation Index
NICFI	Norway International Climate and Forest Initiative
OLS	Ordinary Linear Least Squares
PCA	Principal Component Analysis
PDFs	Probability Density Functions
PCC	Probability of Correct Classification
PRS	Proximal Remote Sensing
RF	Random Forest
RNN	Recurrent Neural Network
RGB	Red, Green, and Blue
R-CNN	Region Convolutional Neural Network
RPN	Region Proposal Network
RS	Remote Sensing
RMSE	Root Mean Square Error
SSD	Single Shot Detector
SOC	Soil Organic Carbon
ISRIC	Soil Reference and Information Centre
SAE	Stacked Autoencoder
SRCNN	Super-Resolution Convolutional Neural Network
SVM	Support Vector Machine
SVR	Support Vector Regression
SAR	Synthetic Aperture Radar
3D	Three-Dimensional
TML	Traditional Machine Learning
TN	True Negative
TP	True Positive
2D	Two-Dimensional

UDS	University for Development Studies
UAV	Unmanned Aerial Vehicle
VGG	Visual Geometry Group
WDM	Water Displacement Method
WACWISA	West African Centre for Water, Irrigation, and Sustainable Agriculture
YOLO	You Only Look Once

CHAPTER ONE

GENERAL INTRODUCTION

1.1 Background

Tree species play a crucial role in maintaining the balance and health of ecosystems. They provide ecological services that are essential for the survival of various life forms. They provide oxygen, enhance air quality, improve soil structure, conserve water, and regulate climate. Additionally, trees offer economic resources, cultural value, and health benefits (Harrison *et al.*, 2022; Seth, 2003; Turner-Skoff and Cavender, 2019). In West Africa's savanna, indigenous multipurpose trees, especially *Adansonia digitata* (baobab) and *Parkia biglobosa* (African locust bean), support rural livelihoods and local food systems.

Adansonia digitata is a tree known for its longevity, which is associated with its ability to thrive in arid environments. *Adansonia digitata* can live for over a millennium and serve as a vital source of food, shelter, and medicine for human and animal species, including insects, birds, and other mammals (Miyoshi *et al.*, 2020; Venter and Witkowski, 2010). Similarly, *Parkia biglobosa* is integral to the ecosystem, and it also contributes to the socio-economic and cultural life of the people in the community where it is found. The seeds and pulp are utilized for food purposes because of their high nutritional value (Houndonougbo *et al.*, 2020).

The utility has created a growing demand that is accompanied by increased extraction pressure, without corresponding improvements in monitoring and management systems. Managing and conserving the tree species is essential for sustaining life on Earth. However, traditional forest inventory methods are time-consuming, labour-intensive, and costly (Canetti *et al.*, 2021; Jurjević *et al.*, 2020). It is therefore important to integrate modern technologies to facilitate studies and enhance our understanding of their characteristics, management, and production (Canetti *et al.*, 2021). This will ensure that they are conserved and sustained for future generations. While they are effective, more efficient methods are desired.

In recent years, the increase in computer speed and memory, coupled with remote sensing and machine learning, has heightened the potential for improved forest inventory efficiency. Tree mapping, productivity, climate change modeling, greenhouse gas inventory, and terrestrial carbon estimations can be achieved at a landscape scale within a short period (Moreira *et al.*, 2021). In the year 2020, 1.8 billion trees were identified and counted in the West African Sahara, Sahel, and sub-humid zone, using deep learning (Brandt *et al.*, 2020). The findings play a critical role in enhancing biomass estimation, climate change modeling, and carbon estimation. They also demonstrate that digital technologies can overcome current limits in tree resource monitoring by offering scalable ways to measure production and support sustainable use.

Furthermore, in Brazil, deep learning and computer vision have been used to locate and count economic trees such as palm. The Multi-level Attention Domain Adaptation Network (MADAN) was used for large-scale and cross-regional oil palm tree counting and detection (Zheng *et al.*, 2020). The method guaranteed high detection accuracy and saved manual tree annotation efforts. Similarly, deep learning was used to identify palm species from UAV-derived RGB images at the individual tree crown level (Ferreira *et al.*, 2020). These studies demonstrate the growing applicability of deep learning for accurate and efficient detection.

Progress has also been made in applying computer vision technology to estimate structural characteristics such as tree height, crown width, and diameter at breast height (DBH) from UAV-based RGB images and LiDAR. Image reconstruction and local maximum filter methods are useful (correlation of 94 % and root mean square of 28 cm) to obtain individual tree heights of coniferous urban forests from UAV images (Birdal *et al.*, 2017). The results are impressive and comparable to those from LiDAR, which hitherto has been at the forefront of this technology. Tree heights and crown diameter estimates from canopy height models (CHMs) that have been derived from 3-dimensional (3D) reconstructions of RGB images also compare well with the ground truth (Panagiotidis *et al.*, 2017). Technology and workflow design are collectively responsible for the quality of results. For example, flying at 25 m above tree canopies at a camera tilt of 60° and forward and side overlaps of 90 % gives optimal results (Moreira *et al.*, 2021). Therefore, computer vision and UAV-based approaches can reliably characterize structural attributes of trees, which are critical inputs for understanding their productivity and yield.

The total size of citrus fruits can be estimated by Faster Region Convolutional Neural Network (R-CNN) and yield by Long Short-term Memory (LSTM) (Apolo-Apolo *et al.*, 2020a). Traditional machine learning approaches, such as support vector regression (SVR) and K-nearest neighbour (KNN), have also produced accurate yield maps at the orchid and individual tree level ($R^2 > 75$) (Chen *et al.*, 2022). Thus, Machine learning algorithms can learn and extract distinctive features unique to individual tree species and their specific environmental contexts. These features are crucial for accurately detecting and estimating structural dimensions and yields. Despite advances for some tree types, native trees, including *Adansonia digitata* and *Parkia biglobosa*, remain underrepresented. This creates a gap in the application of these technologies to support sustainable harvesting, yield estimation, and value chain optimization.

This study applied computer vision and machine learning techniques to detect and characterize *Adansonia digitata* fruits and *Parkia biglobosa* pod yield. It relied on images from diverse sources, including satellite, drone, and smartphone platforms. It focused on instance segmentation to detect *Adansonia digitata* fruits and extracted detailed morphological characteristics to estimate mass, volume, and density. To enhance implementation, it develops a web-based application for the process. Additionally, it explored the relationship between crown area and yield for *Parkia biglobosa* through regression analysis that combines image data with soil characteristics.

1.2 Problem Statement and Justification of Study

Indigenous tree species such as *Adansonia digitata* and *Parkia biglobosa* play a vital role in Africa for their food, fiber, and medicinal properties. They contribute significantly to the income of rural communities through informal markets (Gurashi and Kordofani, 2014; Kristensen and Lykke, 2003; Teklehaimanot, 2004). *Adansonia digitata* extracts, such as seed oil and fruit pulp, have been exported from Africa to Europe, Canada, and the United States of America, and the demand is expected to increase (EC, 2008; Hyde *et al.*, 2017; Welford and Breton, 2008). This rising demand exerts pressure on natural populations, as increased extraction may reduce regeneration where harvesting is unsustainably managed (Gebauer & Luedeling, 2013).

At the collector level, harvesting *Adansonia digitata* and *Parkia biglobosa* is labour-intensive, taking 1 - 4 hours per tree for \$1.70 ± \$0.60 per tree. Raw pulp-covered *Adansonia digitata* sells for \$0.07 per kg while de-pulped, sun-dried *Parkia biglobosa* bean sells for \$0.62 per kg (Adedigba *et al.*, 2024; Jäckering *et al.*, 2019; Masters and Kelly, 2024). High value-addition costs arise from labour-intensive, inefficient harvesting, making products expensive and less accessible. Integrating technology can reduce costs, improve efficiency, and enable scalable production.

Adansonia digitata and *Parkia biglobosa* differ in tree and fruit structure and require distinct yield estimation methods. *Adansonia digitata* produces large, single fruits (Gebauer and Luedeling, 2013; Gurashi and Kordofani, 2014; Houndonougbo *et al.*, 2020), making it suitable for count-based estimates (Gebauer and Luedeling, 2013). In contrast, *Parkia biglobosa's* clustered pods make direct counting difficult. Such variability directly influences production outcomes, quality, and harvesting, which in turn affects consumer demand and pricing (Gurashi and Kordofani, 2014).

Within the study area (Nandom, Navrongo, and Kumbungu), tree and fruit traits are shaped by conditions of the savanna ecological zone, including distinct wet and dry seasons and heterogeneous soils. In addition, community members engage in informal harvesting of species to support livelihoods, which increases the difficulty of accurate yield estimation. In effect, commercialization potential is constrained, and the derived benefits from the native trees are suboptimal. Consequently, Yield models should use image-derived structural features, as climate and soil influence drone and satellite signals (Joswig *et al.*, 2022) to enable assessment of vegetation health, production, and distribution across large areas (Hauser *et al.*, 2021; Houborg *et al.*, 2015; Ma *et al.*, 2019; Thomson *et al.*, 2018).

1.3 Objective of the Study

The main objective of this study was to investigate the application of computer vision and machine learning techniques for the detection and analysis of *Adansonia digitata* and *Parkia biglobosa* production using diverse image sources.

The specific objectives were:

i. To evaluate computer vision models by examining their effectiveness across different countries, climates, and tree species.
ii. To develop a computer vision system to detect Adansonia digitata fruits in images, extract their morphological traits, and estimate physical properties.
iii. To develop a web-based application for estimating the physical properties and distribution density of *Adansonia digitata* fruits from images.
iv. To model the pod yield of *Parkia biglobosa* as a function of crown structural metrics derived from UAV imagery, UAV image-derived vegetation indicators, Satellite image-derived vegetation indicators, soil physicochemical properties, and locality.

1.4 Research Questions

- What algorithms are effective at instance-segmentation of trees and their morphological characteristics?
- How effective are computer vision models for detecting *Adansonia digitata* fruits in smartphone images?
- What image properties of *Adansonia digitata* fruits best estimate their volume, mass, and density?
- Is the yield of *Parkia biglobosa* influenced by crown area, vegetation health, soil properties, and locality?

1.5 Scope

This research utilizes multi-source imagery, computer vision, machine learning, a web-based application, and statistical approaches to detect, characterize, and estimate the yield of native tree species based on key parameters extracted from images. The scope of this work includes an analysis of artificial intelligence (AI) models for tree species segmentation and evaluates their effectiveness across different geographical regions, climatic conditions, and species diversity. The study is structured around three key components:

1. Global Species Identification: This involved analyzing the applications of deep and traditional machine learning for identifying tree species. It also involved evaluating the performance of different models and approaches across various landscapes and ecosystems.
2. Fruit Physical Property Estimation: Development of a computer vision system to estimate the volume, mass, and density of *Adansonia digitata* fruits from single-view RGB images, focusing on morphological characteristics to enhance accuracy.
3. Tree-Level Yield Prediction: A mathematical model that integrates tree morphology, vegetation health indices from drone and satellite imagery, and soil variables to estimate the yield of *Parkia biglobosa* at the tree level.

1.6 Conceptual Framework

The study is conducted in the savanna ecological zone. *Adansonia digitata* fruits are detected and characterized using images captured from a smartphone, deep learning, and machine learning, with Bayesian methods used for classification. A web application is developed for the fruit level analysis. Figure 1.1

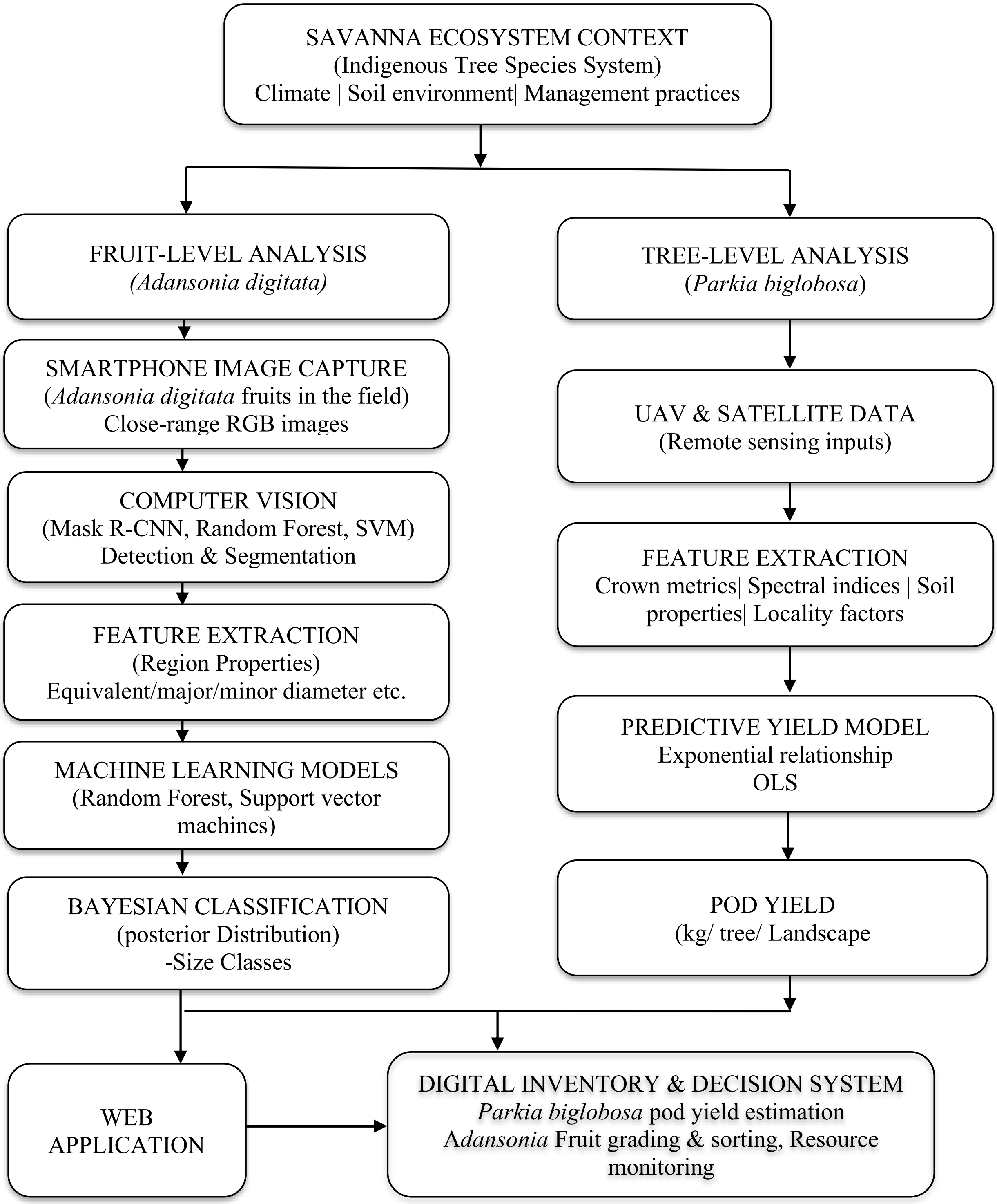

Figure 1.1 Integrated Conceptual Framework: Characterization of *Adansonia digitata* and Estimating Pod Yield of *Parkia biglobosa*

At the tree level, *Parkia biglobosa* pod yield is estimated using crown metrics, spectral indicators from UAV and satellite imagery, soil properties, and locality factors within a predictive modelling framework. Both levels are integrated within a digital system to support inventory, monitoring, and decision-making

1.7 Limitations of the Study

Although the study takes a comprehensive approach, it does have some limitations. The image-based morphological analysis of *Adansonia digitata* fruits was limited by the quality of the images and annotation errors. Again, the study did not consider the impact of management practices on the yield of *Parkia biglobosa*, which may affect production outcomes. Additionally, it did not include data from Synthetic Aperture Radar (SAR) and LiDAR, as these data are more challenging to collect and process on a routine basis compared to standard images. This omission limited the analysis of vegetation structure and morphology. They were acknowledged in the interpretation of the study's findings.

1.8 Outline of the Thesis

The thesis is structured as follows (Figure 1.2): Chapter One serves as the general introduction; it outlines the general context, presents the problem statement, explains the justification for the study, and defines its objectives, scope, and limitations. Chapter Two is dedicated to a systematic literature review, which situates the study within the current theoretical framework. It reviews various machine learning models used for tree detection from drones and satellite imagery. The countries, climate, species, algorithms, and accuracies. Chapter Three focuses on the application of computer vision and machine learning in the morphological characterization of *Adansonia digitata* fruits. Chapter Four introduces a web-based application to estimate the distribution of

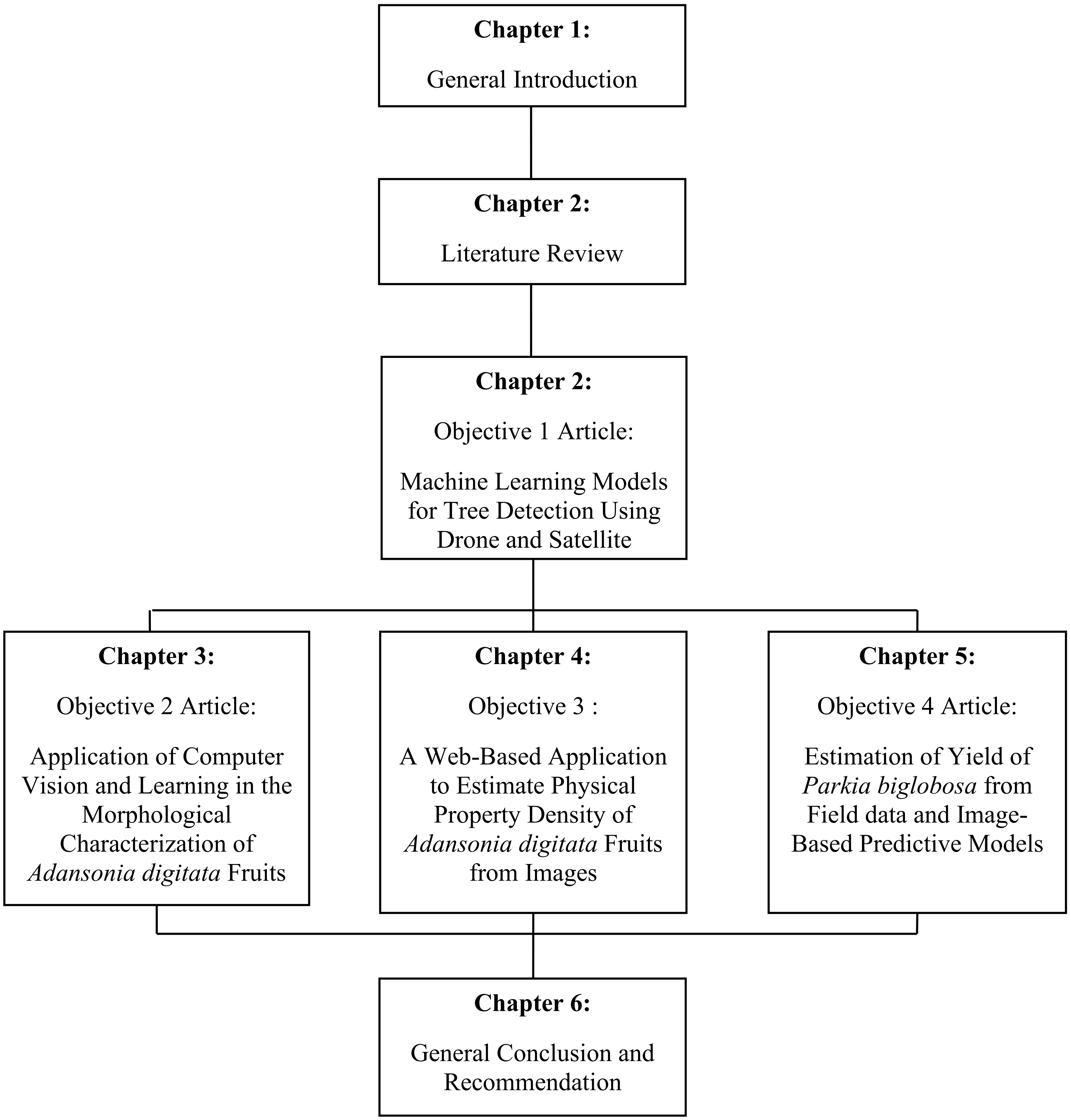

Figure 1.2: Outline of Thesis

physical properties (mass, volume, and density) of *Adansonia digitata* fruits from images. Chapter Five discusses the estimation of yields for *Parkia biglobosa* using field data and image-based predictive models. Chapter Six presents the main conclusions and offers recommendations for implementation and further research.

References

Adedigba, B. K., Bello, K. G., Olukemi, A. D., & Olaitan, A. A. (2024). The locust beans value chain : profit sharing of the key actors in Oyo state, Nigeria. *Journal of Environmental Studies, 36(1),* 1–8. *https://doi.org/10.21608/JESJ.2024.263031.1065*

Amusa, O., Adesoye, A., Ogunkanmi, A., Omoche, O., Olowe, O., Akinyosoye, S., & Omodele, T. (2014). Genetic diversity of *Parkia biglobosa* from different agroecological zones of Nigeria using RAPD markers. *International Journal of Biodiversity*, *2014*, 1–6. https://doi.org/10.1155/2014/457309

Apolo-Apolo, O. E., Martínez-Guanter, J., Egea, G., Raja, P., & Pérez-Ruiz, M. (2020). Deep learning techniques for estimation of the yield and size of citrus fruits using a UAV. *European Journal of Agronomy*, *115*, 126030. https://doi.org/10.1016/j.eja.2020.126030

Birdal, A. C., Avdan, U., & Türk, T. (2017). Estimating tree heights with images from an unmanned aerial vehicle. *Geomatics, Natural Hazards and Risk*, *8*(2), 1144–1156. https://doi.org/10.1080/19475705.2017.1300608

Brandt, M., Tucker, C. J., Kariryaa, A., Rasmussen, K., Abel, C., Small, J., Chave, J., Rasmussen, L. V., Hiernaux, P., Diouf, A. A., Kergoat, L., Mertz, O., Igel, C., Gieseke, F., Schöning, J., Li, S., Melocik, K., Meyer, J., Sinno, S., Fensholt, R. (2020). An unexpectedly large count of trees in the West African Sahara and Sahel. *Nature*, *587*(7832), 78–82. https://doi.org/10.1038/s41586-020-2824-5

Canetti, A., Braz, E. M., de Mattos, P. P., Basso, R. O., & Filho, A. F. (2021). A new approach to maximize the wood production in the sustainable management of Amazon forest. *Annals of Forest Science*, *78*(3). https://doi.org/10.1007/s13595-021-01079-8

Chen, R., Zhang, C., Xu, B., Zhu, Y., Zhao, F., Han, S., Yang, G., & Yang, H. (2022). Predicting individual apple tree yield using UAV multi-source remote sensing data and ensemble learning. *Computers and Electronics in Agriculture*, *201*, 107275. https://doi.org/10.1016/j.compag.2022.107275

EC. (2008). Commission decision: authorizing the placing on the market of baobab dried fruit pulp as a novel food ingredient under regulation (EC) No 258/97 of the European Parliament and of the Council. *Official Journal of the European Union*, *183*, 38–39.

Ferreira, M. P., Almeida, D. R. A. de, Papa, D. de A., Minervino, J. B. S., Veras, H. F. P., Formighieri, A., Santos, C. A. N., Ferreira, M. A. D., Figueiredo, E. O., & Ferreira, E. J. L.

(2020). Individual tree detection and species classification of Amazonian palms using UAV images and deep learning. *Forest Ecology and Management*, *475*, 118397. https://doi.org/10.1016/j.foreco.2020.118397

Gebauer, J., Adam, Y. O., Sanchez, A. C., Darr, D., Eltahir, M. E. S., Fadl, K. E. M., Fernsebner, G., Frei, M., Habte, T. Y., Hammer, K., Hunsche, M., Johnson, H., Kordofani, M., Krawinkel, M., Kugler, F., Luedeling, E., Mahmoud, T. E., Maina, A., Mithöfer, D., … Kehlenbeck, K. (2016). Africa's wooden elephant: the baobab tree (*Adansonia digitata* L.) in Sudan and Kenya: a review. *Genetic Resources and Crop Evolution*, *63*(3), 377–399. https://doi.org/10.1007/s10722-015-0360-1

Gebauer, J., & Luedeling, E. (2013). A note on baobab (*Adansonia digitata* L.) in Kordofan, Sudan. *Genetic Resources and Crop Evolution*, *60*(4), 1587–1596. https://doi.org/10.1007/s10722-013-9964-5

Gurashi, N. A., & Kordofani, M. (2014). Morphological variation in fruit shapes of *Adansonia digitata* L. from Blue Nile and North Kordofan States, Sudan. *Journal of Forest Products & Industries*, *3*(2), 106–111.

Harrison, T. G., Khan, M. A. H., & Shallcross, D. E. (2022). How trees affect the climate : is it just through photosynthesis ? 58, 1–6.

Hauser, L. T., Timmermans, J., van der Windt, N., Sil, Â. F., César de Sá, N., Soudzilovskaia, N. A., & van Bodegom, P. M. (2021). Explaining discrepancies between spectral and in-situ plant diversity in multispectral satellite earth observation. *Remote Sensing of Environment*, *265*. https://doi.org/10.1016/j.rse.2021.112684

Houborg, R., Fisher, J. B., & Skidmore, A. K. (2015). Advances in remote sensing of vegetation function and traits. *International Journal of Applied Earth Observation and Geoinformation*, *43*, 1–6. https://doi.org/10.1016/j.jag.2015.06.001

Houndonougbo, J. S. H., Kassa, B., Mensah, S., Salako, V. K., Glèlè Kakaï, R., & Assogbadjo, A. E. (2020). A global systematic review on conservation nd domestication of *Parkia biglobosa* (Jacq.) R. Br. ex G. Don, an indigenous fruit tree species in Sub-Saharan African traditional parklands: current knowledge and future directions. *Genetic Resources and Crop Evolution*, *67*(4), 1051–1066. https://doi.org/10.1007/s10722-020-00892-w

Hyde, R., Hartley, S., & Millar, K. (2017). European novel foods policy at a critical juncture: Drawing lessons for future novel food governance through a retrospective examination of

Regulation 258/97. *Food and Drug Law Journal*, *72*(3), 472–505.

Jäckering, L., Fischer, S., & Kehlenbeck, K. (2019). A value chain analysis of baobab (Adansonia digitata l.) products in eastern and coastal Kenya. Journal of Agriculture and Rural Development in the Tropics and Subtropics, 120(1), 91–104. https://doi.org/10.17170/kobra-20191030732

Joswig, J. S., Wirth, C., Schuman, M., Kattge, J., Reu, B., Wright, I. J., Sippel, S., Rüger, N., Richter, R., Schaepman, M. E., van Bodegom, P. M., Cornelissen, J. H. C., Díaz, S., Hattingh, W., Kramer, K., Lens, F., Niinemets, Ü., Reich, P. B., Reichstein, M., Römermann, C., Schrodt, F., Anand, M., … (2022). Climatic and soil factors explain the two-dimensional spectrum of global plant trait variation. *Nature Ecology & Evolution*, 6(1), 36–50.

Jurjević, L., Liang, X., Gašparović, M., & Balenović, I. (2020). Is field-measured tree height as reliable as believed – Part II: A comparison study of tree height estimates from conventional field measurement and low-cost close-range remote sensing in a deciduous forest. *ISPRS Journal of Photogrammetry and Remote Sensing*, *169*, 227–241. https://doi.org/10.1016/j.isprsjprs.2020.09.014

Kristensen, M., & Lykke, A. M. (2003). Informant-based valuation of use and conservation preferences of savanna trees in Burkina Faso. *Economic Botany*, *57*(2), 203–217. https://doi.org/10.1663/0013-0001(2003)057[0203:IVOUAC]2.0.CO;2

Ma, X., Zhu, K., Guan, H., Feng, J., Yu, S., & Liu, G. (2019). High-throughput phenotyping analysis of potted soybean plants using colorized depth images based on a proximal platform. *Remote Sensing*, *11*(9). https://doi.org/10.3390/rs11091085

Maroyi, A. (2019). Medicinal uses, biological and chemical properties of Wild Plum (Harpephyllum caffrum): An Indigenous fruit plant of Southern Africa. *Journal of Pharmacy and Nutrition Sciences*, *9*(5), 258–268. https://doi.org/10.29169/1927-5951.2019.09.05.4

Masters, E. T., & Kelly, B. A. (2024). Protein Quality of African Locust Bean - A high-value gathered tree food contributing protein and palatability to plant-based diets. International Journal of Food Science, 2024. https://doi.org/10.1155/2024/1596212

Miyoshi, G. T., Imai, N. N., Tommaselli, A. M. G., de Moraes, M. V. A., & Honkavaara, E. (2020). Evaluation of hyperspectral multitemporal information to improve tree species identification in the highly diverse Atlantic forest. *Remote Sensing*, *12*(2), 1–22. https://doi.org/10.3390/rs12020244

Moreira, B. M., Goyanes, G., Pina, P., Vassilev, O., & Heleno, S. (2021). Assessment of the influence of survey design and processing choices on the accuracy of tree diameter at breast height (Dbh) measurements using UAV-based photogrammetry. *Drones*, *5*(2). https://doi.org/10.3390/drones5020043

Odoom, D. A. (2021). Characterization of Baobab (*Adansonia digitata* L.) in the Builsa District of Ghana. *Journal of Food Technology and Preservation*, *2*(1). https://doi.org/10.36266/JFTP/116

Panagiotidis, D., Abdollahnejad, A., Surový, P., & Chiteculo, V. (2017). Determining tree height and crown diameter from high-resolution UAV imagery. *International Journal of Remote Sensing*, *38*(8–10), 2392–2410. https://doi.org/10.1080/01431161.2016.1264028

Seth, M. K. (2003). Trees and their economic importance. Botanical Review, 69(4), 321–376. https://doi.org/10.1663/0006-8101(2004)069[0321:TATEI]2.0.CO;2

Teklehaimanot, Z. (2004). Exploiting the potential of indigenous agroforestry trees: *Parkia biglobosa* and Vitellaria paradoxa in sub-Saharan Africa. *Agroforestry Systems*, *61–62*(1–3), 207–220. https://doi.org/10.1023/B:AGFO.0000029000.22293.d1

Thomson, E. R., Malhi, Y., Bartholomeus, H., Oliveras, I., Gvozdevaite, A., Peprah, T., Suomalainen, J., Quansah, J., Seidu, J., Adonteng, C., Abraham, A. J., Herold, M., Adu-Bredu, S., & Doughty, C. E. (2018). Mapping the leaf economic spectrum across West African tropical forests using UAV-acquired hyperspectral imagery. *Remote Sensing*, *10*(10). https://doi.org/10.3390/rs10101532

Turner-Skoff, J. B., & Cavender, N. (2019). The benefits of trees for livable and sustainable communities. Plants People Planet, 1(4), 323–335. https://doi.org/10.1002/ppp3.39

Venter, S. M., & Witkowski, E. T. F. (2011). Baobab (*Adansonia digitata* L.) fruit production in communal and conservation land-use types in Southern Africa. *Forest Ecology and Management*, *261*(3), 630–639. https://doi.org/10.1016/j.foreco.2010.11.017

Welford, L., & Breton, G. Le. (2008). Bridging the gap: Phytotrade Africa's experience of the certification of natural products. *Forests Trees and Livelihoods*, *18*(1), 69–79. https://doi.org/10.1080/14728028.2008.9752618

Zerbo, I., Salako, K. V., Hounkpèvi, A., Zozoda, D., Kakaï, R. G., & Thiombiano, A. (2022).

Ethnobotanical knowledge and conservation of *Bombax costatum* Pellegr. and Vuillet: an overexploited savanna tree species. *Trees, Forests and People*, *10*. https://doi.org/10.1016/j.tfp.2022.100356

Zheng, J., Fu, H., Li, W., Wu, W., Zhao, Y., Dong, R., & Yu, L. (2020). Cross-regional oil palm tree counting and detection via a multi-level attention domain adaptation network. *ISPRS Journal of Photogrammetry and Remote Sensing*, *167*, 154–177. https://doi.org/10.1016/j.isprsjprs.2020.07.002

CHAPTER TWO

LITERATURE REVIEW

2.1 Background

This chapter presents a concise literature review on the detection, characterization, and estimation of fruit tree and crop yields using remote sensing images, computer vision, and statistical methods. Trees play a vital role in the socio-economic well-being of communities, contributing to food security and ecosystem resilience. Their sustainable management requires efficient yield estimation that sharply contrasts with traditional methods. The chapter begins with foundational knowledge in remote sensing, contextualizing the definition and examining platforms. It proceeds to give an overview of remote sensing and yield determination, highlighting the image-derived indices often used to determine yield. It then explores computer vision techniques for fruit identification, the key algorithms, and methodologies for estimating fruit volume and mass. The text examines statistical and machine learning models utilized for yield determination. Finally, it addresses the limitations in applying it to determine the yield of native multipurpose species, such as *Adansonia digitata* and *Parkia biglobosa*.

2.2 Remote Sensing

Remote Sensing (RS) has evolved from a broad "observation at a distance" concept into a more operational Earth-observation framework centered on instrument-based acquisition of geospatial information across multiple spectral domains and platforms. In older formulations, remote sensing was defined the science of acquiring information about objects or areas without direct contact (Lambin, 2001; Dyring, 1973). This is a maximal definition that, regardless of platform, encompasses all remote sensing devices, including cameras, lasers, radar systems, sonar, gravimeters, and magnetometers (Jenson, 2009). Sensing occurs at varying distances and could start from 1 cm to a million meters, with no clear ideal distance (Lambin, 2001). Thus, humans can use their eyes, sense of smell, or hearing to accomplish this task (Lillesand *et al*., 2004; Dyring, 1973). More recent usage is narrower and more functional (minimal), emphasizing Earth observation through remote sensing instruments that capture digital imagery and related measurements from different platforms, with distinctions commonly drawn between passive and active sensing systems. The minimal definitions of remote sensing progressively add qualifiers to ensure the definition fits a function or purpose (Jenson, 2009). Since most sensors record information by measuring emitted and reflected radiation of electromagnetic energy from target objects, the source of energy, the wavelength region, the distance, and the platform are often used as qualifiers in minimal definitions (Pierrat *et al*., 2025; Tang and Shao, 2015). When the platform is the source of the measured energy, it is considered active; otherwise, it is considered passive remote sensing (Asner, 2015). Functional definitions have given rise to names such as satellite remote sensing (Shaban, 2022), terrestrial remote sensing (Cracknell and Hayes, 2007), and proximal remote sensing (Tao *et al*., 2022), among others.

Remote sensing for Earth observation requires the acquisition of information from the ultraviolet, visible, infrared, and microwave regions of the electromagnetic spectrum (Kadmon, 2001). Sensors are mounted on platforms such as aircraft or spacecraft, and the information acquired is analysed using visual and digital image processing (Jenson, 2009). Remote sensing is proximal when sensors are placed close to the target. Proximal Remote Sensing (PRS) bridges the gap between relatively coarse airborne or satellite observation by providing high temporal and spatial resolution data (Pierrat *et al*., 2025).

In the context of this study, remote sensing refers to both far and nearby observations made by sensors from satellites, Manned Aerial Vehicles (MAVs), Unmanned Aerial Vehicles (UAVs), also referred to as drones, and smartphones, to discriminate objects and the analysis of required information by visual and digital image processing. This applied definition is preferable because it is consistent with contemporary multi-platform practice and accommodates the study's integrated use of smartphone, drone, and satellite imagery.

2.2.1 Remote Sensing Platforms

Remote sensing operates across various spatial scales, from satellite and aerial platforms generally classified by sensor to target distance, which affects spatial resolution and coverage (Samadzadegan *et al*., 2024).

Satellite remote sensing gives synoptic coverage, repeatability, and long-term data. RS platforms like Landsat, Sentinel, and MODIS offer consistent global observations across multiple spectral bands for environmental monitoring (Cracknell and Hayes, 2007). However, they are limited by due to change in orbits, cloud cover interference (for optical sensors), and often coarse spatial resolution (Samadzadegan *et al*., 2024; Shaban, 2022).

Aerial remote sensing employs aircraft, including manned and unmanned aerial vehicles (MAVs and UAVs), and has become a valuable complement to traditional remote sensing platforms. They provide ultra-high spatial resolution, flexibility in data acquisition times, and the ability to operate under cloud cover when equipped with radar or lidar sensors (Eriksson, 2015), compared to satellite remote sensing. They are effective in smallholder agricultural systems, construction monitoring, and site-specific disaster assessment (Jensen, 2015; Lillesand and Kiefer, 1979).

Proximal Remote Sensing platforms include handheld devices, tripods, vehicles, and towers, and can vary from basic RGB cameras in smartphones to advanced multispectral and hyperspectral imaging systems, including thermographic cameras (Pierrat *et al*., 2025; Tao *et al*., 2022). Unlike satellite or aerial remote sensing, proximal sensors on smartphones provide near-field, high-resolution, and repeatable measurements under various conditions (Pierrat *et al*., 2025). This technology leverages RGB sensors and, in some cases, near-infrared capabilities or depth cameras.

In summary, each platform has its strengths and limitations. Satellite imagery is preferred for large-scale temporal monitoring due to its broad spatial coverage, speed of survey, and spectral resolution (Parman *et al*., 2016). However, it has lower spatial and temporal resolution as well as cost efficiency. In contrast, UAVs are ideal for targeted, high-detail analyses. They are cost-effective and have high spatial and temporal resolutions; however, they face challenges such as limited spatial coverage, slower survey speeds, and reduced spectral resolution (Wang *et al*., 2026). MAVs occupy a moderate position within this spectrum (Figure 2.1).

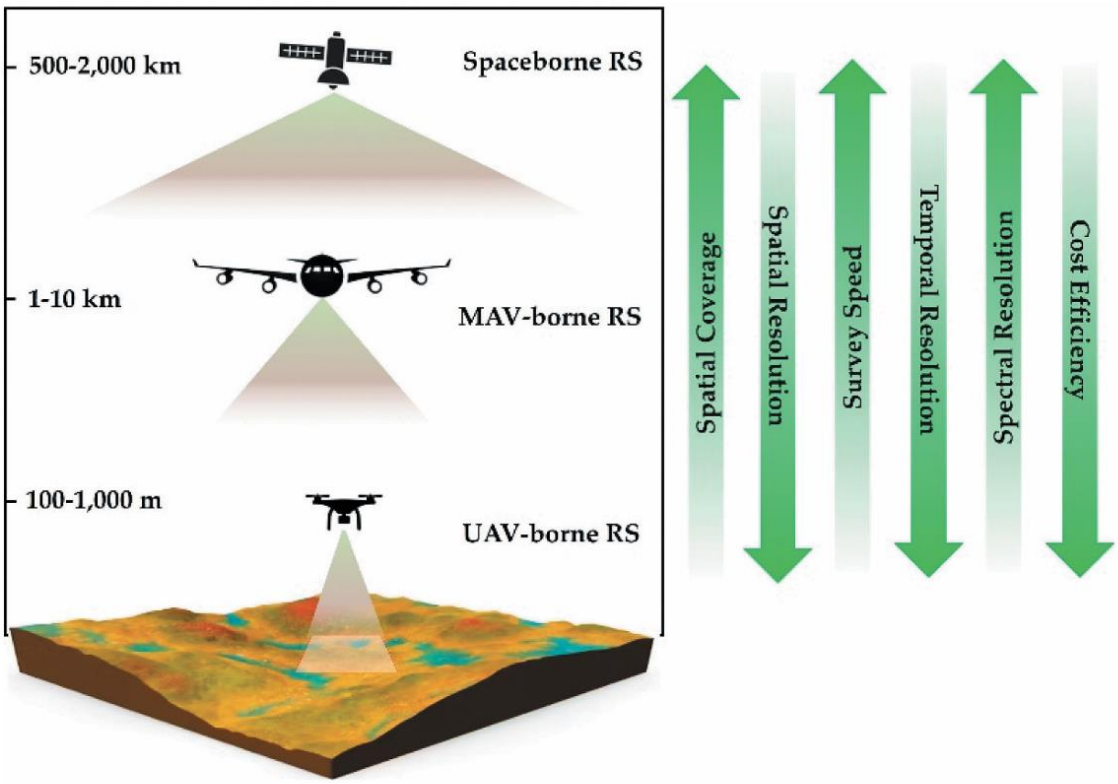

Figure 2.1: A comparison between the spaceborne, MAV-borne, and UAV-borne RS

source: Samadzadegan *et al*. (2024)

Proximal Remote Sensing is preferred for fine-scale, high-frequency data collection. However, in smartphones, the cameras used are usually not calibrated for scientific reflectance (Rançon *et al*., 2023) and are used in uncontrolled environmental settings (Pierrat *et al*., 2025), introducing errors in measurements.

Recent trends highlight the integration of data from different platforms. Satellite and drone data, can be combined, to take advantage of the high spatial resolution of drones and the high temporal resolution of satellites to enhance spatial resolution, serving as an end in itself, or a means to vegetation recognition, crop distribution mapping, or object detection (Alvarez-Vanhard *et al*., 2021; Samadzadegan *et al*., 2024). In addition, proximal sensing by smartphones is becoming a fast and sometimes non-destructive means of gathering environmentally influenced observable and measurable characteristics of organisms (Laamrani *et al*., 2018). Smartphones enable citizen science measurements and are significantly more scalable in space and time than professional instruments (Laamrani *et al*., 2018). They are cost-effective and efficient for data collection and measurement compared to traditional methods that require labor-intensive manual measurements, resulting in higher costs and lower efficiency at high throughput.

2.2.2 Synthetic Aperture Radar (SAR)

Synthetic Aperture Radar (SAR) is an active remote sensing technology that transmits microwave signals and records their backscatter to generate high-resolution images of the Earth's surface (NASA Earthdata, 2025). Unlike optical sensors, it is unaffected by weather or lighting conditions, and it penetrates cloud, fog, and light rain (Doerry, 2019; JOUAV, 2024), making it suitable for continuous agricultural monitoring, especially during critical crop stages in cloud-prone regions. Thus, it operates day and night, rain or shine. In the context of crop yield estimation, Synthetic Aperture Radar (SAR) is valuable for detecting structural changes in vegetation, estimating biomass, and identifying phenological stages such as heading and maturity. Studies have shown that SAR backscatter increases with crop biomass and water content, offering a proxy for growth stages and yield potential (Setiyono *et al*., 2014).

2.3 Yield Determination Overview

Yield studies consistently demonstrate that yield is governed by structural, environmental, and site-specific controls. Allometric theory establishes that tree size and crown architecture determine production capacity (Niklas, 1994; West *et al*., 1999; Pretzsch, 2009). Resource-based frameworks further show that yield is constrained by environmental conditions, particularly soil fertility and resource availability (Monteith, 1977; Lobell *et al.*, 2009). In agroforestry parklands, these factors interact with management and locality effects to produce substantial variability in tree productivity (Boffa, 1999; Akinnifesi *et al.,* 2008; Jamnadass *et al.,* 2011). Consequently, modelling yield as a function of crown structure, soil properties, and locality is well grounded in established yield science, with residual variation representing inherent ecological complexity (Zuur *et al.,* 2009).

Remote Sensing technology provides a scalable and non-destructive approach for yield estimation, which is fundamental to food security, policy formulation, and agricultural decision-making. Traditional yield prediction methods, such as farmer surveys and crop-cutting experiments, have been widely used but are often time-consuming, labor-intensive, and prone to significant inaccuracies (Panda *et al*., 2010). With the increasing demand for timely and scalable information, RS and data-driven approaches, such as machine learning (ML), have gained prominence for improving yield forecasting accuracy and operational efficiency (Jabed and Azmi Murad, 2024). These technologies facilitate landscape-level monitoring and real-time assessment of crop development, making them indispensable tools in modern precision agriculture.

The integration of SAR data into crop models, such as ORYZA2000 for rice, has significantly improved yield prediction accuracy through the addition of SAR-derived information, such as start of growing season and leaf growth rate (Setiyono *et al*., 2014). SAR-based indices and temporal features are also being incorporated into machine learning models to enhance performance in cereals and paddy crops (Lu *et al*., 2019).

2.4 Vegetation Indices

Remote sensing has enabled observations of various surface characteristics, including vegetation health, moisture, and phenology, by measuring energy from surfaces like soil, water, and vegetation (CRISP, 2025; Wikipedia, 2025). A core application in agriculture is the use of Vegetation Indices (VIs), which are mathematical combinations of reflectance values from different spectral bands, most commonly red and Near Infra-Red (NIR). These indices are crucial for yield estimation, as they correlate strongly with photosynthetic activity and plant productivity (Barriguinha *et al*., 2021; Panda *et al*., 2010). Imagery from platforms like Sentinel-2, Landsat, and MODIS provides time-series data used in monitoring vegetation and watersheds (Ablat *et al*., 2021; Soria *et al*., 2022; B. Zhao and Wang, 2024). This information helps to develop strategies for water resource management and sustainable land use in the face of changing environmental conditions (Umukiza *et al*., 2024). Additionally, they aid land cover change analysis, informing policies aimed at conserving protected forests (Amponsah *et al*., 2022) and estimating agricultural yields (Al-Gaadi *et al*., 2016).

Vegetation Indices derived from optical sensors remain central in yield estimations. Indices such as the Normalized Difference Vegetation Index (NDVI), Enhanced Vegetation Index (EVI), and Green NDVI (GNDVI) serve as proxies for biophysical traits, including chlorophyll concentration and Leaf Area Index (LAI), which are directly linked to crop productivity (Barriguinha *et al*., 2021). However, these indices perform better for full-canopy crops (e.g., wheat and maize) than for discontinuous crops (e.g., vineyards), where soil background interference reduces index sensitivity (Victorino *et al*., 2022). Nonetheless, indices such as NDVI and LAI have shown moderate success even in vineyards when combined with advanced regression techniques (Barriguinha *et al*., 2021)

In proximal remote sensing, using Light Aided Spectral Absorption Photometry (LASAP), images from the smartphone have been used with indices to measure the chlorophyll content of corn leaves with an R^2 of 0.97 (Vesali *et al*., 2017).

2.5 Computer Vision and Image Processing

Computer vision (CV) enables computers to interpret and understand visual inputs such as images and videos. It aims to replicate the capabilities of the human visual system in machines (Szeliski, 2011). Foundational tasks in computer vision are based on image processing and include image acquisition, enhancement, segmentation, object detection, and three-dimensional reconstruction (Forsyth and Ponce, 2012). Image processing focuses on enhancing and extracting information from images. It uses noise reduction, segmentation, histogram equalization, and edge sharpening to enhance contrast and highlight features that aid interpretation (Ritika and Kaur, 2013).

Image acquisition refers to the process of capturing real-world images using digital sensors and devices. It often precedes image processing. The devices used for capturing images include Charge-Coupled Device (CCD) and Complementary Metal-Oxide Semiconductor (CMOS) cameras, scanners, satellite sensors, and specialized equipment like infrared and LiDAR systems (Li *et al*., 2014). Recent advancements integrate multiple sensors such as RGB, depth, and inertial sensors, with event-based cameras that replicate biological vision for high-speed and low-latency capture (Gallego *et al*., 2022). Smartphones use computational imaging techniques, such as High

Dynamic Range (HDR)+, which merges burst images for noise reduction and enhanced detail (Hasinoff *et al*., 2016).

Traditional image enhancement improves quality for better perception or analysis, which has been automated in deep learning. The era of deep learning started with the Super-Resolution Convolutional Neural Network (SRCNN) (Dong *et al*., 2014), followed by Generative Adversarial Networks (GAN) based methods like Super-Resolution Generative Adversarial Network (SRGAN), for enhancing image resolution (Ledig *et al*., 2017). Recent advancements include Enhanced Super-Resolution Generative Adversarial Network (ESRGAN) (X. Wang *et al*., 2018) and diffusion models, which improve image details and make them appear realistic.

Image segmentation divides an image into meaningful regions by labeling each pixel based on visual or semantic characteristics. It aims to outline objects or uniform areas in the image. Segmentation can utilize low-level cues like color and texture (Yu *et al*., 2023). Common methods include thresholding, region-based approaches, and edge detection techniques. Segmentation generates a mask that identifies pixels belonging to specific regions or objects (Yu *et al*., 2023). The two main types are semantic segmentation and instance segmentation, with panoptic segmentation combining both (Kirillov *et al*., 2019).

Semantic segmentation assigns a class to each pixel in an image (Csurka *et al*., 2022). The Fully Convolutional Network (FCN) marked the start of deep learning-based semantic segmentation (Shelhamer *et al*., 2017). Improvements in segmentation models include architectures like DeepLab (Chen *et al*., 2017) and U-Net (Ronneberger *et al*., 2021). The Segment Anything Model (SAM) by Kirillov *et al*. (2023) represents a breakthrough with its zero-shot segmentation using prompt-based learning.

Instance segmentation refers to the process of recognizing and delineating distinct objects of the same class within an image. A prominent model used for this purpose is Mask R-CNN ((He *et al*., 2017), which builds upon the Faster R-CNN framework by incorporating an additional branch for only mask prediction. Recent advancements in frameworks (panoptic segmentations) aim to combine semantic and instance segmentation tasks within a single model (Cheng *et al*., 2022).

Thus, unlike instance segmentation, semantic segmentation does not differentiate between objects of the same class. Semantic segmentation is used in land cover mapping and medical imaging (Jain *et al*., 2023; G. Wang *et al*., 2024), while instance segmentation is for object counting and fruit detection (Fusaro *et al*., 2024; Wojszczyk *et al*., 2024). It provides a better understanding of the objects in the image, especially when there is occlusion (Figure 2.2).

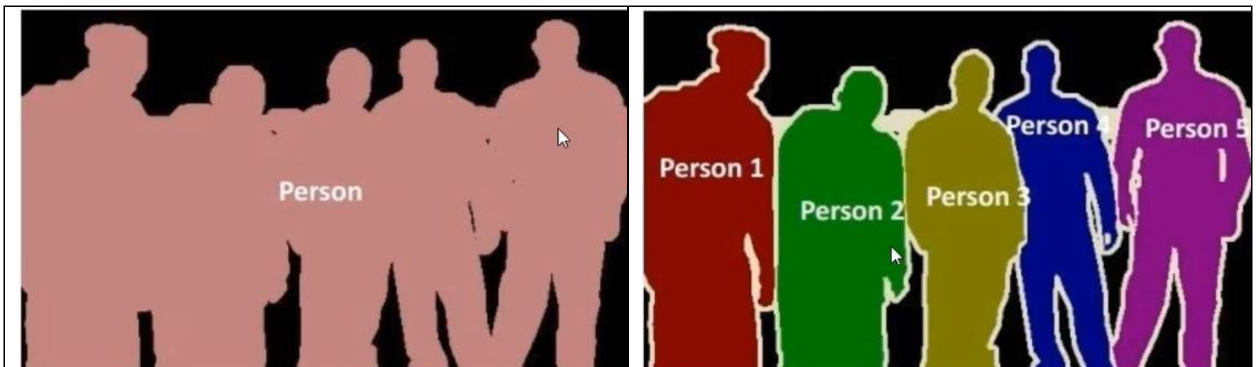

Semantic Segmentation	Instance Segmentation

Figure 2.2: Segmentation

Source: Saple *et al*. (2022)

Object detection involves the identification and localization of objects within an image using bounding boxes defining a coarse object boundary compared to semantic and instance segmentation (Figure 2.3).

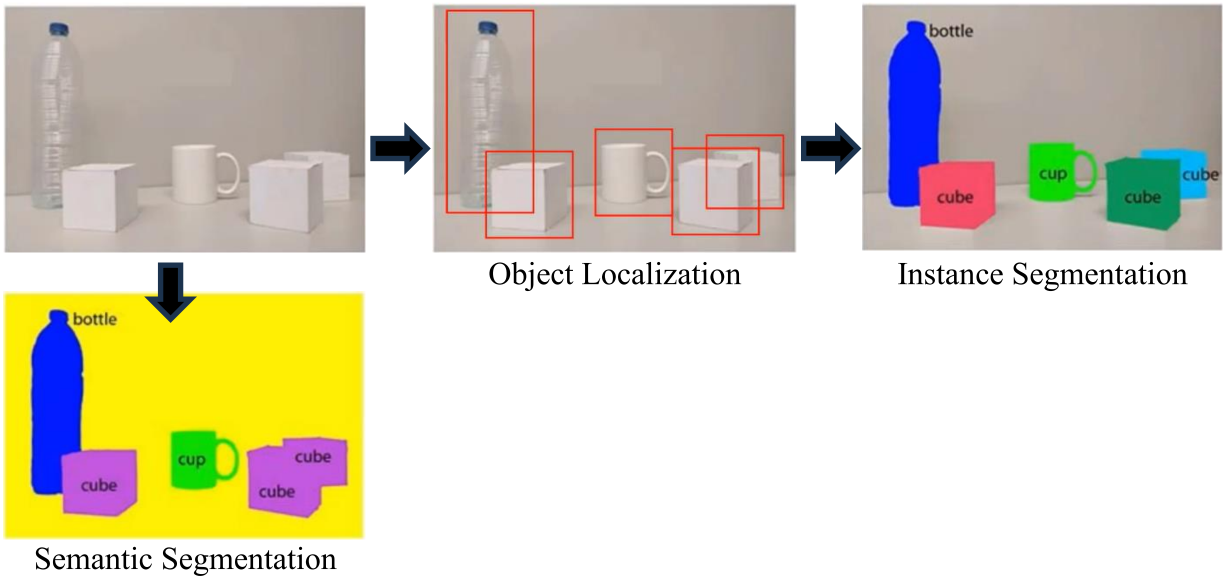

Figure 2.3: Segmentation Process

Source: DigitalSreeni, (2022)

Early models, such as R-CNN (Girshick *et al*., 2014), evolved into Faster R-CNN (Ren *et al*., 2017), which integrates region proposal networks for improved performance in object detection. To strike a balance between speed and accuracy, one-stage detectors like You Only Look Once (YOLO) (Redmon *et al*., 2016) and RetinaNet (Lin *et al*., 2020) were introduced. More recently, Detection Transformer (DETR), a transformer-based model, represented a novel approach by predicting sets of objects directly, thereby eliminating the need for traditional anchor boxes and non-maximum suppression (Carion *et al*., 2020).

A three-dimensional (3D) reconstruction creates spatial representations based on 2D images or sensor data. Traditional methods include Structure-from-Motion (Snavely *et al*., 2006) and Multi-View Stereo (Furukawa and Ponce, 2010). Neural Radiance Fields (NeRF) (Mildenhall *et al*., 2020) represent scenes facilitating high-quality novel view synthesis. Recent research has concentrated on enhancing NeRF for real-time applications and improving its generalizability to dynamic and large-scale environments. Modern advancements in computer vision have been influenced by traditional machine learning and deep learning techniques. Convolutional Neural Networks (CNNs) have become the standard for tasks such as image classification, semantic segmentation, and instance segmentation due to their ability to learn hierarchical feature representations directly from data (Szeliski, 2011). The success of these models relies on principles derived from classical image processing techniques. Consequently, computer vision and image processing are interconnected. Image processing focuses on operations that prepare images for analysis, while computer vision provides the framework for interpreting these images in context, making them inherently linked.

2.6 Computer Vision for Natural Objects and Vegetation

Computer vision provides the framework for the automated detection and classification of natural objects, vegetation, and fruits. Before the advent of deep learning, techniques such as color thresholding, spectral indices, and shape analysis were employed in conjunction with statistical analysis to distinguish vegetation from soil or urban areas (Baatuuwie and Leeuwen, 2011; Luo *et al*., 2003). In deep learning, innovations like R-CNN, Fast R-CNN, Faster R-CNN, Mask R-CNN, YOLO, and U-Net have improved vegetation segmentation accuracy and fruit detection and counting (Ayhan *et al*., 2020; Xiao *et al*., 2023).

Vegetation classification has evolved from index-based methods to deep learning models, which provide more accurate results in complex environments. The former were quicker but oversimplified scenes and introduced errors (Miao *et al*., 2024). In recent times, vegetation cover identification and classification have been accomplished using U-Net for tree crowns and Mask R-CNN for individual tree segmentation (Ayhan *et al*., 2020). State-of-the-art deep CNNs, including transformer-augmented models, yield the most accurate vegetation maps in complex environmental contexts.

Forest vegetation can be detected using YOLOv5 from vehicle-mounted RGB images, achieving rapid inference with high precision (Mendes *et al*., 2023). Similar results were observed by employing YOLOv7 to identify standing dead trees in aerial images, with 94 % precision and 98% mAP (Zhou *et al*., 2024). Faster R-CNN detects fallen logs or human-made objects in forests, with higher accuracy but slower speed.

2.6.1 Fruit Detection and Yield Estimation

Detecting fruits is a crucial task in determining fruit tree yield. Due to occlusion, shadows, and variable lighting, image processing methods that rely on color and shape are not very effective (Xu and Lv, 2018). This has led to a preference for deep learning approaches, making YOLO, Single Shot Detector (SSD), and R-CNN models popular. Approximately 17% of studies use YOLO models because they provide real-time speed. Successful YOLO implementations have been reported for various crops, including mangoes and clustered lychees (Koirala *et al*., 2019; Qi *et al*., 2022). The Region-based Convolutional Neural Networks (Faster R-CNN) and Mask R-CNN models deliver high accuracy, with some studies achieving over 90 % in fruit detection (Xiao *et al*., 2023). However, detecting small or occluded fruits continues to be a challenge, often necessitating advanced segmentation techniques.

2.6.2 *Adansonia digitata* and *Parkia biglobosa* Detection

Research on *Adansonia digitata* fruits and *Parkia biglobosa* is limited. Very limited literature exist on the application of CNN-based object detectors or deep segmentation networks for *Adansonia* *digitata* fruits or *Parkia biglobosa* beans, although some work exists on mapping *Adansonia digitata* trees and *Parkia biglobosa* beans; using sub-meter-resolution satellite imagery, Brandt *et al*. (2020) detected over 1.8 billion individual trees with crown size greater than 3 m^2 and median of 12 m^2 in the West African Sahara, Sahel, and sub-humid zone, and Huang *et al*. (2024) identified nearly 2.8 million *Adansonia digitata* trees in the Sahel. This gap in deep-learning research concerning *Adansonia digitata* fruits presents opportunities for advancements in automated yield estimates and ecological monitoring of this species.

2.6.3 Key Algorithms and Architectures

Deep learning has greatly enhanced computer vision, especially in tree fruit detection. Convolutional Neural Networks (CNNs) are vital for modern image recognition, as they learn feature representations directly from images. These networks have improved upon traditional methods that often struggled with varying environmental conditions (Bargoti and Underwood, 2017).

YOLO is a real-time object detection architecture that predicts bounding boxes and class probabilities from the entire image for high frame rates. However, its performance can decline in densely packed or occluded scenarios.

Region-based Convolutional Neural Network (R-CNN) represents a significant advancement in the field of object detection. The original R-CNN (Girshick *et al*., 2014) introduced the concept of proposing object regions and applying Convolutional Neural Networks (CNNs) to each region. This approach evolved with the introduction of Fast R-CNN (Girshick, 2015), followed by the development of Faster R-CNN (Ren *et al*., 2017). The Faster R-CNN model incorporates a Region

Proposal Network (RPN) and demonstrates significantly improved accuracy and efficiency in complex environments. It has been successfully utilized for detecting mangoes, almonds, and apples in orchards, achieving F1-scores greater than 0.9 (Bargoti and Underwood, 2017). Mask R-CNN is an extension of Faster R-CNN, which facilitates instance segmentation by introducing an additional branch for predicting segmentation masks with bounding boxes. This feature is advantageous for distinguishing small objects, such as fruits, or those that are clustered or partially occluded. The pixel-level precision provided by Mask R-CNN enhances both accuracy and interpretability in proximal remote sensing tasks, including morphological characterization, yield prediction, and phenotyping.

ACE R-CNN builds upon Mask R-CNN (He *et al*., 2017) by introducing an Attention-guided Contextual Encoder (ACE) that enhances region features with multi-scale, global, and local context through the use of spatial and channel attention (Li *et al*., 2022). It also integrates Sobel filters to capture edge-aware features, which improve object boundary localization in segmentation tasks. These advancements lead to higher detection accuracy, especially for small or occluded objects. However, ACE R-CNN adds computational overhead and still relies on anchor-based proposals (Tian *et al*., 2019).

DEtection Transformer (DETR) is a transformer-based object detector that replaces traditional components like anchor boxes and non-maximum suppression (NMS) with a set-based prediction framework (Carion *et al*., 2020). It uses a transformer encoder-decoder to model global relationships and directly predicts object bounding boxes and labels using Hungarian matching (Carion *et al*., 2020). DETR handles occlusions and overlapping well but suffers from slow training, struggles with small objects, and has high computational demands (Zhu *et al*., 2021).

2.6.4 Image Processing for Morphological Feature Extraction

Image processing for morphological feature extraction involves analyzing two-dimensional (2D) images to extract basic morphological features such as area, perimeter, and shape descriptors. By measuring the radius and area from single-view images of axisymmetric fruits such as citrus, it is possible to estimate their size and shape, and the estimates closely align with manual measurements for grading (Iqbal *et al*., 2015). In contrast to citrus fruits, *Adansonia digitata* fruits are mostly non-axisymmetric; they exhibit varied shapes such as ellipsoid, reniform, and globose. These shapes are classified based on both quantitative and qualitative descriptors, such as length, diameter, and weight (Murage *et al*., 2022).

Deep learning models offer significant advantages in handling complex datasets with noisy backgrounds and overlaps. Networks like Mask R-CNN and YOLO have been applied successfully for fruit detection, segmentation, and size estimation in mangoes, apples, and tomatoes (Ferrer-Ferrer *et al*., 2023; Neupane *et al*., 2022). The image-derived metrics can be correlated to biological parameters such as pulp mass and seed number using traditional machine learning.

2.7 Volume Estimation Techniques

Volume estimation often begins with shape-fitting techniques that approximate fruits with geometric solids (e.g., spheres, ellipsoids). Single-view images and analytical volume formulas have been used for spherical and ellipsoidal apples (Iqbal *et al*., 2011). This approach is especially suitable for axisymmetric fruits.

In contrast, for irregular shapes, silhouette-based multi-view reconstruction systems have been used to estimate surface area and volume by creating 3D wireframe models (Lee *et al*., 2006).

Similarly, a Monte-Carlo framework was used to estimate volume based on binary silhouettes (Siswantoro *et al*., 2013), demonstrating flexible applicability to various fruit shapes. Additionally, Chopin *et al*. (2017) introduced a high-throughput volume estimation method. The method was based on three orthogonal 2D projections, and it achieved an error of approximately 2 % for rounded fruits.

Recent developments in Red, Green, and Blue-Depth (RGB-D) imaging have facilitated the integration of depth and color information. Reconstructed 3D point clouds from images taken from multi-perspectives can be achieved by applying slicing algorithms for volume estimation (Zhu *et al*. 2024). The accuracy was impressive, exceeding 95 %. The method was improved by using deep learning on 2 x 2 pixel units (Kim *et al*. 2025).

Photogrammetry employs structure-from-motion and multi-view stereo techniques to reconstruct real-world objects from images. Together with M-Estimator SAmple Consensus (MSAC) and template matching, 3D apples constructed from orchard images can be isolated with accuracies greater than 88 % (Gené-Mola *et al*. 2021). However, this method depends on accurate matching of features, and factors like poor lighting or blurred images can lower the accuracy. In addition, photogrammetric processing is computationally intensive, making it less suitable for real-time applications or large-scale use without significant computer resources.

2.8 Mass and Volume Prediction Models

The mass and volume of fruits and agricultural produce are essential physical properties that impact yield estimation, postharvest logistics, and market value. They help value chain actors forecast production, plan storage and transportation, and influence consumer preference (Kumar and Singh, 2022).

Mass can be estimated from volume, assuming a constant fruit density. Support vector machine models that use radial basis functions have been used to estimate cherry tomato mass with over 98 % R^2 and about 15 g RMSE (Nyalala *et al*., 2019). When instance segmentation was combined with ensemble regression, the Mean Average Percentage Error (MAPE) was 9.1 % (Lee *et al*., 2020). The accuracy of the estimate for mass depends on the error level in the volume or estimated shape descriptors, used as geometric proxies for volume (Omid *et al*., 2010). Thus, reducing volume uncertainty is essential for accurate mass estimation. Axisymmetric shapes allow the derivation of analytical error expressions by using error propagation formulas (Huynh *et al*., 2020).

2.9 Statistical and Machine Learning Modeling for Yield Estimation

Statistical modelling provides a framework for understanding and predicting yield based on biophysical, environmental, and management variables (Alvarado *et al*., 2020). Linear regression and ANOVA models are commonly used for analyzing Multi-Environmental Trials (METs), where yield responses are affected by genotype, environment, and their interactions (Argaw *et al*., 2025; Ricardo *et al*., 2019). There are two widely used models in this context: the Additive Main Effect and Multiplicative Interactive (AMMI) model and the Genotype and Genotype x Environment (GGE) biplot model (Abebe *et al*., 2024). The AMMI model separates the additive and interaction components of variance, providing a robust framework for interpreting yield data, especially in identifying stable and high-performing genotypes across environments (Gauch *et al*., 2008). The GGE model, by contrast, focuses on genotype performance and GE interactions visualized and delineated through biplots (Gauch et al., 2008).

A major challenge in statistical modeling is the presence of multicollinearity among predictor variables (Banks and Fienberg, 2003; Voss, 2005). Collinearity inflates standard errors and can obscure the true effect of individual predictors. It can be mitigated by dimensionality reduction techniques such as Principal Component Analysis (PCA), regularization methods like Ridge Regression, and strategic feature selection based on ecological relevance and statistical diagnostics (Dormann *et al*., 2013).

Recent advances have led to a transition to machine learning-based models, which are better equipped to capture complex, nonlinear interactions. Algorithms such as support vector machines, random forest, and Gaussian Process Regression (GPR) have demonstrated strong performance in yield prediction tasks (Liu *et al*., 2024). Gaussian Process Regressions (GPRs) outperform traditional models in predicting wheat yield and dry matter in the North China Plain (Liu *et al*., 2024).

Machine Learning (ML) models offer flexible frameworks to model nonlinear relationships between multi-source data and yield (Jabed and Azmi Murad, 2024). These methods can incorporate diverse features, such as spectral indices, climate variables, and topographic data, allowing for comprehensive and context-aware yield prediction (Araghi and Daccache, 2025). For example, combining Sentinel-2 indices with TerraClimate data has improved wheat yield forecasts in Iran (Araghi and Daccache, 2025). Pixel-level ML models reduce the time for data cleaning, feature extraction, and spectral index time series analysis, and can discriminate between cloudy data to enable high-resolution yield mapping, which supports precision agriculture (Perich *et al*., 2023). Deep learning models, such as convolutional neural networks (CNNs) and Recurrent Neural

Networks (RNNs), have shown promise in extracting spatiotemporal features from satellite time series for yield prediction (Lu *et al*., 2019).

However, machine learning models often trade interpretability for higher predictive performance. Complex models like deep neural networks and ensemble methods can improve accuracy but make decision logic opaque (Kakogeorgiou and Karantzalos, 2021; Zhao *et al*., 2024). Again, model generalization across regions and seasons remains a challenge, prompting interest in hybrid approaches and explainable AI techniques to ensure interpretability and trust (Kakogeorgiou and Karantzalos, 2021).

In contrast, simpler models such as linear regression and small decision trees provide clear relationships between inputs and outputs. Although they lack top-tier predictive power, they retain explanatory power (Linardatos *et al*., 2021). Therefore, there is a trade-off between model complexity, accuracy, and explainability: highly accurate models tend to be less interpretable, while simpler, more transparent models sacrifice some predictive accuracy.

2.10 Soil Data Integration

Combining spectral imagery and soil variables enhances yield prediction accuracy (Sarkar *et al*., 2025). Soil data enhances model resilience, especially in heterogeneous landscapes where remote sensing alone may not capture all yield-determining variables (Fowler *et al*., 2024). Remote sensing detects signals from plants on the surface. However, the soil also plays a crucial role in plant growth because it provides water and nutrients. When soil and RS data are used together in machine learning or crop models, the prediction improves in accuracy (Sahbeni *et al*., 2023; Sarkar *et al*., 2025).

Trentin *et al*. (2024) also emphasized the need for multi-source data integration, including soil and weather variables, for improving yield prediction accuracy using machine learning models. They identified this as crucial for developing robust, generalizable models applicable across diverse agro-ecological zones.

Similarly, combining vegetation indices with environmental covariates like soil moisture has been shown to enhance yield estimation models. For instance, Prasad *et al*. (2006) and Fathollahi *et al*. (2024) demonstrated improved yield prediction using NDVI, soil moisture, surface temperature, and rainfall as inputs.

2.11 Conclusion

Computer vision and remote sensing technology applications are increasing in agricultural yield estimation, utilizing tools like object detection, instance segmentation, and spectral vegetation indices. The tools have demonstrated good performance in conventional crops, but the same cannot be said for indigenous tree species, such as *Adansonia digitata* and *Parkia biglobosa*. These trees have unique structures, irregular spacing, and wide morphological variation of species, which may pose challenges to standard object detection and yield modeling approaches. For instance, *Adansonia digitata* trees exhibit highly variable fruit shapes and sizes, which makes it difficult to develop generalized morphological models. The absence of specialized data collection tools and methods for fruit characterization and specific background contextualization raises a barrier for direct application based on success observed in other species and environments.

Yield estimation models rely heavily on spectral indices such as NDVI or EVI, which may not effectively capture the productivity of tree crops with partial or sparse canopies. Both *Adansonia* *digitata* and *Parkia biglobosa* species are typically found in heterogeneous, smallholder landscapes, where soil variability, mixed cropping, and environmental stressors further complicate yield modeling. Yet, drone-based high-resolution imagery, which could help overcome these limitations, is still underutilized. There is also a lack of integration between remote sensing outputs and measurements of soil properties and environmental conditions for yield analysis. To address these constraints, we need to develop species-specific image analysis protocols and create detailed annotated datasets. Additionally, yield models must integrate multi-source data, including canopy metrics, phenology, and edaphic factors. This approach will enhance the accuracy and relevance of predictions for these vital yet overlooked tree crops, ultimately improving fruit crop production practices and resource management.

References

Abebe, A. T., Adewumi, A. S., Adebayo, M. A., Shaahu, A., Mushoriwa, H., Alabi, T., Derera, J., Agbona, A., & Chigeza, G. (2024). Genotype x environment interaction and yield stability of soybean (Glycine max l.) genotypes in multi-environment trials (METs) in Nigeria. *Heliyon*, *10*(19), e38097. https://doi.org/10.1016/j.heliyon.2024.e38097

Ablat, X., Liu, G., Liu, Q., & Huang, C. (2021). Using modis-ndvi time series to quantify the vegetation responses to river hydro-geomorphology in the wandering river floodplain in an arid region. *Water (Switzerland)*, *13*(16). https://doi.org/10.3390/w13162269

Akinnifesi, F. K., Leakey, R. R. B., Ajayi, O. C., Sileshi, G., Tchoundjeu, Z., Matakala, P., & Kwesiga, F. R. (2008). *Indigenous fruit trees in the tropics: Domestication, utilization and commercialization*. CABI.

Al-Gaadi, K. A., Hassaballa, A. A., Tola, E., Kayad, A. G., Madugundu, R., Alblewi, B., & Assiri, F. (2016). Prediction of potato crop yield using precision agriculture techniques. *PLoS ONE*, *11*(9), 1–16. https://doi.org/10.1371/journal.pone.0162219

Alvarado, G., Rodríguez, F. M., Pacheco, A., Burgueño, J., Crossa, J., Vargas, M., Pérez-Rodríguez, P., & Lopez-Cruz, M. A. (2020). META-R: A software to analyze data from multi-environment plant breeding trials. *Crop Journal*, *8*(5), 745–756. https://doi.org/10.1016/j.cj.2020.03.010

Alvarez-Vanhard, E., Corpetti, T., & Houet, T. (2021). UAV & satellite synergies for optical remote sensing applications: A literature review. *Science of Remote Sensing*, *3*(February), 100019. https://doi.org/10.1016/j.srs.2021.100019

Amponsah, A., Nasare, L. I., Tom-Dery, D., & Baatuuwie, B. N. (2022). Land cover changes of Atewa Range Forest Reserve, a biodiversity hotspot in Ghana. *Trees, Forests and People*, *9*(January), 100301. https://doi.org/10.1016/j.tfp.2022.100301

Araghi, A., & Daccache, A. (2025). Remote sensing and TerraClimate datasets for wheat yield prediction using machine learning. *Smart Agricultural Technology*, *11*(August 2024), 100909. https://doi.org/10.1016/j.atech.2025.100909

Argaw, T., Fenta, B. A., Zegeye, H., Azmach, G., & Funga, A. (2025). Multi-environment trials data analysis: linear mixed model-based approaches using spatial and factor analytic models. *Frontiers in Research Metrics and Analytics*, *10*. https://doi.org/10.3389/frma.2025.1472282

Asner, G. P. (2015). Environmental remote sensing and imaging spectroscopy. In S. A. Levin (Ed.), *Encyclopedia of biodiversity* (2nd ed., pp. 129–137). Academic Press. https://doi.org/10.1016/B978-0-12-800066-3.00004-8

Ayhan, B., Kwan, C., Budavari, B., Kwan, L., Lu, Y., Perez, D., Li, J., Skarlatos, D., & Vlachos, M. (2020). Vegetation Detection Using Deep Learning and Conventional Methods. *Remote Sensing*, *12*(15). https://doi.org/10.3390/rs12152502

Baatuuwie, N. B., & Leeuwen, I. L. Van. (2011). Evaluation of three classifiers in mapping forest stand types using medium resolution imagery : a case study in the Offinso Forest District , Ghana. *African Journal of Environmental Science and Technology*, *5*(January), 25–36.

Banks, D. L., & Fienberg, S. E. (2003). *Statistics , Multivariate*. 851–889.

Bargoti, S., & Underwood, J. (2017). Deep fruit detection in orchards. *Proceedings - IEEE International Conference on Robotics and Automation*, 3626–3633. https://doi.org/10.1109/ICRA.2017.7989417

Barriguinha, A., Neto, M. de C., & Gil, A. (2021). Vineyard yield estimation, prediction, and forecasting: A systematic literature review. In *Agronomy* (Vol. 11, Issue 9). https://doi.org/10.3390/agronomy11091789

Brandt, M., Tucker, C. J., Kariryaa, A., Rasmussen, K., Abel, C., Small, J., Chave, J., Rasmussen, L. V., Hiernaux, P., Diouf, A. A., Kergoat, L., Mertz, O., Igel, C., Gieseke, F., Schöning, J., Li, S., Melocik, K., Meyer, J., Sinno, S., … Fensholt, R. (2020). An unexpectedly large count of trees in the West African Sahara and Sahel. *Nature*, *587*(7832), 78–82. https://doi.org/10.1038/s41586-020-2824-5

Carion, N., Massa, F., Synnaeve, G., Usunier, N., Kirillov, A., & Zagoruyko, S. (2020). End-to-End Object Detection with Transformers. *Lecture Notes in Computer Science (Including Subseries Lecture Notes in Artificial Intelligence and Lecture Notes in Bioinformatics)*, *12346 LNCS*, 213–229. https://doi.org/10.1007/978-3-030-58452-8_13

Chen, L.-C., Papandreou, G., Schroff, F., & Adam, H. (2017). *Rethinking Atrous Convolution for Semantic Image Segmentation*. http://arxiv.org/abs/1706.05587

Cheng, B., Misra, I., Schwing, A. G., Kirillov, A., & Girdhar, R. (2022). Masked-attention Mask Transformer for Universal Image Segmentation. *Proceedings of the IEEE Computer Society Conference on Computer Vision and Pattern Recognition*, *2022-June*, 1280–1289. https://doi.org/10.1109/CVPR52688.2022.00135

Cracknell, A. P., & Hayes, L. (2007). Introduction to remote sensing, second edition. In *Introduction to Remote Sensing, Second Edition*. https://doi.org/10.1201/b13575

CRISP. (2025). *Optical Remote Sensing*. Centre for Remote Imaging, Sensing and Processing.

Csurka, G., Volpi, R., & Chidlovskii, B. (2022). Semantic Image Segmentation: Two Decades of Research. *Foundations and Trends in Computer Graphics and Vision*, *14*(1–2), 1–162. https://doi.org/10.1561/0600000095

DigitalSreeni. (2022). *283 - What is Mask R-CNN? - YouTube*. https://www.youtube.com/watch?v=NEl9RPyMgzY&list=PL6st9qYyc3jLZ4ijMXeaWQtkPzr99GoMa&index=2

Doerry, A. (2019). Introduction to synthetic aperture radar. In *2019 IEEE Radar Conference, RadarConf 2019*. https://doi.org/10.1109/RADAR.2019.8835560

Dong, C., Loy, C. C., He, K., & Tang, X. (2014). Learning a Deep Convolutional Network for Image Super-Resolution. In D. Fleet, T. Pajdla, B. Schiele, & T. Tuytelaars (Eds.), *Computer Vision -- ECCV 2014* (pp. 184–199). Springer International Publishing.

Dormann, C. F., Elith, J., Bacher, S., Buchmann, C., Carl, G., Carré, G., Marquéz, J. R. G., Gruber, B., Lafourcade, B., Leitão, P. J., Münkemüller, T., Mcclean, C., Osborne, P. E., Reineking, B., Schröder, B., Skidmore, A. K., Zurell, D., & Lautenbach, S. (2013). Collinearity: A review of methods to deal with it and a simulation study evaluating their performance. *Ecography*, *36*(1), 27–46. https://doi.org/10.1111/j.1600-0587.2012.07348.x

Dyring, E. (1973). Principles of Remote Sensing. *Ambio*, *11*(3), 57–69. https://doi.org/10.4324/9780203714522-9

Eriksson, U. (2015). *Reading the Sky and The Spiral of Teaching and Learning in Astronomy*. *January*, 1–7.

Fathollahi, L., Wu, F., Melaki, R., Jamshidi, P., & Sarwar, S. (2024). Global Normalized Difference Vegetation Index forecasting from air temperature, soil moisture and precipitation using a deep neural network. *Applied Computing and Geosciences*, *23*(October 2023), 100174. https://doi.org/10.1016/j.acags.2024.100174

Ferrer-Ferrer, M., Ruiz-Hidalgo, J., Gregorio, E., Vilaplana, V., Morros, J. R., & Gené-Mola, J. (2023). Simultaneous fruit detection and size estimation using multitask deep neural networks. *Biosystems Engineering*, *233*(September), 63–75. https://doi.org/10.1016/j.biosystemseng.2023.07.010

Forsyth, D. A., & Ponce, J. (2012). *Computer Vision: A Modern Approach*. Pearson.

Fowler, A., Basso, B., Maureira, F., Millar, N., Ulbrich, R., & Brinton, W. F. (2024). Spatial patterns of historical crop yields reveal soil health attributes in US Midwest fields. *Scientific Reports*, *14*(1), 1–15. https://doi.org/10.1038/s41598-024-51155-y

Furukawa, Y., & Ponce, J. (2010). Accurate, dense, and robust multiview stereopsis. *IEEE Transactions on Pattern Analysis and Machine Intelligence*, *32*(8), 1362–1376. https://doi.org/10.1109/TPAMI.2009.161

Fusaro, D., Magistri, F., Behley, J., Pretto, A., & Stachniss, C. (2024). *Horticultural Temporal*

Fruit Monitoring via 3D Instance Segmentation and Re-Identification using Point Clouds. http://arxiv.org/abs/2411.07799

Gallego, G., Delbruck, T., Orchard, G., Bartolozzi, C., Taba, B., Censi, A., Leutenegger, S., Davison, A. J., Conradt, J., Daniilidis, K., & Scaramuzza, D. (2022). Event-Based Vision: A Survey. *IEEE Transactions on Pattern Analysis and Machine Intelligence*, *44*(1), 154–180. https://doi.org/10.1109/TPAMI.2020.3008413

Gauch, H. G., Piepho, H. P., & Annicchiarico, P. (2008). Statistical analysis of yield trials by AMMI and GGE: Further considerations. *Crop Science*, *48*(3), 866–889. https://doi.org/10.2135/cropsci2007.09.0513

Girshick, R. (2015). Fast R-CNN. *Proceedings of the IEEE International Conference on Computer Vision*, *2015 Inter*, 1440–1448. https://doi.org/10.1109/ICCV.2015.169

Girshick, R., Donahue, J., Darrell, T., & Malik, J. (2014). Rich feature hierarchies for accurate object detection and semantic segmentation. *Proceedings of the IEEE Computer Society Conference on Computer Vision and Pattern Recognition*, 580–587. https://doi.org/10.1109/CVPR.2014.81

Hasinoff, S. W., Barron, J. T., Sharlet, D., Geiss, R., Kainz, F., Chen, J., Adams, A., & Levoy, M. (2016). Burst photography for high dynamic range and low-light imaging on mobile cameras. *ACM Transactions on Graphics*, *35*(6). https://doi.org/10.1145/2980179.2980254

He, K., Gkioxari, G., Dollár, P., & Girshick, R. (2017). Mask R-CNN. *ICCV*.

Huang, K., Brandt, M., Hiernaux, P., Tucker, C. J., Rasmussen, L. V., Reiner, F., Li, S., Kariryaa, A., Mugabowindekwe, M., den Braber, B., Small, J., Sino, S., & Fensholt, R. (2024). Mapping every adult baobab (*Adansonia digitata* L.) across the Sahel and relationships to rural livelihoods. *Nature Ecology & Evolution*, *8*(9), 1632–1640. https://doi.org/10.1038/s41559-024-02483-9

Huynh, T., Tran, L., & Dao, S. (2020). Real-time size and mass estimation of slender axi-symmetric fruit/vegetable using a single top view image. *Sensors (Switzerland)*, *20*(18), 1–24. https://doi.org/10.3390/s20185406

Iqbal, S. M., Gopal, A., Sankaranarayanan, P. E., & Nair, A. B. (2015). Estimation of size and shape of citrus fruits using image processing for automatic grading. *2015 3rd International Conference on Signal Processing, Communication and Networking, ICSCN 2015*. https://doi.org/10.1109/ICSCN.2015.7219859

Iqbal, S. M., Gopal, A., & Sarma, A. S. V. (2011). Volume estimation of apple fruits using image processing. *ICIIP 2011 - Proceedings: 2011 International Conference on Image Information Processing*, *Iciip*. https://doi.org/10.1109/ICIIP.2011.6108909

Jabed, M. A., & Azmi Murad, M. A. (2024). Crop yield prediction in agriculture: A comprehensive review of machine learning and deep learning approaches, with insights for future research and sustainability. *Heliyon*, *10*(24), e40836. https://doi.org/10.1016/j.heliyon.2024.e40836

Jain, S. N., Pise, P., & Mishra, A. (2023). Semantic segmentation in medical image analysis with convolutional neural networks. *9102*(November), 3143–3148. https://doi.org/10.21917/ijivp.2023.0447

Jamnadass, R., Dawson, I. K., Franzel, S., Leakey, R. R. B., Mithöfer, D., Akinnifesi, F. K., & Tchoundjeu, Z. (2011). Improving livelihoods and nutrition in Sub-Saharan Africa through the promotion of indigenous and exotic fruit production in smallholders' agroforestry systems: A review. *International Forestry Review, 13*(3), 338-354. https://doi.org/10.1505/146554811798293836

Jensen, J. R. (2015). Introduction to Digital Image Processing: A Remote Sensing Perspective. In *Sustainability (Switzerland)* (Vol. 11, Issue 1). http://scioteca.caf.com/bitstream/handle/123456789/1091/RED2017-Eng-8ene.pdf?sequence=12&isAllowed=y%0Ahttp://dx.doi.org/10.1016/j.regsciurbeco.2008.06.005%0Ahttps://www.researchgate.net/publication/305320484

Jenson, J. R. (2009). *Remote Sensing of the Environment, An Earth Resource Perspective*.

Jouav. (2024). *What is SAR Imagery? Guide to Synthetic Aperture Radar*.

Kakogeorgiou, I., & Karantzalos, K. (2021). Evaluating explainable artificial intelligence methods for multi-label deep learning classification tasks in remote sensing. *International Journal of Applied Earth Observation and Geoinformation*, *103*. https://doi.org/10.1016/j.jag.2021.102520

Kirillov, A., He, K., Girshick, R., Rother, C., & Dollar, P. (2019). Panoptic segmentation. *Proceedings of the IEEE Computer Society Conference on Computer Vision and Pattern Recognition*, *2019-June*, 9396–9405. https://doi.org/10.1109/CVPR.2019.00963

Kirillov, A., Mintun, E., Ravi, N., Mao, H., Rolland, C., Gustafson, L., Xiao, T., Whitehead, S., Berg, A. C., Lo, W.-Y., Dollár, P., & Girshick, R. (2023). *Segment Anything*. http://arxiv.org/abs/2304.02643

Koirala, A., Walsh, K. B., Wang, Z., & McCarthy, C. (2019). Deep learning for real-time fruit detection and orchard fruit load estimation: benchmarking of 'MangoYOLO.' *Precision Agriculture*, *20*(6), 1107–1135. https://doi.org/10.1007/s11119-019-09642-0

Kumar, M., & Singh, D. (2022). Estimating Volume and Mass of Tomato Fruits by Image Processing Technique. *Indian Journal of Ecology*, *49*(3806), 2179–2183.

https://doi.org/10.55362/ije/2022/3806

Laamrani, A., Lara, R. P., Berg, A. A., Branson, D., & Joosse, P. (2018). Using a mobile device "app" and proximal remote sensing technologies to assess soil cover fractions on agricultural fields. *Sensors (Switzerland)*, *18*(3), 1–16. https://doi.org/10.3390/s18030708

Lambin, E. F. (2001). Remote sensing and geographic information systems analysis. In N. J. Smelser & P. B. Baltes (Eds.), *International encyclopedia of the social & behavioral sciences* (pp. 13150–13155). Pergamon. https://doi.org/10.1016/B0-08-043076-7/04200-5

Ledig, C., Theis, L., Huszár, F., Caballero, J., Cunningham, A., Acosta, A., Aitken, A., Tejani, A., Totz, J., Wang, Z., & Shi, W. (2017). Photo-realistic single image super-resolution using a generative adversarial network. *Proceedings - 30th IEEE Conference on Computer Vision and Pattern Recognition, CVPR 2017*, *2017-Janua*, 105–114. https://doi.org/10.1109/CVPR.2017.19

Lee, D. J., Eifert, J. D., Zhan, P., & Xu, X. (2006). Area and volume measurements of objects with irregular shapes using multiple silhouettes. *Optical Engineering*, *45*(2), 027202. https://doi.org/10.1117/1.2166847

Lee, J., Nazki, H., Baek, J., Hong, Y., & Lee, M. (2020). Artificial intelligence approach for tomato detection and mass estimation in precision agriculture. *Sustainability (Switzerland)*, *12*(21), 1–15. https://doi.org/10.3390/su12219138

Li, L., Zhang, Q., & Huang, D. (2014). A review of imaging techniques for plant phenotyping. *Sensors (Switzerland)*, *14*(11), 20078–20111. https://doi.org/10.3390/s141120078

Li, Y., Chai, G., Wang, Y., Lei, L., & Zhang, X. (2022). ACE R-CNN: An Attention Complementary and Edge Detection-Based Instance Segmentation Algorithm for Individual Tree Species Identification Using UAV RGB Images and LiDAR Data. *Remote Sensing*, *14*(13). https://doi.org/10.3390/rs14133035

Lillesand, T., Kiefer, R. W., & Chipman, J. (2004). Remote sensing. In *Encyclopedia of GIS*. Springer. https://doi.org/10.1007/1-4020-4520-4_343

Lillesand, T. M., & Kiefer, R. W. (1979). Remote sensing and image interpretation. In *Remote sensing and image interpretation.* Wiley. https://doi.org/10.2307/634969

Lin, T. Y., Goyal, P., Girshick, R., He, K., & Dollar, P. (2020). Focal Loss for Dense Object Detection. *IEEE Transactions on Pattern Analysis and Machine Intelligence*, *42*(2), 318–327. https://doi.org/10.1109/TPAMI.2018.2858826

Linardatos, P., Papastefanopoulos, V., & Kotsiantis, S. (2021). Explainable ai: A review of machine learning interpretability methods. *Entropy*, *23*(1), 1–45. https://doi.org/10.3390/e23010018

Liu, F., Su, L., Luo, P., Tao, W., Wang, Q., & Deng, M. (2024). Prediction Models of Growth Characteristics and Yield for Chinese Winter Wheat Based on Machine Learning. *Agronomy*, *14*(4). https://doi.org/10.3390/agronomy14040839

Lobell, D. B., Cassman, K. G., & Field, C. B. (2009). Crop yield gaps: Their importance, magnitudes, and causes. *Annual Review of Environment and Resources, 34*, 179–204. https://doi.org/10.1146/annurev.environ.041008.093740

Lu, B., He, Y., & Dao, P. D. (2019). Comparing the performance of multispectral and hyperspectral images for estimating vegetation properties. *IEEE Journal of Selected Topics in Applied Earth Observations and Remote Sensing*, *12*(6), 1784–1797. https://doi.org/10.1109/JSTARS.2019.2910558

Luo, J., Singhal, A., & Zhu, W. (2003). Natural object detection in outdoor scenes based on probabilistic spatial context models. *Proceedings - IEEE International Conference on Multimedia and Expo*, *2*(June), 457–460. https://doi.org/10.1109/ICME.2003.1221652

Mendes, P. A. S., Coimbra, A. P., & de Almeida, A. T. (2023). Forest Vegetation Detection Using Deep Learning Object Detection Models. *Forests*, *14*(9), 1–22. https://doi.org/10.3390/f14091787

Miao, S., Wang, C., Kong, G., Yuan, X., Shen, X., & Liu, C. (2024). Utilizing active learning and attention-CNN to classify vegetation based on UAV multispectral data. *Scientific Reports*, *14*(1), 1–18. https://doi.org/10.1038/s41598-024-82248-3

Mildenhall, B., Srinivasan, P. P., Tancik, M., Barron, J. T., Ramamoorthi, R., & Ng, R. (2020). NeRF: Representing Scenes as Neural Radiance Fields for View Synthesis. *Lecture Notes in Computer Science (Including Subseries Lecture Notes in Artificial Intelligence and Lecture Notes in Bioinformatics)*, *12346 LNCS*, 405–421. https://doi.org/10.1007/978-3-030-58452-8_24

Monteith, J. L. (1977). Climate and the efficiency of crop production in Britain. *Philosophical Transactions of the Royal Society B: Biological Sciences, 281*(980), 277–294. *https://doi.org/10.1098/rstb.1977.0140*

Murage, M., Onguso, J. M., Remmy, W., & Wekesa, T. B. (2022). Morphological Characterization of Baobab Fruit (*Adansonia Digitata* L.) in Makueni, Taita Taveta, Kilifi and Kwale Counties in Kenya. ‖ *World Journal of Agricultural Research*, *10*(3), 82–93. https://doi.org/10.12691/wjar-10-3-4

NASA Earthdata. (2025). *Synthetic Aperture Radar (SAR)*.

Neupane, C., Koirala, A., & Walsh, K. B. (2022). In-Orchard Sizing of Mango Fruit: 1. Comparison of Machine Vision Based Methods for On-The-Go Estimation. *Horticulturae*, *8*(12). https://doi.org/10.3390/horticulturae8121223

Niklas, K. J. (1994). *Plant allometry: The scaling of form and process*. University of Chicago Press.

Nyalala, I., Okinda, C., Nyalala, L., Makange, N., Chao, Q., Chao, L., Yousaf, K., & Chen, K. (2019). Tomato volume and mass estimation using computer vision and machine learning algorithms: Cherry tomato model. *Journal of Food Engineering*, *263*(July), 288–298. https://doi.org/10.1016/j.jfoodeng.2019.07.012

Omid, M., Khojastehnazhand, M., & Tabatabaeefar, A. (2010). Estimating volume and mass of citrus fruits by image processing technique. *Journal of Food Engineering*, *100*(2), 315–321. https://doi.org/10.1016/j.jfoodeng.2010.04.015

Panda, S. S., Ames, D. P., & Panigrahi, S. (2010). Application of vegetation indices for agricultural crop yield prediction using neural network techniques. *Remote Sensing*, *2*(3), 673–696. https://doi.org/10.3390/rs2030673

Parman, R., Kamarudin, N., Ismail, A., & Ibrahim, S. (2016). A review of uses of satellite imagery in monitoring mangrove forests. *IOP Conference Series: Earth and Environmental Science, 37*(1), 012034. https://doi.org/10.1088/1755-1315/37/1/012034

Perich, G., Turkoglu, M. O., Graf, L. V., Wegner, J. D., Aasen, H., Walter, A., & Liebisch, F. (2023). Pixel-based yield mapping and prediction from Sentinel-2 using spectral indices and neural networks. *Field Crops Research*, *292*(March), 108824. https://doi.org/10.1016/j.fcr.2023.108824

Pierrat, Z. A., Magney, T. S., Richardson, W. P., Runkle, B. R. K., Diehl, J. L., Yang, X., Woodgate, W., Smith, W. K., Johnston, M. R., Ginting, Y. R. S., Koren, G., Albert, L. P., Kibler, C. L., Morgan, B. E., Barnes, M., Uscanga, A., Devine, C., Javadian, M., Meza, K., … Cawse-Nicholson, K. (2025). Proximal remote sensing: an essential tool for bridging the gap between high-resolution ecosystem monitoring and global ecology. *New Phytologist*, 419–436. https://doi.org/10.1111/nph.20405

Prasad, A. K., Chai, L., Singh, R. P., & Kafatos, M. (2006). Crop yield estimation model for Iowa using remote sensing and surface parameters. *International Journal of Applied Earth Observation and Geoinformation*, *8*(1), 26–33. https://doi.org/10.1016/j.jag.2005.06.002

Pretzsch, H. (2009). *Forest dynamics, growth and yield: From measurement to model*. Springer. https://doi.org/10.1007/978-3-540-88307-4

Qi, X., Dong, J., Lan, Y., & Zhu, H. (2022). Article Method for Identifying Litchi Picking Position Based on YOLOv5 and PSPNet. *Remote Sensing*, *14*(9), 1–17. https://doi.org/10.3390/rs14092004

Rançon, F., Keresztes, B., Deshayes, A., Tardif, M., Abdelghafour, F., Fontaine, G., Da Costa, J. P., & Germain, C. (2023). Designing a Proximal Sensing Camera Acquisition System for Vineyard Applications: Results and Feedback on 8 Years of Experiments. *Sensors*, *23*(2). https://doi.org/10.3390/s23020847

Redmon, J., Divvala, S., Girshick, R., & Farhadi, A. (2016). You only look once: Unified, real-time object detection. *Proceedings of the IEEE Computer Society Conference on Computer Vision and Pattern Recognition*, *2016-Decem*, 779–788. https://doi.org/10.1109/CVPR.2016.91

Ren, S., He, K., Girshick, R., & Sun, J. (2017). Faster R-CNN: Towards Real-Time Object Detection with Region Proposal Networks. *IEEE Transactions on Pattern Analysis and Machine Intelligence*, *39*(6), 1137–1149. https://doi.org/10.1109/TPAMI.2016.2577031

Ricardo, P., Viana, A. P., Gomes, V. M., Preisigke, C., & De, O. F. (2019). Genetics and Plant Breeding | Research Article approaches and mixed models. *Scientia Agricola*, *1*(October), 424–433.

Ritika, R., & Kaur, S. (2013). Contrast Enhancement Techniques for Images - A Visual Analysis. *International Journal of Computer Applications*, *64*(17), 20–25. https://doi.org/10.5120/10727-5679

Ronneberger, O., Philipp, F., & Thomas, B. (2021). UNet: Convolutional Networks for Biomedical Image Segmentation. *IEEE Access*, *9*, 16591–16603. https://doi.org/10.1109/ACCESS.2021.3053408

Sahbeni, G., Székely, B., Musyimi, P. K., Timár, G., & Sahajpal, R. (2023). Crop Yield Estimation Using Sentinel-3 SLSTR, Soil Data, and Topographic Features Combined with Machine Learning Modeling: A Case Study of Nepal. *AgriEngineering*, *5*(4), 1766–1788. https://doi.org/10.3390/agriengineering5040109

Samadzadegan, F., Toosi, A., & Dadrass Javan, F. (2024). A critical review on multi-sensor and multi-platform remote sensing data fusion approaches: current status and prospects. *International Journal of Remote Sensing*, *46*(3), 1327–1402. https://doi.org/10.1080/01431161.2024.2429784

Saple, M. R., Jadhav, T. M., Kode, S. Y., & Gargi. (2022). Density Based Traffic Control System with Convolutional Neural Network. *ITM Web of Conferences*, *44*, 03045. https://doi.org/10.1051/itmconf/20224403045

Sarkar, S., Osorio Leyton, J. M., Noa-Yarasca, E., Adhikari, K., Hajda, C. B., & Smith, D. R. (2025). Integrating Remote Sensing and Soil Features for Enhanced Machine Learning-Based Corn Yield Prediction in the Southern US. *Sensors*, *25*(2), 1–27. https://doi.org/10.3390/s25020543

Setiyono, T., Nelson, A., & Holecz, F. (2014). Remote Sensing based Crop Yield Monitoring and Forecasting. *Expert Meeting on Crop Monitoring for Improved Food Security*, *February*.

Shaban, A. (2022). Fundamentals of Satellite Remote Sensing. In *Springer Water*. https://doi.org/10.1007/978-3-031-15549-9_1

Shelhamer, E., Long, J., & Darrell, T. (2017). Fully Convolutional Networks for Semantic Segmentation. *IEEE Transactions on Pattern Analysis and Machine Intelligence*, *39*(4), 640–651. https://doi.org/10.1109/TPAMI.2016.2572683

Siswantoro, J., Prabuwono, A. S., & Abdulah, A. (2013). Volume Measurement of Food Product with Irregular Shape Using Computer Vision and Monte Carlo Method: A Framework. *Procedia Technology*, *11*(June), 764–770. https://doi.org/10.1016/j.protcy.2013.12.256

Snavely, N., Seitz, S. M., & Szeliski, R. (2006). Photo tourism: Exploring photo collections in 3D. *ACM SIGGRAPH 2006 Papers, SIGGRAPH '06*, 835–846. https://doi.org/10.1145/1179352.1141964

Soria, J., Ruiz, M., & Morales, S. (2022). Monitoring Subaquatic Vegetation Using Sentinel-2 Imagery in Gallocanta Lake (Aragón, Spain). *Earth (Switzerland)*, *3*(1), 363–382. https://doi.org/10.3390/earth301002

Szeliski, R. (2011). Computer vision: algorithms and applications. *Choice Reviews Online*, *48*(09), 48-5140-48–5140. https://doi.org/10.5860/choice.48-5140

Tang, L., & Shao, G. (2015). Drone remote sensing for forestry research and practices. *Journal of Forestry Research*, *26*(4), 791–797. https://doi.org/10.1007/s11676-015-0088-y

Tao, H., Xu, S., Tian, Y., Li, Z., Ge, Y., Zhang, J., Wang, Y., Zhou, G., Deng, X., Zhang, Z., Ding, Y., Jiang, D., Guo, Q., & Jin, S. (2022). Proximal and remote sensing in plant phenomics: 20 years of progress, challenges, and perspectives. *Plant Communications*, *3*(6), 100344. https://doi.org/10.1016/j.xplc.2022.100344

Tian, Z., Shen, C., Chen, H., & He, T. (2019). FCOS: Fully convolutional one-stage object detection. *Proceedings of the IEEE International Conference on Computer Vision*, *2019-Octob*, 9626–9635. https://doi.org/10.1109/ICCV.2019.00972

Trentin, C., Ampatzidis, Y., Lacerda, C., & Shiratsuchi, L. (2024). Tree crop yield estimation and prediction using remote sensing and machine learning: A systematic review. *Smart Agricultural Technology*, *9*(September), 100556. https://doi.org/10.1016/j.atech.2024.100556

Umukiza, E., Abagale, F. K., & Adongo, T. A. (2024). Characterization of landuse and landcover dynamics and their impact on runoff generation patterns in dam catchments of

Northern Ghana. *Geocarto International*, *39*(1). https://doi.org/10.1080/10106049.2024.2335247

Vesali, F., Omid, M., Mobli, H., & Kaleita, A. (2017). Feasibility of using smart phones to estimate chlorophyll content in corn plants. *Photosynthetica*, *55*(4), 603–610. https://doi.org/10.1007/s11099-016-0677-9

Victorino, G., Braga, R. P., Santos-Victor, J., & Lopes, C. M. (2022). Comparing a New Non-Invasive Vineyard Yield Estimation Approach Based on Image Analysis with Manual Sample-Based Methods. In *Agronomy* (Vol. 12, Issue 6). https://doi.org/10.3390/agronomy12061464

Voss, D. S. (2005). *Multicollinearity*. *2*, 2005.

Wang, G., Chen, J., Mo, L., Wu, P., & Yi, X. (2024). Lightweight land cover classification via semantic segmentation of remote sensing imagery and analysis of influencing factors. *Frontiers in Environmental Science*, *12*(February), 1–20. https://doi.org/10.3389/fenvs.2024.1329517

Wang, X., Yu, K., Wu, S., Gu, J., & Liu, Y. (2018). *ESRGAN : Enhanced Super-Resolution Generative Adversarial Networks*. *1*, 63–79. https://doi.org/10.1007/978-3-030-11021-5

West, G. B., Brown, J. H., & Enquist, B. J. (1999). A general model for the structure and allometry of plant vascular systems. *Nature, 400*(6745), 664–667. https://doi.org/10.1038/23251

Wikipedia. (2025). *Visible and Near-Infrared (VNIR)* (Issue April 2011, p. 2012). http://ru.wikipedia.org/?oldid=27468909

Wojszczyk, R., Radzimowski, W., & Królikowski, T. (2024). Counting objects using image segmentation methods. *Procedia Computer Science*, *246*(C), 2302–2311. https://doi.org/10.1016/j.procs.2024.09.558

Xiao, F., Wang, H., Xu, Y., & Zhang, R. (2023). Fruit Detection and Recognition Based on Deep Learning for Automatic Harvesting: An Overview and Review. *Agronomy*, *13*(6). https://doi.org/10.3390/agronomy13061625

Xu, L., & Lv, J. (2018). Recognition method for apple fruit based on SUSAN and PCNN. *Multimedia Tools and Applications*, *77*(6), 7205–7219. https://doi.org/10.1007/s11042-017-4629-6

Yu, Y., Wang, C., Fu, Q., Kou, R., Huang, F., Yang, B., Yang, T., & Gao, M. (2023). Techniques and Challenges of Image Segmentation: A Review. *Electronics (Switzerland)*, *12*(5). https://doi.org/10.3390/electronics12051199

Zhao, B., & Wang, L. (2024). Surface water monitoring from 1984 to 2021 based on Landsat time-series images and Google Earth Engine. *Heliyon*, *10*(17). https://doi.org/10.1016/j.heliyon.2024.e36660

Zhao, T., Wang, S., Ouyang, C., Chen, M., Liu, C., Zhang, J., Yu, L., Wang, F., Xie, Y., Li, J., Wang, F., Grunwald, S., Wong, B. M., Zhang, F., Qian, Z., Xu, Y., Yu, C., Han, W., Sun, T., … Wang, L. (2024). Artificial intelligence for geoscience: Progress, challenges, and perspectives. *The Innovation*, *5*(5), 100691. https://doi.org/10.1016/j.xinn.2024.100691

Zhou, H., Wu, S., Xu, Z., & Sun, H. (2024). Automatic detection of standing dead trees based on improved YOLOv7 from airborne remote sensing imagery. *Frontiers in Plant Science*, *15*(January), 1–18. https://doi.org/10.3389/fpls.2024.1278161

Zhu, X., Su, W., Lu, L., Li, B., Wang, X., & Dai, J. (2021). Deformable Detr: Deformable Transformers for End-To-End Object Detection. *ICLR 2021 - 9th International Conference on Learning Representations*, 1–16.

Zuur, A. F., Ieno, E. N., Walker, N. J., Saveliev, A. A., & Smith, G. M. (2009). *Mixed effects models and extensions in ecology with R*. Springer. *https://doi.org/10.1007/978-0-387-87458-6*

CHAPTER THREE

MACHINE LEARNING MODELS FOR TREE DETECTION USING DRONE AND SATELLITE IMAGES: SYSTEMATIC REVIEW

3.1 Introduction

Instance segmentation of tree species from aerial and satellite images has gained significant attention because of its potential for various applications, such as urban planning, environmental monitoring, and forest management (Dong *et al.*, 2019; Zhang *et al.*, 2020). Brandt *et al.* (2020) identified and enumerated at least 1.8 billion individual trees in the West African Sahara, Sahel, and subhumid zones using satellite images and deep learning. The contribution of these trees to ecosystem services, including carbon storage, food, and shelter, is invaluable and essential.

Deep and traditional machine learning have gained prominence in tree identification and counting across diverse geographical locations. The interest in their application is reflected in the growing number of reviews and analyses undertaken to evaluate deep and traditional machine learning models for tree classification and detection using aerial and satellite images. Sheykhmousa *et al.* (2020) focused on the performance of random forest (RF) and support vector machine (SVM) models, they varied parameters such as data types, remote sensing applications, spatial resolutions, and the number of extracted features. Their study analyzed 251 articles and revealed that SVM classifiers were the most used and effective in tree detection tasks; nonetheless, RF performed better in landuse/ landcover (LULC) classification. Furthermore, the accuracy was not strongly correlated with the number of features for either the RF or SVM model.

Heydari and Mountrakis (2019) compared the performances of various ML models. These included deep learning (DL) models such as convolutional neural networks (CNNs), deep belief networks (DBNs), and stacked autoencoders (SAEs), as well as traditional machine learning (TML) models represented by support vector machines (SVMs). They studied 103 manuscripts, and 92 cases supported direct accuracy comparisons between DL and SVM models. The findings indicated that SVM models generally outperformed other traditional machine learning models. Additionally, DL models reportedly outperform traditional machine learning models in terms of accuracy. The study also highlighted that the CNN-based models demonstrated the highest overall performance among all the models analyzed.

Heydari and Mountrakis (2019) and Sheykhmousa *et al.* (2020) agree that artificial intelligence models are useful for tree detection from aerial and satellite images. However, the performance of these models can be influenced by various factors, such as model architecture, image resolution, training methods, data quality, and specific application scenarios (Chaturvedi, 2008; Zhao *et al.*, 2023). Therefore, continued review and research are essential for understanding how model architectures perform under various conditions, the best practices in training that lead to reliability and performance, and the limitations and challenges of current models used to identify trees from aerial and satellite images.

Many useful reviews have focused on the applications, algorithms, techniques, challenges and opportunities, and future directions and emerging trends of traditional machine learning and deep learning for remote sensing (Y. N. Chen *et al.*, 2023; de Galiza Barbosa *et al.*, 2022; Janga *et al.*, 2023; L. Ma *et al.*, 2019; Manogaran *et al.*, 2020; Zhong *et al.*, 2024). The reviewed papers mostly focused on classification via semantic segmentation, which often suffers from blurry boundaries and the loss of individual object details. There is a gap in reviews on applications, for instance segmentation of tree species and ecosystem influences.

This review sheds light on the global potential of AI models, for instance segmentation of individual tree species. An examination of the use of these models in various geographic regions and their ability to identify a wide range of tree species was undertaken. The review also compares the different machine learning models used for species identification and performs a meta-analysis of their confusion matrix based on the method, algorithm, and species choice.

3.2 Methods

3.2.1 Literature Search

A comprehensive literature search was performed in ScienceDirect, Taylor and Francis, and ProQuest to identify relevant articles published in English from January 1, 2015, to January 15, 2023. The start year for the review 2015 corresponds to the period when deep learning became recognized as a dominant in machine learning (Adedokun, 2019). It achieved landmark results in image recognition, speech processing, and natural-language tasks, which triggered a surge in deep-learning papers and captured the bulk of the mature, widely cited deep-learning literature (LeCun *et al*., 2015). The search criterion was (tree species AND identify AND UAV AND RGB NOT (pest OR disease OR health OR soil)). Acronyms were used in the search criteria to accommodate search engine character limits while maintaining a consistent query across databases. Using full terms would have restricted the number of keywords included and reduced coverage. Given that acronyms are widely used in remote sensing and related literature, their inclusion ensured that relevant studies were effectively captured, resulting in broad and representative coverage. Out of 224 abstracts, 221 were retrieved, and duplicate records were deleted. The remaining records were further screened for potential eligibility by titles and abstracts. The full texts of all the screened articles were manually reviewed for final selection based on the

Preferred Reporting Items for Systematic Reviews and Meta-Analysis (PRISMA) procedure (Page *et al.*, 2021). Fourteen (14) other articles were added from Google Scholar and other websites to support qualitative analysis.

All original articles of cross-sectional studies that identified tree species from high-resolution satellite and unmanned aerial vehicle (UAV) images were included, provided that they reported the confusion metrics of the machine learning algorithms used. Multiclass prediction models that provided sufficient information to derive a confusion matrix for each class were included. Articles that reported accuracy metrics other than the confusion matrix were excluded to avoid multiple counts if the samples were not as independent as expected.

After the screening, 14 supplementary articles and 11 studies containing 23 machine learning algorithms and architectures and 155 deployments were included for qualitative and quantitative analysis (Figure 3.1).

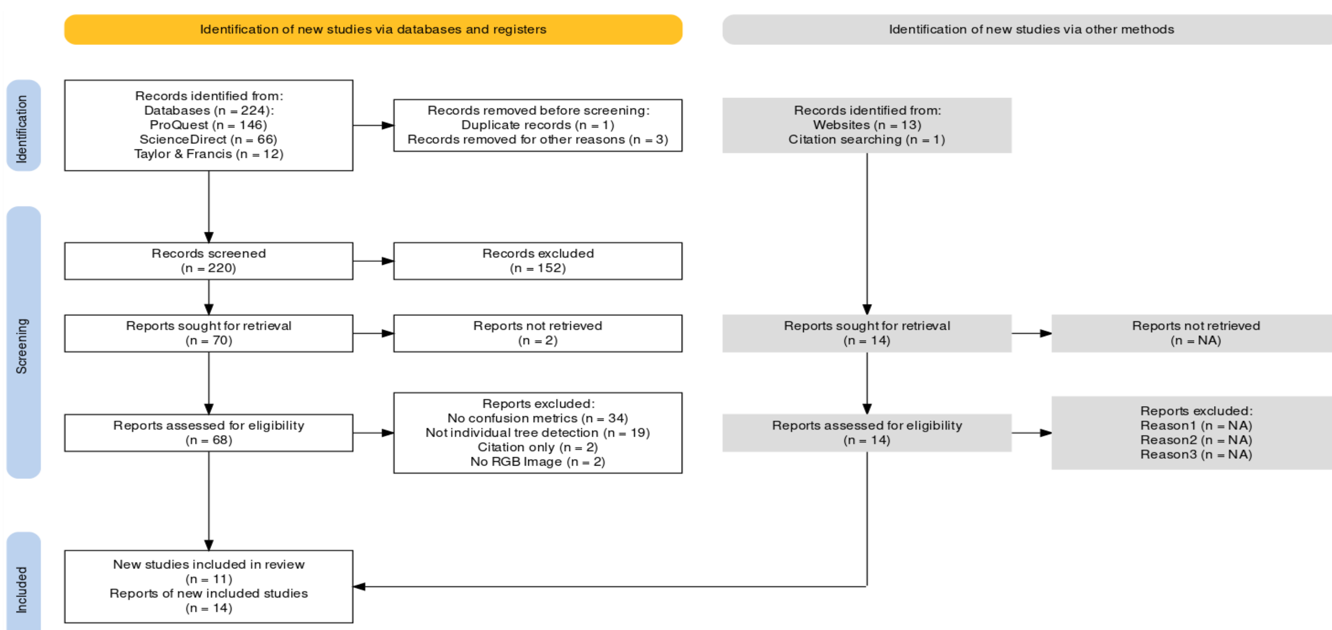

Figure 3.1: PRISMA Flow Diagram for Study Selection

3.2.2 Data Extraction and Description

The data was extracted into a pre-designed Excel template. The variables obtained included article title, authors, year of publication, continent of study, country of study, study objective, camera platform, image type, image resolution, data training and testing method, tree species, information about the models, site, and accuracy metrics such as true positive (TP), false positive (FP), false negative (FN), and true negative (TN) counts. When an article tested more than one model, species, or dataset, all the metrics (contingency tables) were extracted, provided that each test and its samples were independent. Further information about the climate of the geographical area and the family and order of the species under investigation was obtained to support qualitative analysis.

3.2.3 Comparison of TML and DL Model Accuracies

A total of 155 confusion matrices were extracted from the literature: 21 based on pixel counts and 134 based on individual tree counts. Of these, 10 were normalized matrices, and 18 had true positive (TP) values of 0, which were excluded from the analysis. A total of 127 case studies were chosen for analysis and categorized into two groups: deep learning (DL = 101) and traditional machine learning (TML = 26) to assess the effect of model category on accuracy. They were organized by article, model, and taxonomic order to evaluate the influence of study design, model type, and taxonomy on accuracy.

The sensitivities and specificities were pooled and analyzed by Bayesian meta-analysis using the bamdit package in R. The correlation between sensitivities and the probability of correct classification (PCC) was computed for analysis. The PCC represents the area under the Bayesian summary receiver operating characteristic (BSROC) curve.

3.3 Results and Discussion

3.3.1 Data Extraction and Description

3.3.1.1 Characteristics of the Content of Articles

The trends of eleven articles were analyzed, as shown in Figure 3.2. Most articles on the subject matter were published in 2020 and 2021, with the fewest occurring in 2019 and 2022. This trend could be attributed to easy access to satellite and drone images and advances in DL, as they provided a good basis for minimally interactive (i.e., UAV, satellite, and forest-based) research to thrive. Although interest in the use of ML in remote sensing has recently gained momentum, there is relatively little use in specific applications, such as individual tree detection (Ghanbari *et al.*, 2021), because of the further complexity that is imposed on the task of instance segmentation by variations in tree size, shape, shadow, lighting, and overlapping canopies.

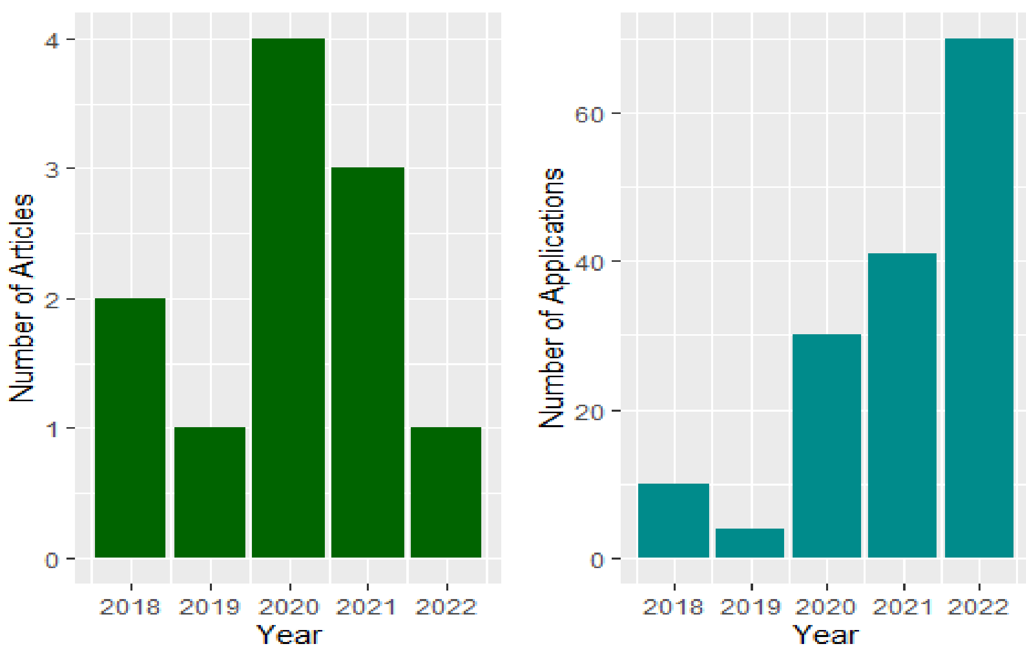

Figure 3.2: Frequency of Articles and Applications of Case Studies with Models

There were 11 articles from 6 countries across 5 continents and 8 climate zones. Five articles were from Brazil, 2 from Finland and China, and 1 from Canada and the Kingdom of Tonga. The climate zones were tropical rainforest, tropical monsoon, humid continental, humid subtropical, subarctic, tropical zone with dry winters, tropical rainforest, and tropical savanna. In all, 23 machine learning algorithms and architectures were used to identify tree species as case studies, and the applied methodologies differed. There were 20 deep learning architectures, and 3 traditional machine learning algorithms used (Table 3.1).

Table 3.1: Continents and Countries where the Models were used.

Continent	**Countries**	**Citation**	**Models**	**Model Class**
Asia	China, Thailand	Li *et al.* (2022) Dong *et al.* (2018)	1) ResNet50-FPN, 2) ACNet, 3) ACNet-Laplace, 4) ACNet-Sobel, 5) Cascade-NN	DL
Europe	Finland	Mäyrä *et al.* (2021) Ouattara *et al.* (2020)	1) RF, 2) LightGBM, 3) SVM, 4) ANN 5) 3D-CNN, 6) Faster R-CNN	TML, DL
North America	Canada	Chabot *et al.* (2018)	RF	TML
Oceania	Kingdom of Tonga	Saldana Ochoa and Guo (2019)	YOLO	DL
South America	Brazil	Ferreira *et al.* (2020) Ferreira *et al.* [18] Miyoshi *et al.* (2020) Moura *et al.* (2021) Torres *et al.* (2020)	1) ResNet18 2) ResNet50 3) MobileNet V2 4) U-NET 5) SegNet 6) FC-DenseNet 7) DeepLabV3 8) R-CNN 9) DeepLabV3-MobileNetV3 10) ResNet18-DeepLabV3 11) CP-WSS 12) RF	DL, TML

3.3.1.2 Study Methods

Most studies have developed workflows and methods or compared models and experimental outcomes for accuracy. They also assessed the impact of tree characteristics on detection accuracy and either developed or modified existing DL architectures (Table 3.2).

Table 3.2: Overview of Study Objectives, Relevant Articles, Model-to-Species Relationships, and Data Utilized

Study Objective	**Articles**	**Model-to-species relationship**	**Data Used**
Development of workflows or methods for species detection	Chabot *et al.* (2018), Dong *et al.* (2018), Ferreira *et al.* (2020), Ouattara *et al.* (2020)	One-to-many Many-to-one	Hyperspectral, Multispectral, RGB, CHM
Comparison of model performance	Chabot *et al.* (2018), Ferreira *et al.* (2020), Miyoshi *et al.* (2020), Moura *et al.* (2021), Ochoa and Guo (2019)	One-to-many	Hyperspectral, RGB
	Li *et al.* (2022), Mäyrä *et al.* (2021)	Many-to-many	RGB, CHM
	Dong *et al.* (2018), Torres *et al.* (2020)	Many-to-one	RGB, Raw RGB
Evaluation of seasonal effects on model performance	Miyoshi *et al.* (2020)	One-to-many	Hyperspectral
Improvement of deep learning architectures	Li *et al.* (2022)	Many-to-many	RGB, CHM
Impact of canopy and leaf structure	Moura *et al.* (2021)	One-to-many	RGB

Four articles, Chabot *et al.* (2018), Dong *et al.* (2018), Ferreira *et al.* (2020), and Ouattara *et al.* (2020) focused on the development of a workflow or method for the detection of species from drone images. These articles achieved excellent performance on above-water and ground species. The case studies were conducted in five (5) climate zones: tropical savanna, rainforest, humid continental, subtropical, and subarctic. High-resolution RGB images were used to identify species for training the models in the four articles. Canopy height models (CHMs) and RGB images effectively detected individual tree crowns (ITCs). The kernel size for extracting textural features varied in the random forest model, and slight variations from the optimal size resulted in significant differences in accuracy. On the other hand, variations in model parameters (number of trees and maximum depth of trees in the RF algorithm) did not lead to significant differences. (Chabot *et al.*, 2018).

Comparison studies were used to evaluate the performance of a single model for the identification of a single tree species across seasons (Ouattara *et al.*, 2020). Another focus was on evaluating a single model's performance in identifying multiple tree species (Chabot *et al.*, 2018; Ferreira *et al.*, 2020; Miyoshi *et al.*, 2020; Moura *et al.*, 2021; Ochoa and Guo, 2019) and comparing different models for identifying multiple tree species (Li *et al.*, 2022; Mäyrä *et al.*, 2021). Dong *et al.* (2018) and Torres *et al.* (2020) also evaluated how well different models could identify single tree species. The case studies were mainly conducted in tropical savanna, rainforest, humid continental, subtropical, and subarctic climatic zones. A single CNN model used to identify many species in red, green, and blue (RGB) mosaic images achieved very high detection accuracy (Moura *et al.*, 2021). This was because the CNN model used did not require feature engineering, as it could self-learn the underlying patterns of the data.

Several deep learning (DL) and traditional machine learning (TML) models were used to detect many species from hyperspectral images. Only one article used raw RGB images for training (Torres *et al.*, 2020). Overall, deep learning methods outperformed traditional machine learning methods due to feature extraction challenges in machine learning. Automatic feature extraction is the major advantage of deep learning. A comparison of five deep learning models for the instance segmentation of a single species with slight modifications in model architecture (Torres *et al.*, 2020) revealed small improvements over instances where various models were used for the identification of multiple species. This outcome was expected because of the greater challenges in obtaining the right training dataset and distinguishing similar trees in multiclass detections. High-accuracy DL models have poor computational efficiency (Torres *et al.*, 2020). Generally, as the number of classification classes (tree species) increased, detection accuracy declined (Miyoshi *et al.*, 2020).

Canopy and leaf structure influence the spectral and spatial features captured by UAV imagery, directly affecting the accuracy of tree species detection in predictive models (Moura *et al.*, 2021). The characteristic patterns of trees are obtained from UAV images for network training, and high-resolution images are more effective for this purpose. An article from Brazil used the random forest algorithm to evaluate how spectral information from different seasons affects detection accuracy (Miyoshi *et al.*, 2020). Changes in the spectra of some species significantly impacted detection performance due to the influences of weather patterns.

Efforts to improve the existing DL architecture to enhance feature extraction were reported by Li *et al.* (2022). They introduced an attention-complementary network to replace the feature extractor in Mask R-CNN. They also incorporated an edge detection feature and evaluated the performance by testing different model configurations, varying data input types, backbone feature extraction networks, and edge detection filters for single tree species detection. The images used were mosaic RGB, CHM, or both. Models that used RGB and CHM as inputs outperformed those that used only CHM or RGB.

Supervised training is the preferred method for object detection and image classification. This was demonstrated in various case studies. The TML algorithm and DL architecture were trained using manually outlined trees and background samples to create a classifier that could accurately differentiate between trees. Data augmentation and transfer learning were effective for enhancing training efficiency and reducing time in DL. Shadows were significant in tree detection, although there is disagreement about their usefulness in the identification process. Ferreira *et al.* (2021) used a supervised deep CNN to localize and classify species. They acknowledged that shadows were a crucial discriminative feature, but Moura *et al.* (2021) observed greater classification errors due to overlapping canopies and shadows in images. The combination of mosaic RGB and CHM provided higher detection accuracy.

3.3.1.3 Tree Species Identified

The physical form and external structure of trees provide a good basis for grouping them into order and family (Streich and Todd, 2014). Similarly, computer vision depends on morphology and other tree characteristics to detect and classify them. The tree species observed in this study were grouped by order and family to provide a broader basis for discussion.

In total, 37 tree species from 16 orders and 19 families were recorded, as presented in Figure 3.3 and Table A 2.1 (Appendix). Six species were put in the class "Unknown" because they could not be identified by their labels (i.e., soft broads, background, floating, emergent, and submerged vegetation). The Fabaceae family was the most studied (28) of the tree species, followed by those in the Pinaceae (25). This trend could be driven by ecological and economic factors.

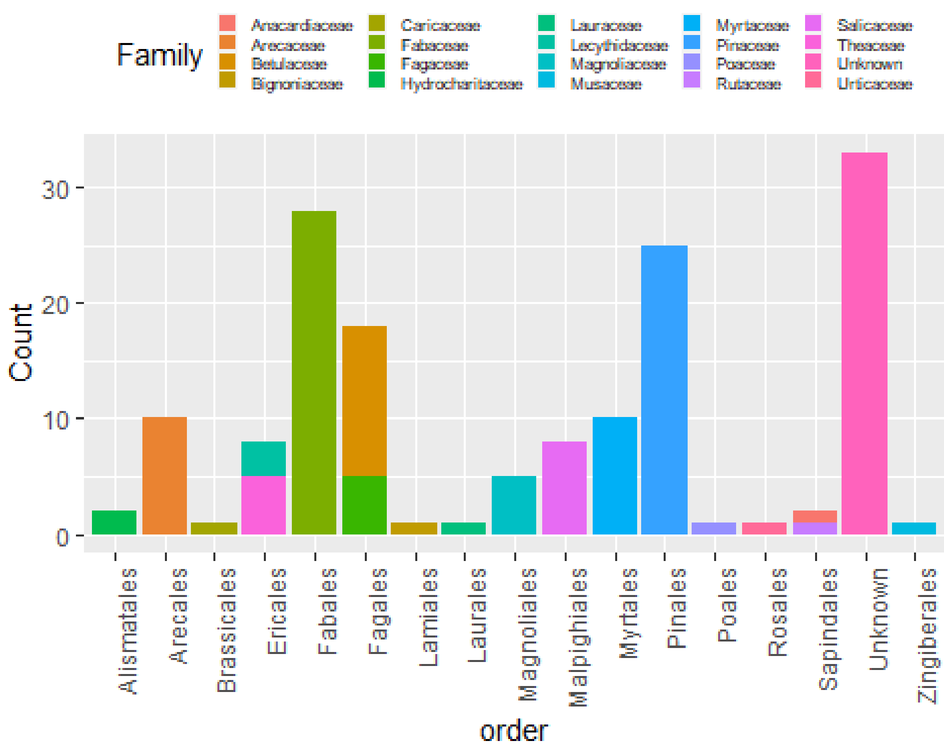

Figure 3.3: Number of Tree Species in Case Studies Grouped by Order and Family.

The main orders observed among the tree species were Fabales, Pinales, and Fagales, accounting for at least 46 % of the species, leaving 54 % of the remaining 14, Table A 2.1 (Appendix).

Four articles studied 27 % of the tree species (10) from the order Febales in the family Fabaceae (legumes), *Acacia melanoxylon*, *Dipteryx alata*, *Apuleia leiocarpa*, *Copaifera langsdorffii*, *Hymenaea courbaril*, *Inga vera*, *Pterodon pubescens*, *Anadenanthera* sp., *Bauhinia acreana*, and

Hymenaea courbaril in 28 case studies, Table A 2.1 (Appendix). The species in Fabales, the family of Fabaceae, referred to as the bean or pea family, consists of herbs, shrubs, trees, or vines that may have spines. The leaves of these plants are usually compound and sometimes simple. They have flowers and mostly legume fruits. These species are common in parts of Africa and Australia (Simpson, 2019) and include the *Parkia biglobosa*. Species detection from aerial images in this order and class is generally difficult because of the wide variations in size and shape. Small herbs and shrubs may be partially occluded by other plants or structures in the environment. Larger trees with recognizable features, such as leaves, branches, and outstanding canopy shapes, are comparatively easier to detect. Nonetheless, the difficulty associated with detection may increase when canopies smoothly merge into their backgrounds in the wet season with green undergrowth.

Four species constituting 11 % of the total species studied were from the order Pinales and the family Pinaceae. Three articles studied *Pinus elliottii*, *Picea abies* (Norway spruce), *Pinus sylvestris* (Scots pine), and *Picea* spp. (young spruce), Table A 2.1 (Appendix). The members of the order Pinales are often termed conifers. They are woody plants and are mostly the principal trees of forests worldwide (Zanoni and Axsmith, 2020). Pine, spruce, cedar, and redwood are examples. Structurally, their leaves are simple, shed singly, alternate, and spirally arranged. These infections are common in North America, Europe Asia, and North Africa (Weakley, 2012). Since conifers also vary in shape and size, identifying them from aerial images is difficult; however, these plants have unique structures that make them easy targets for detection from a combination of aerial RGB images and point clouds. The pine family, which is the most widespread, is easy to detect because of the arrangement of its leaves.

In the order Fagales, 18 case studies of 8 % of the species (3) were split between 2 families, Betulaceae, *Betula alnoides, Betula pubescens* and *Betula pendula,* and Fagaceae, *Castanopsis hystrix*. The species were studied in 2 articles, Table A 2.1 (Appendix). *Betula* consists of monoecious trees or shrubs. Structurally, their leaves are simple, deciduous, and usually spiral, with toothed margins. These plants bear flowers and produce nuts as fruits. According to Simpson (2019), they are often found in northern temperate and mountainous tropical regions. Success in detecting birch trees has largely been due to the size and quality of training samples and the inclusion of contextual information, such as the shape and texture of surrounding vegetation.

The accuracy of plant detection from aerial RGB images and point clouds depends on several factors, including the quality of the datasets, the presence of contextual information, the complexity of species characteristics and structure, the extent of occlusion, and the choice of algorithm. Good results in detection are usually achieved through a combination of deep learning and image processing techniques.

3.3.1.4 Model Architecture and Backbone Network

The articles evaluated different deep learning (DL) architectures and backbone combinations for detecting individual tree species, Table A 2.1 (Appendix). In 28 case studies from one article, architecture enhancements were made in edge detection using the Sobel and Laplace filters (Li *et al.*, 2022). Basic data augmentation techniques such as cropping, flipping, and rotating images were commonly applied.

A backbone is a feature extractor network that is the key component of a CNN model (Zhao *et al.*, 2023). Different backbone networks with various architectures were used in these studies. ResNet-

18 was the most frequently used backbone. Occasionally, ResNet-50, AceNet, Densnet, Xception, mobile V2/V3, or InceptionV2 were also used. The backbones were used with architectures such as the Attention Complementary and Edge Detection Region-based Convolutional Neural Network (ACE R-CNN), Faster R-CNN, Mask R-CNN, and DeeplabV3+. Fully Convolutional Network (FCN) with Conditional Random Fields (CRF), 3D-CNN, and You Only Look Once (YOLO) (Table 3.3).

Table 3.3: Summary of Model Architecture and Backbone

Architecture	**Backbone**
ACE R-CNN	ACNet
DeepLabv3+	ResNet-18, ResNet-50, MobileNetV2, IRU Encoder, Xception, MobileNetV3
Faster R-CNN	InceptionV2
FCN=CRF	U-Net, SegNet, FC-DenseNet
Mask R-CNN	ResNet-50

The ACE R-CNN with AceNet as its backbone was used for individual tree species identification (Li *et al.*, 2022). Compared with the Mask R-CNN, which had a ResNet backbone, and the Faster R-CNN, which had an InceptionV2 backbone, the ACE R-CNN with the Sobel filter performed best. Other architectures, such as the 3D CNN and YOLO, achieved reasonably high accuracy, although they did not outperform the ACE R-CNN using the Sobel edge filter. Similarly, the FCN-CRF architecture with the FC-DenseNet backbone also showed competitive performance.

Traditional machine learning: TML algorithms such as random forest (RF), light gradient boosting machine (GBM), support vector machines (SVMs), and maximum likelihood criteria (MLC) have been successful in image classification. However, they were mostly outperformed by DL methods. Nonetheless, they are efficient at managing computer resources and time. Feature creation and extraction are operator-dependent, and that is a major disadvantage. Compared to other TMLs, the SVM performed better in terms of pine classification. Where hyperspectral images were used, the RF and GBM methods did not require normalization of the input reflectance (Mäyrä *et al.*, 2021). The RF model performed better than the MLC model on the same dataset.

3.3.2 Comparison of DL and TML Accuracies

There were 101 deep learning (DL) models and 26 traditional machine learning (TML) models utilized across the reviewed studies. However, these models were built upon a smaller set of core base architectures, which were modified or combined as a backbone to suit specific tasks or datasets (Table 3.4).

Table 3.4: Categorization of Models

Category	**Models**
Deep Learning	ACNet, Cascade-NN, 3D-CNN, Faster R-CNN, Mask-RCNN, ACE R-CNN, YOLO ResNet18, ResNet50, MobileNetV2, U-Net, SegNet, FC-DenseNet, DeepLabV3, R-CNN DeepLabV3, MobileNetV3, CP-WSS1
Traditional Machine Learning	Random Forest (RF), LightGBM, SVM, ANN

The sensitivity, specificity, and probability of correct classification (PCC) were assessed to evaluate how well the model made correct classifications. The DL models showed a positive correlation (0.434) between sensitivity and specificity, with mean values of 89.8 % and 94.6 %, respectively. In contrast, the TML models exhibited a negative correlation (-0.064) between the metrics, with a pooled sensitivity of 72.3 % and specificity of 93.4 %.

The probability that a DL model correctly classified a species was 84.9 %, indicating a good likelihood of correctly identifying species. The TML models had a lower mean classification probability of 70.6 %, reflecting moderate performance in correctly identifying species. Generally, the TML models performed well with smaller datasets, while DL models typically needed much larger datasets for optimal performance.

3.3.2.1 Model accuracy analyzed by study, model type, and species order groups.

The deep learning dataset showed a positive correlation between pooled sensitivity and specificity in all the studies, except for that of Mäyrä *et al.* (2021). High probabilities of correct classification (> 80.0 %) were observed across all studies. TML model sensitivity mostly had a negative correlation with specificity, except for the studies of Chabot *et al.* (2018). The specificity values were generally high, with a lower probability of correct classification (PCC) observed in Miyoshi *et al.* (2020) (Table 3.5).

Table 3.5: Summary of Model Accuracies Grouped by Article for Assessing the Influence of Study Design on Detection Accuracy.

Article	Deep Learning				Machine Learning			
	SEN	SPE	PCC	CORR	SEN	SPE	PCC	CORR
Li *et al.* (2022)	0.894	0.935	0.842	0.746				
Ferreira *et al.* (2020)	0.838	0.937	0.809	0.722				
Moura *et al.* (2021)	0.905	0.982	0.884	0.131				
Mayra *et al.* (2021)	0.852	0.952	0.831	-0.247	0.679	0.905	0.644	-0.560
Chabot *et al.* (2018)					0.866	0.945	0.85	0.300
Miyoshi *et al.* (2020)					0.496	0.923	0.486	-0.017

When grouped by models, the ACE R-CNN with Laplace and Sobel filters and Faster R-CNN-FPN had the highest sensitivity and specificity, and PCC values greater than 85 %. The sensitivity of the mask R-CNN was low, and it points to a high threshold, class imbalance, poor annotation quality, or poor parameter tuning (Table 3.6).

Table 3.6: Summary of Model Accuracies Grouped by Model Type for Assessing the Influence of Model Choice on Detection Accuracy.

Model	Deep Learning				Machine Learning			
	SEN	SPE	PCC	CORR	SEN	SPE	PCC	CORR
DeepLabv3+(ResNet-18)	0.816	0.905	0.804	0.567				
MaskR-CNN	0.380	0.842	0.39	0.171				
ACER-CNN	0.938	0.930	0.912	-0.181				
ACER-CNN-Laplace	0.966	0.949	0.951	0.240				
ACER-CNN-Sobel	0.996	0.993	0.986	0.231				
FasterR-CNN-FPN	0.905	0.982	0.883	0.112				
3D-CNN	0.856	0.953	0.83	-0.304				
Random-Forest					0.741	0.940	0.719	0.074

Within the taxonomic order group, all probabilities of correct classification were greater than 80 % (PCC values > 0.80). The diagnostic criteria for Ericales, Fabales, Pinales, and Malphighiales had high sensitivity and specificity. All the others were between 70.0 % and 80.0 % (Table 3.7).

Table 3.7: Summary of Model Accuracies Grouped by Taxonomic Order for Assessing the Influence of Order on Detection Accuracy.

Order	Deep Learning				Machine Learning			
	SEN	SPE	PCC	CORR	SEN	SPE	PCC	CORR
Arecales	0.789	0.927	0.786	0.533				
Ericales	0.822	0.902	0.83	0.725				
Fagales	0.741	0.924	0.735	0.817				
Magnoliales	0.724	0.709	0.745	0.150				
Fabales	0.838	0.968	0.848	0.626				
Unknown	0.808	0.944	0.792	0.525	0.855	0.901	0.842	0.220
Myrtales	0.763	0.864	0.766	0.758				
Pinales	0.884	0.890	0.866	0.140	0.783	0.889	0.768	0.334
Malpighiales	0.836	0.981	0.812	0.015				

The analysis of works by Chabot *et al.* (2018) suggested that ML models were useful for identifying individual tree species. Reasonably high metrics and PCC values were observed. Other sensitivity and specificity values from the group analysis of the ML models were low.

3.4 Conclusion

This study reviewed current state-of-the-art methods of detecting individual tree species to disclose how TML and DL models were applied. The models were applied globally in eight climate zones: tropical savanna, rainforest, humid continental, subtropical, subarctic, tropical monsoon, humid subtropical, and tropical zone with dry winters. These zones vary in temperature and precipitation, affecting vegetation and ecosystems.

RGB and canopy height model (CHM) data were the most common and familiar forms of visual data, mostly obtained through remote sensing. RGB images are significantly more valuable than point clouds for selecting training samples for the annotation and final detection of tree species. Nonetheless, their combination results in better detection accuracy, and this synergy can be seen when CHMs formed from point clouds are used with RGB images for individual tree detection.

Although there is a growing interest in using machine learning for analyzing remotely sensed images and their point clouds, its application in individual tree detection is still relatively low. On the few occasions when individual trees were studied, most focused on the order, family, and species with high ecological and economic importance, such as *Acacia melanoxylon* in the order of legumes, or outstanding physical characteristics, such as *Pinus elliottii* in the order of Pinales.

Modified models like the ACE R-CNN with the Sobel edge detection filter excel in individual tree detection, achieving 99.6 % sensitivity, 99.3 % specificity, and a Bayesian area under the curve of 98.6 %. However, accuracy varies when detecting tree species from different families, orders, or environments, suggesting an influence of external factors on model performance. Accuracies were generally lower where a model was applied in multiclass (species) segmentation.

DL models generally outperform traditional machine learning models due to their ability to automatically engineer useful features that help in species detection, a task that is often manual in TML models. However, since the non-performance of TMLs is not due to the limitations of the algorithms but rather to the ability to engineer useful features for the model to detect species, TML algorithms such as SVM and RF will remain relevant in individual tree detection. Coupled with the advantages of speed and accurate detection in the face of relatively small training data, these methods are strong rivals or complements of DL models.

References

Adedokun, O. G. (2019). Deep learning—An overview. *Journal of Electrical & Electronic Systems, 8*(1), 302.

Brandt, M., Tucker, C. J., Kariryaa, A., Rasmussen, K., Abel, C., Small, J., Chave, J., Rasmussen, L. V., Hiernaux, P., Diouf, A. A., Kergoat, L., Mertz, O., Igel, C., Gieseke, F., Schöning, J., Li, S., Melocik, K., Meyer, J., Sinno, S., … Fensholt, R. (2020). An unexpectedly large count of trees in the West African Sahara and Sahel. *Nature*, *587*(7832), 78–82. https://doi.org/10.1038/s41586-020-2824-5

Chabot, D., Dillon, C., Shemrock, A., Weissflog, N., & Sager, E. P. S. (2018). An object-based image analysis workflow for monitoring shallow-water aquatic vegetation in multispectral drone imagery. *ISPRS International Journal of Geo-Information*, *7*(8). https://doi.org/10.3390/ijgi7080294

Chaturvedi. (2008). *Factors Affecting the Performance of Artificial*. *85*(1943), 51–52.

Dong, T., Shen, Y., Zhang, J., Ye, Y., & Fan, J. (2019). Progressive cascaded convolutional neural networks for single tree detection with Google Earth imagery. *Remote Sensing*, *11*(15). https://doi.org/10.3390/rs11151786

Dong, T., Zhang, J., Gao, S., Shen, Y., & Fan, J. (2018). Single-tree detection in high-resolution remote-sensing images based on a cascade neural network. *Canadian Historical Review*, *7*(9). https://doi.org/10.3390/ijgi7090367

Ferreira, M. P., Almeida, D. R. A. de, Papa, D. de A., Minervino, J. B. S., Veras, H. F. P., Formighieri, A., Santos, C. A. N., Ferreira, M. A. D., Figueiredo, E. O., & Ferreira, E. J. L. (2020). Individual tree detection and species classification of Amazonian palms using UAV images and deep learning. *Forest Ecology and Management*, *475*, 118397. https://doi.org/10.1016/j.foreco.2020.118397

Ferreira, M. P., Lotte, R. G., D'Elia, F. V., Stamatopoulos, C., Kim, D. H., & Benjamin, A. R. (2021). Accurate mapping of Brazil nut trees (Bertholletia excelsa) in Amazonian forests using WorldView-3 satellite images and convolutional neural networks. *Ecological Informatics*, *63*, 101302. https://doi.org/10.1016/j.ecoinf.2021.101302

Ghanbari, H., Mahdianpari, M., Homayouni, S., & Mohammadimanesh, F. (2021). A meta-analysis of convolutional neural networks for remote sensing applications. *IEEE Journal of*

Selected Topics in Applied Earth Observations and Remote Sensing, *14*, 3602–3613. https://doi.org/10.1109/JSTARS.2021.3065569

Heydari, S. S., & Mountrakis, G. (2019). Meta-analysis of deep neural networks in remote sensing: A comparative study of mono-temporal classification to support vector machines. *ISPRS Journal of Photogrammetry and Remote Sensing*, *152*, 192–210. https://doi.org/10.1016/j.isprsjprs.2019.04.016

LeCun, Y., Bengio, Y., & Hinton, G. (2015). Deep learning. *Nature, 521*(7553), 436-444. *https://doi.org/10.1038/nature14539*

Li, Y., Chai, G., Wang, Y., Lei, L., & Zhang, X. (2022). ACE R-CNN: An attention-complementary and edge detection-based instance segmentation algorithm for individual tree species identification using UAV RGB images and LiDAR data. *Remote Sensing*, *14*(13). https://doi.org/10.3390/rs14133035

Mäyrä, J., Keski-Saari, S., Kivinen, S., Tanhuanpää, T., Hurskainen, P., Kullberg, P., Poikolainen, L., Viinikka, A., Tuominen, S., Kumpula, T., & Vihervaara, P. (2021). Tree species classification from airborne hyperspectral and LiDAR data using 3D convolutional neural networks. *Remote Sensing of Environment*, *256*. https://doi.org/10.1016/j.rse.2021.112322

Miyoshi, G. T., Imai, N. N., Tommaselli, A. M. G., de Moraes, M. V. A., & Honkavaara, E. (2020). Evaluation of hyperspectral multitemporal information to improve tree species identification in the highly diverse Atlantic forest. *Remote Sensing*, *12*(2), 1–22. https://doi.org/10.3390/rs12020244

Moura, M. M., de Oliveira, L. E. S., Sanquetta, C. R., Bastos, A., Mohan, M., & Corte, A. P. D. (2021). Towards Amazon forest restoration: Automatic detection of species from UAV imagery. *Remote Sensing*, *13*(13), 1–16. https://doi.org/10.3390/rs13132627

Ochoa, K. S., & Guo, Z. (2019). A framework for the management of agricultural resources with automated aerial imagery detection. *Computers and Electronics in Agriculture*, *162*, 53–69. https://doi.org/10.1016/j.compag.2019.03.028

Ouattara, I., Hyyti, H., & Visala, A. (2020). Drone-based mapping and identification of young spruce stands for semiautonomous cleaning. *IFAC-PapersOnLine*, *53*(2), 15777–15783. https://doi.org/10.1016/j.ifacol.2020.12.205

Page, M. J., McKenzie, J. E., Bossuyt, P. M., Boutron, I., Hoffmann, T. C., Mulrow, C. D., Shamseer, L., Tetzlaff, J. M., Akl, E. A., Brennan, S. E., Chou, R., Glanville, J., Grimshaw, J. M., Hróbjartsson, A., Lalu, M. M., Li, T., Loder, E. W., Mayo-Wilson, E., McDonald, S., Moher, D. (2021). The PRISMA 2020 statement: An updated guideline for reporting systematic reviews. *British Medical Journal*, *372*. https://doi.org/10.1136/bmj.n71

Sheykhmousa, M., Mahdianpari, M., Ghanbari, H., Mohammadimanesh, F., Ghamisi, P., & Homayouni, S. (2020). Support vector machine versus random forest for remote sensing image classification: A meta-analysis and systematic review. *IEEE Journal of Selected Topics in Applied Earth Observations and Remote Sensing*, *13*, 6308–6325. https://doi.org/10.1109/JSTARS.2020.3026724

Simpson, M. G. (2019). Diversity and classification of flowering plants: Eudicots. In *Plant Systematics* (Vol. 366). https://doi.org/10.1016/b978-0-12-812628-8.50008-0

Streich, A. M., & Todd, K. A. (2014). Classification and naming of plants. *University of Nebraska-Lincoln Extension*, 8.

Torres, D. L., Feitosa, R. Q., Happ, P. N., La Rosa, L. E. C., Junior, J. M., Martins, J., Bressan, P. O., Gonçalves, W. N., & Liesenberg, V. (2020). Applying fully convolutional architectures for semantic segmentation of a single tree species in urban environment on high-resolution UAV optical imagery. *Sensors (Switzerland)*, *20*(2), 1–21. https://doi.org/10.3390/s20020563

Weakley, A. S. (2012). *Flora of the Southern by table of contents*. *November*, 898–903. http://www.herbarium.unc.edu/FloraArchives/WeakleyFlora_2015-05-29.pdf

Zanoni, T. A., & Axsmith, B. J. (2020). *Pinales*. https://doi.org/10.1036/1097-8542.517500

Zhang, C., Atkinson, P. M., George, C., Wen, Z., Diazgranados, M., & Gerard, F. (2020). Identifying and mapping individual plants in a highly diverse high-elevation ecosystem using UAV imagery and deep learning. *ISPRS Journal of Photogrammetry and Remote Sensing*, *169*, 280–291. https://doi.org/10.1016/j.isprsjprs.2020.09.025

Zhao, H., Morgenroth, J., Pearse, G., & Schindler, J. (2023). A Systematic review of individual tree crown detection and delineation with convolutional neural networks (CNN). *Current Forestry Reports*, *0123456789*. https://doi.org/10.1007/s40725-023-00184-3

CHAPTER FOUR

APPLICATION OF COMPUTER VISION AND MACHINE LEARNING IN THE MORPHOLOGICAL CHARACTERIZATION OF *ADANSONIA DIGITATA* FRUITS

4.1 Introduction

Native multipurpose tree species within the savanna ecological zone provide numerous ecosystem services (Gebauer and Luedeling, 2013). The *Adansonia digitata* (baobab) is one such native multipurpose species found in the savannas of West Africa.

The export value of *Adansonia digitata* fruits has increased over the last decade (Hyde *et al.*, 2017; The Commission of the European Communities, 2008; Welford and Breton, 2008), and opportunities for African markets have expanded. Despite their economic prospects, not all *Adansonia digitatas* are in high demand. According to Odoom (2021), fruit size varies from large to small and is an indicator of sweetness. Gurashi and Kordofani (2014) associated the shape of the fruit with its market value. Therefore, attributes such as size and shape can affect consumer preference and market value, both of which influence demand. This calls for the selection of suitable varieties for both marketing and propagation. As a result, researchers have intensified studies on the morphology of *Adansonia digitata* fruit to gain insight into how it impacts production, quality, and domestication potential (Egbadzor, 2020; Parkouda *et al.*, 2012; Sanchez *et al.*, 2011). Morphological variability in *Adansonia digitata* fruit shape in combination with the percentage of pulp weight is a possible criterion for selecting high-yield fruits (Gebauer and Luedeling, 2013) and Gurashi and Kordofani (2021), confirmed this assertion. Despite the usefulness of these findings, measuring the length and width of the fruit and their component weights using hand-operated tape and an electronic scale was manual, laborious, and time-consuming. This problem persists in most studies in industry (Gouwakinnou *et al.*, 2011; Gurashi and Kordofani, 2014; Mkwezalamba *et al.*, 2015)

The determination of suitable *Adansonia digitata* fruits for domestication and production by analyzing their morphological characteristics requires less labour-intensive methods for efficient and large-scale production. Mass and volume are useful in planning for sorting, storage, packaging, and transport (Fitriyah, 2022; Ifmalinda *et al.*, 2022). They directly affect storage and transport costs, which influence sales (Nyalala *et al.*, 2021). In agriculture, weight is often used as a proxy for size because of its relative ease of measurement compared with volume, but volume-based sorting is more efficient (Koc, 2007). Compared with mass, the volume of fruit is less affected by external factors such as moisture content. Because of the complexity associated with measuring the volume of irregular objects using geometry, fruit volume is commonly measured by gas or water displacement. Both methods are unsuitable for production because they are best conducted indoors and are time-consuming. In addition, the water displacement method (WDM) can have harmful effects on the quality of the fruit. It is therefore not surprising that information on the volume of *Adansonia digitata* fruit is scarce in the literature. A more efficient and less labourious process that is easily scalable and does not compromise fruit quality is needed to measure morphological characteristics.

Object detection is a common and challenging task in computer vision but can be implemented to characterize *Adansonia digitata* fruits by their mass and volume. The technique aims to locate instances of object classes in a specific image by colour and texture or otherwise (Zheng *et al.*, 2023). Previously, image processing techniques and computer vision have been effective at extracting the diameter, area, and perimeter of spherical objects (Fitriyah, 2022; Kheiralipour and Kazemi, 2020). In fruit grading or sorting by colour, texture, or morphological features, computer vision and regression present an intelligent alternative that can be achieved at scale in a cost-effective and timely manner (Raja Sekar L, Ambika N, 2018). In addition to other methods, these methods have been applied to determine the mass and volume of cherry tomatoes in Nanjing, Jiangsu Province, China (Nyalala *et al.*, 2019, 2021), and Thai apple ber, scientifically known as *Ziziphus mauritiana,* in Jodhpur, India (Mansuri *et al.*, 2022).

Food products are classified into axis-symmetric and non-axis-symmetric shapes (Siswantoro *et al.*, 2013). Thus, a product can be regarded as an axis-symmetric object if its cross-sections are circular, while perpendicular to its major axis (Nyalala *et al.*, 2019) and include cherry tomatoes, eggs, watermelons, lemons, limes, oranges, and tangerines. In contrast, axis-nonsymmetric fruits have different shapes that are affected by genetics and the environment (Fitriyah, 2022). In Kordofan, Sudan, Gebauer and Luedeling (2013) identified four *Adansonia digitata* fruit shapes: ventricose, crescent, globose, and fusiform. Gurashi and Kordofani (2014) expanded this classification by identifying nine additional shapes in the Blue Nile and North Kordofan States in Sudan: ellipsoid, high spheroid, ovate, obovate, oblong-pointed, spheroid-emarginate, ellipsoid-pointed, clavate, and rhomboid. Thus, the *Adansonia digitata* fruit is an example of a non-axial-symmetric fruit.

Various geometric models and numerical analysis methods have been used to extract volumes from 3D reconstruction of fruits from images obtained from different camera arrangements (Khojastehnazhand *et al.*, 2010; Koc, 2007; Nyalala *et al.*, 2019). Under the assumptions of axis-symmetric shapes, controlled fruit orientation, uniform lighting, and a simple background, very high levels of accuracy have been achieved using basic solids, solids of revolution, and conical frustum to estimate the mass and volume of fruits (Khojastehnazhand *et al.*, 2010; Koc, 2007). Nyalala *et al.* (2019) used a 3D Kinect Infra-Red Sensor, which was invariant to visible light conditions and had capabilities for depth estimation and ease of image segmentation to construct depth images to estimate the volume and mass of tomatoes. However, deviations from the assumption in a production environment can introduce errors in the estimates of the mass and volume of fruits. In addition, the assumptions of axis-symmetric shapes, controlled fruit orientation, uniform lighting, and simple background are difficult to achieve under real-world field conditions. These assumptions can affect the accuracy of the resulting models and their application in real-world situations. For example, Fitriyah (2022) reported poor to moderate accuracy when using single frontal-view images for non-axis-symmetric shapes.

This study aimed to develop a computer vision system to estimate the volume of non-axis-symmetric *Adansonia digitata* fruits from single-view RGB images captured in a setting where fruit orientation, lighting, and background are not controlled. The specific objectives were to investigate the variation in fruit morphological characteristics across the study areas, to analyze the Mask Region-based Convolutional Neural Network (Mask RCNN) and adapt it for the effective segmentation of *Adansonia digitata* fruits, to develop a 2D feature extraction algorithm, to develop a model to estimate volume, to investigate the relationship between mass and volume, and to extend point estimates of mass and volume to their distributions. The approach used to estimate the volume of fruits provides insights that can be used to optimize sorting, transportation planning, storage, and market pricing strategies to foster efficiency in production and transactions for sellers and buyers. Knowing the relationship between mass and volume in production planning can facilitate the estimation of storage space for fruits when their mass is known.

4.2 Materials and Methods

4.2.1 Study Area

The study was conducted in the savanna ecological zone of Ghana within the Nandom and Kasena–Nankana East municipalities. The Nandom Municipal is located in the Upper West Region, between Longitudes 2°41' W and 2°54' W and Latitudes 10°44' N and 11°00' N. The Kasena-Nankana East Municipal is located in the Upper East Region, between latitude 11°10' and 10°03' North and longitude 10°01' West (Figure 4.1). The monthly average temperatures ranged from 21°C to 32°C. The municipalities experienced a dry season from November to April and a rainy season from May to September/October (MoFA Ghana, 2022).

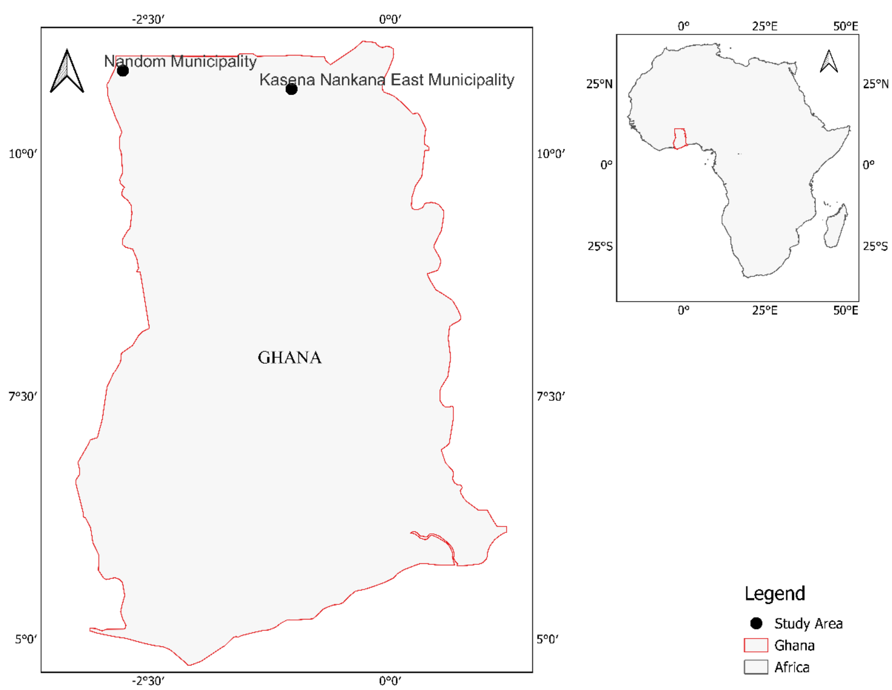

Figure 4.1: Study Area in Africa within the Savanna Ecological Zone of Ghana.

The soil types common to both study areas are Lixisols and Fluvisols. In addition, Nandom has Arenosols and Vertisols, and Kasena-Nankana has Leptosols (Soil Research Institute, 1999).

4.2.2 Study Species

Adansonia digitata plays a vital role, particularly in the food, cosmetic, and pharmaceutical industries (Egbadzor, 2020). It is a massive deciduous fruit tree, up to 20–30 m high, with a lifespan of several hundred years, and the trunk can be as broad as 3–7 m in diameter (Gray and Hayman, 1986). According to Odoom (2021), the fruit has an acidic tar flavor, surpasses spinach in calcium content, and sweet oranges in vitamin C. It is a 35 cm long and 17 cm diameter ovoid capsule with a woody envelope, black seeds, and chalky pulp when ripe. (Gray and Hayman, 1986).

4.2.3 Tree Sampling and Fruit Collection

Purposive sampling was used to select 43 mature, unharvested fruit-bearing *Adansonia digitata* trees within the savanna ecological zone. A total of 166 fruits were collected from the selected trees. Among these fruits, 101 were from 26 trees in the Nandom Municipality, and the remaining 65 were from 17 trees in the Kasena Nankana East Municipality. Differences in sample size across study sites reflect the variation in fruit availability, tree density, and accessibility, as only trees meeting the selection criteria were included. The harvesting techniques outlined by Odoom (2021) were used for fruit collection during the harvesting period in February and March. Three to four fruits were collected from the northeastern, southeastern, southwestern or northwestern quadrants of the tree crown. The fruits were collected from different parts of the crown to reduce bias, since variations in light and temperature within the canopy can affect fruit development and quality (Marcelis *et al*., 1998).

4.2.4 Measurement of Fruit Characteristics

Direct measurements of the volume and weight of the 166 fruits were taken. Each fruit was labeled with the study area code and identification number, which were maintained throughout the measurement process. All the measurements were taken at room temperature. The *Adansonia digitata* fruit was weighed to a precision of one gram. It was coated with Saran Wrap and submerged in water with a sinker rod of negligible volume, and the displaced water was collected in a measuring cylinder to record the volume in cubic centimeters (cm^3). Assuming the density of water to be 1 g/cm^3, the mass of each fruit was determined. The densities were calculated in grams per cubic centimeter (g/cm^3), as the ratio of mass to volume. The major lengths and maximum circumferences of the fruits were measured using a flexible tape with 0.10 cm precision.

4.2.4.1 The Computer Vision System

The conceptual framework of the proposed system takes an image of the *Adansonia digitata* fruit(s) as input. The fruits are detected and segmented (instance segmentation) by a modified Mask R-CNN model to address limitations caused by uncontrolled fruit orientation, shape, lighting, and background. The output is binarized, and two-dimensional (2D) features are extracted to estimate fruit volume or weight when the volume is known. The distribution of the sample is subsequently determined to extend the usefulness of the information from the point estimates for production planning (Figure 4.2).

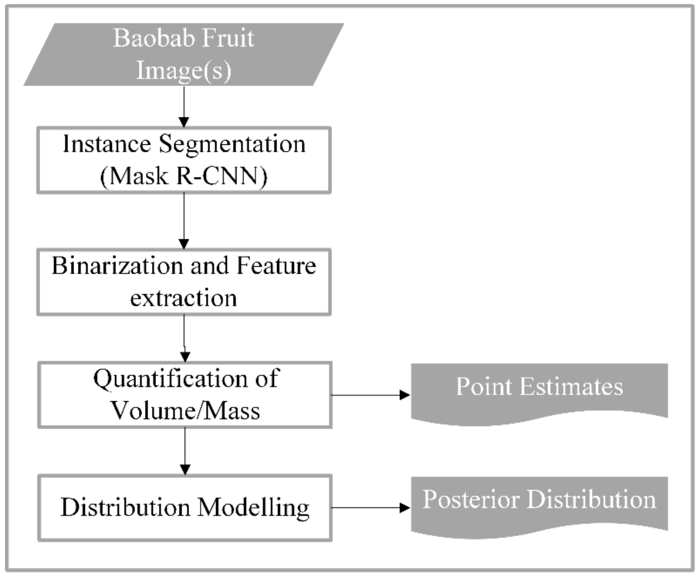

Figure 4.2: Conceptual Framework of the Proposed System

4.2.4.2 Instance Segmentation

An iPhone XS Max camera with a focal length of 4.25 mm and a resolution of 3024 × 4032 was used to capture all the images. The camera was placed at a fixed distance of 130 cm from the center of a white background with dimensions of 93 cm × 123 cm. Using the Nandom samples, images of different fruit counts were captured and down-sampled to a resolution of 381 × 503 pixels. They were subsequently annotated using the visual image annotator (VIA) by the visual geometry group (VGG) (Dutta and Zisserman, 2019). The annotations were converted to coco-style (Lin *et al.*, 2014) and split into training (80 %) and testing (20 %) datasets. The datasets were used to fine-tune the Mask RCNN for detection and instance segmentation (Figure 4.3). The ResNet-50 feature pyramid network (FPN) was used as the model backbone, and the initial weights for training were obtained from the Zoo model.

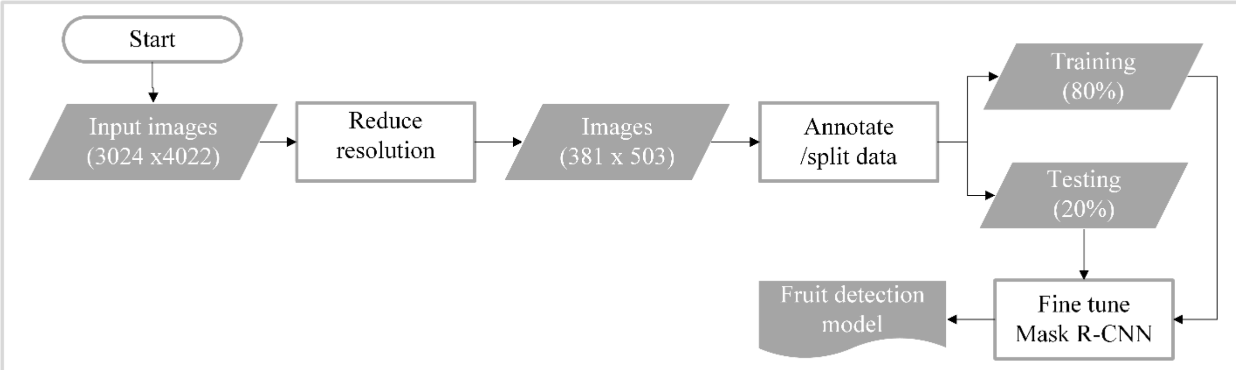

Figure 4.3: Training and Testing Procedure for Fruit Detection and Segmentation.

The accuracies of the models were evaluated using loss box regression, loss classification, loss mask, and mask accuracy. Loss box regression measures the model's ability to predict bounding boxes. Loss classification assesses the accuracy of class assignments to detected objects, and a loss mask is used to measure the accuracy of the pixel predictions. Lower values of the loss metrics were preferred. The mask accuracy represents the accuracy of the predicted segmentation mask, and higher values indicate better accuracy.

4.2.4.3 Image processing and feature extraction.

The fruits were grouped by study area, and without consideration of their arrangement relative to each other, they were photographed in groups of 1-25. The images were rotated 360° at 30° intervals and flipped left-to-right and up-to-down. The new dataset was fed into the trained Mask-RCNN model to detect and segment instances of the *Adansonia digitata* fruit regions to output a predicted mask image with a unique label assigned to each contiguous region. The predicted masks were converted to binary images of fruits and background and relabeled. The geometric and positional measures were extracted from the relabeled, binarized image using scikit-image to measure the region properties. The properties measured included (1) the segmented area, (2) the coordinates of the centroid, (3) the coordinates of the bounding box, (4) the equivalent diameter, and (5) the major diameter. The unique labels and extracted measurements of region properties were written to a Comma Separated Value (CSV) file (Figure 4.4).

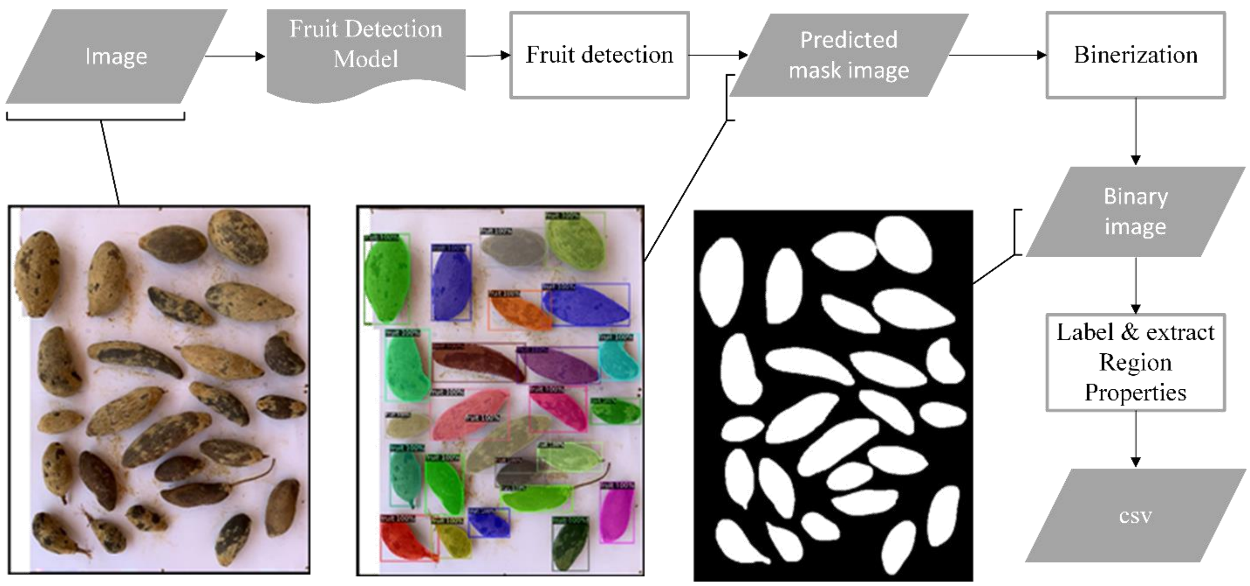

Figure 4.4: Instance Segmentation of an Image of *Adansonia digitata* Fruits to Produce a Predicted Mask Image for Two-Dimensional Feature Extraction.

Images with more than one fruit were used to assess the effectiveness of the segmentation process.

4.2.5 Quantification of Volume and Mass

The features extracted from single images obtained from Nandom were combined with their corresponding volumes from WDM to train and test the models, and likewise for records from Navrongo, which were used to validate the results. The CSV data from Section 2.4.2 was filtered to include only records obtained from single images. They were matched to their corresponding volume measurements from the WDM, separated by the study area. The data from Nandom were split into training (70 %) and testing (30 %) and applied to linear, polynomial, and radial implementations of support vector machines (SVMs) and random forest to derive suitable prediction models. The records from Navrongo were used to validate the models (Figure 4.5). The results were evaluated using the mean average error (MAE), root mean square error (RMSE), and R-squared (R^2) values.

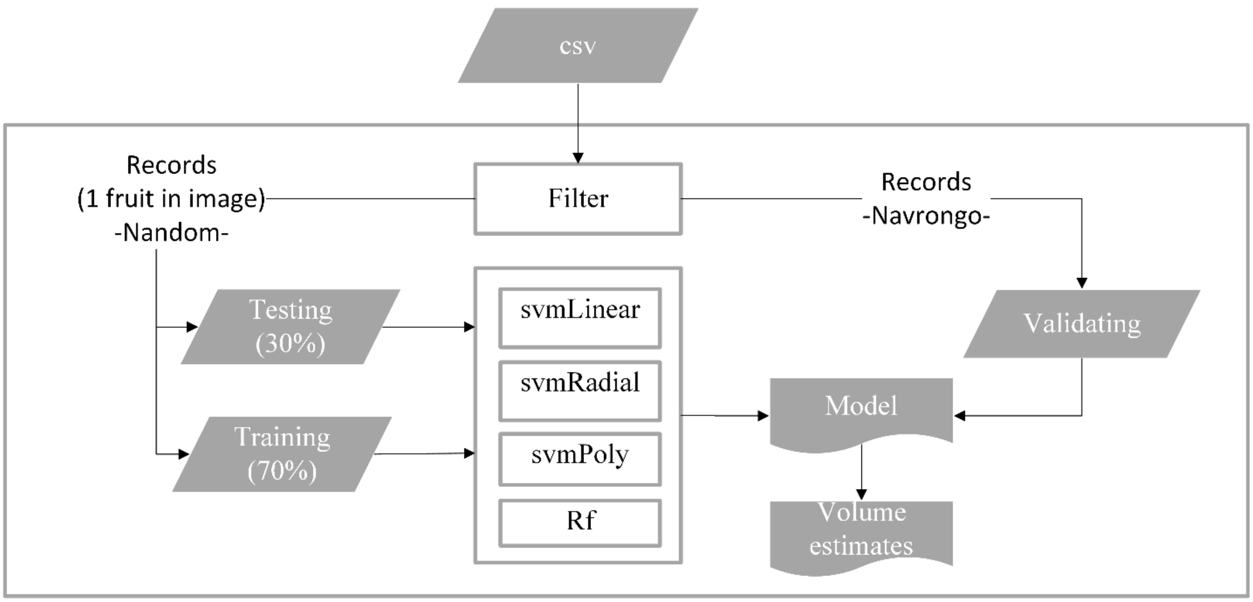

Figure 4.5 Training, Testing, and Validation Process for Volume Quantification Using Machine Learning.

4.2.5.1 Statistical Analysis

A paired t-test and the mean difference confidence interval approach were used to compare the volumes determined by each model (support vector machine and random forest) on the validation dataset with the volumes from the water displacement method. The Bland and Altman (1999) approach was used to plot the agreement between the *Adansonia digitata* fruit volume measured by the water displacement method and machine learning quantifications. The statistical analyses were performed in R.

4.2.6 Modeling Probability Density Functions

The bootstrap resampling technique was used with the distribution fitting package in R to estimate the probability density function for the sampling distribution of the means and standard deviations of fruit mass, volume, and density. The Akaike information criterion (AIC) and Bayesian information criterion (BIC) were used to select the best fit of the normal, exponential, gamma, logistic, Cauchy, Weibull, and log-normal probability density functions (PDFs). All the sampling distributions of the means were approximated to a normal distribution for simplicity. The best-fit distributions were used to define the Bayesian prior distribution for the mean (mu) and standard deviation (sigma). The prior distributions were used as a proxy for expert or industry knowledge of the population distribution of fruits. Arbitrary threshold values were set and used as industry standards to classify fruit mass, volume, or density as either small/low, medium, or large/high.

The process established the posterior distribution from point estimates from the fruit quantification models. The distributions provided insight into the confidence interval of point estimates and the probability of the sample belonging to a class (small/low, medium, or large/high) using the RStan package (Hoffman and Gelman, 2014; Stan Development Team, 2024) (Figure 4.6). The density was estimated as the ratio of mass to volume.

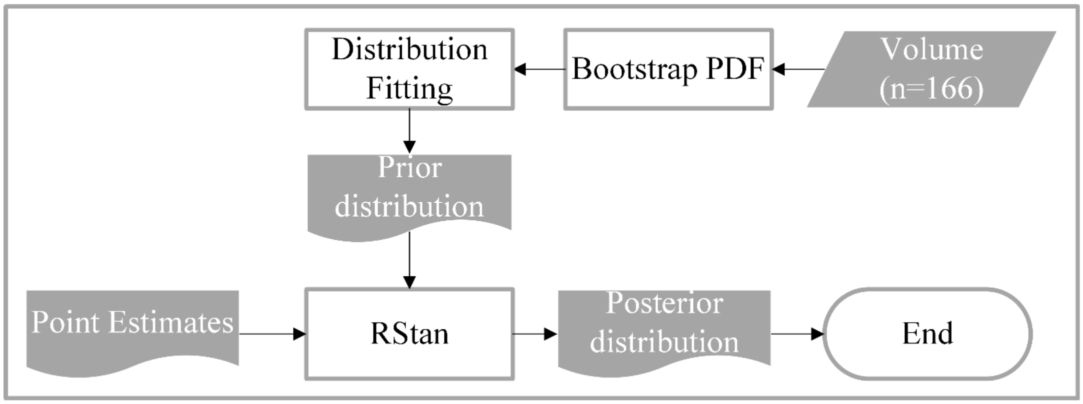

Figure 4.6 Volume Estimation and Distribution Modeling from New Images

4.3 Results and Discussion

4.3.1.1 Measurement of Fruit Characteristics

The samples showed notable morphological variation in shape, dominated by ventricose (45%) and fusiform (36%) , with fewer crescent (12%) and globose (8%) shapes. The volume varied from 150 cm³ to 1820 cm³, and the weight varied from 60 g to 640 g. The maximum length and circumference varied from 10 cm to 39 cm and 18.4 cm to 41 cm, respectively (Table 4.1).

Table 4.1: Summary Statistics of Measured Fruit Characteristics.

Statistic	Weight (g)	Volume (cm³)	Max. Length (cm)	Circumference (cm)
Min.	60	150	10.0	18.4
1st Qu.	150	423	19.0	24.0
Median	210	620	23.0	27.2
Mean	226	682	23.0	27.3
3rd Qu.	290	880	27.0	30.2
Max.	640	1820	39.0	41.0
Sd	0.109	0.339	5.811	4.535

The measured fruit characteristics of *Adansonia digitata* are consistent with values reported in the Sudanian, Sudano-Guinean, and Guinean zones of Benin, with variations caused by ecological and methodological differences (Assogbadjo *et al.,* 2006).

In general, the data from Nandom presented greater variation than the data from Navrongo. It completely overlapped the range of values from Navrongo, with variations in the frequency of occurrence. The distributions of all the observed parameters were skewed (Figure 4.7).

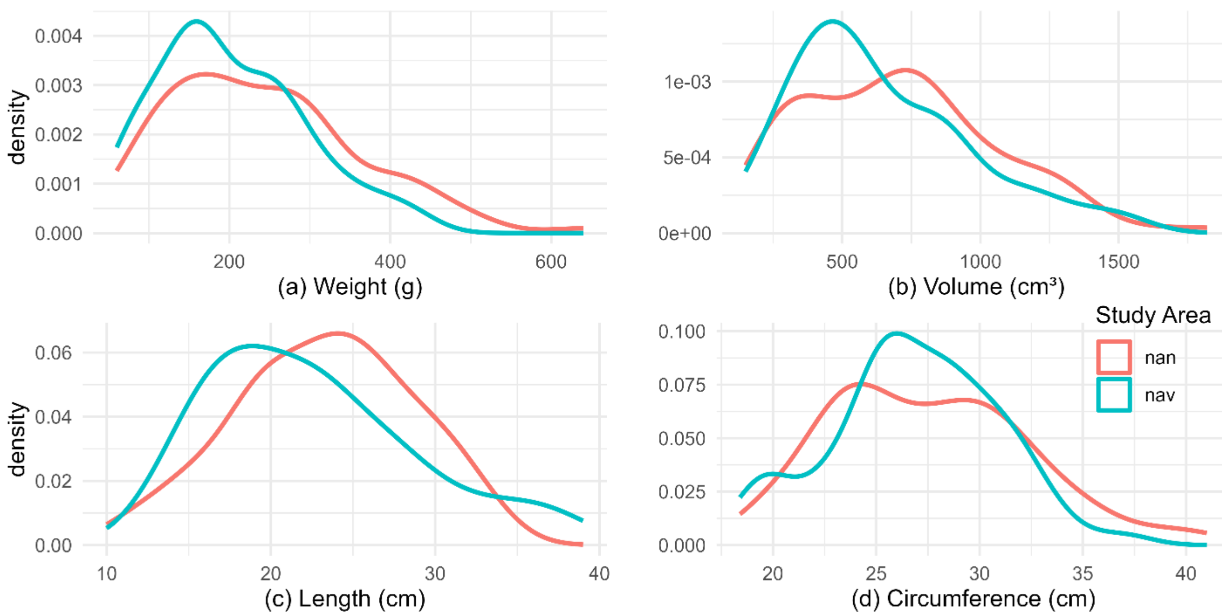

Figure 4.7: Distribution of Morphological Characteristics in Samples Collected from the Nandom (nan) and Navrongo (nav) study areas.

The summary statistics of the measurements and densities from the study areas are presented in Table 4.2. The means of samples from the Nandom Municipality and their standard deviations were mostly greater than those from Navrongo. Although the Nandom group exhibited greater mean length, it showed less variation in measurements compared to the Navrongo group.

Table 4.2: Summary of the Means and Standard Deviations of the Measurements and Densities from the Study Areas

Study Area	Variable	Weight	Volume	Length	Circumference	Density
		(g)	(cm^3)	(cm)	(cm)	(g/cm^3)
Nandom	Mean	241.6	707.2	23.240	27.543	2.933
	Std. dev	116.9	349.9	5.444	4.839	0.507
Navrongo	Mean	202.2	643.8	22.555	26.843	3.181
	Sd	91.4	320.5	6.361	4.016	0.480

The Weight of the fruit samples from Nandom (241 ± 116.9 g) exhibited greater variability than those from Navrongo (202.2 ± 91.4 g), but all values observed in Navrongo were within the range observed in Nandom. Similar wide ranges were observed for Mali (232.0 ± 215.0 g) and Malawi (201.0 ± 152.0 g) in western and southeastern Africa (Sanchez *et al*., 2011). The average fruit weight in this study was slightly greater than that in Mali and Malawi, but the range covered the intervals documented in earlier studies (Gurashi and Kordofani, 2014; Munthali *et al*., 2012).

Fruit circumference and density from both study areas were normally distributed, and length measurements from Nandom were also normally distributed. The mean circumference ($p = 0.314$) was not significantly different between the study areas, but the mean density ($p = 0.002$) was different.

Weight, volume, and length in the Navrongo group were not normally distributed. The medians of weight, volume, and length from Nandom were 230.0 g, 710.0 cm^3, and 23.60 cm, respectively. Their interquartile range (IQR) values were also 0.16, 0.49, and 8.00, respectively. In Navrongo, the corresponding values were 170.0 g, 580.0 cm^3, and 22.00 cm, with IQRs of 0.12, 0.42, and 10.00, respectively, were recorded. The differences between the medians of volume ($p = 0.265$) and length ($p = 0.178$) were not statistically significant. However, the between-weight ($p = 0.037$)

differences were significant. The differences observed can be attributed to factors influenced by the climate gradient.

Generally, Fruit size or volume is often represented by the maximum diameter or fruit length (Sanchez, 2011). On the African continent, the ranges of fruit length and width are 7.5–54 cm and 7.5–20 cm, respectively (Gurashi and Kordofani, 2014). Since this variability in length and width is consistent with the variability observed in this study, it indicates a basis for the wide application of the suggested computer vision method.

4.3.1.2 Fruit Detection and Image Feature Extraction

The training process went through 3000 iterations with loss box regression, loss classification, and loss mask values of 0.061, 0.015, and 0.052, respectively. The losses (box regression, classification, and mask) decreased as the model progressively learned and improved its performance on the detection and segmentation tasks. The mask accuracy was 97.77 %, which also indicated that the model was proficient at accurately segmenting the pixels of the *Adansonia digitata* fruit.

The two-dimensional (2D) image characteristics extracted from the segmented fruit regions exhibited substantial diversity. The pixel count difference for the equivalent diameter (Eq. Diameter) was approximately 30 pixels compared with approximately 394232 for the bounding box area (Bb. Area). Parameters such as the major diameter displayed a more concentrated distribution, whereas the others exhibited greater diversity, highlighting heterogeneity within the dataset (Table 4.3)

Table 4.3: Summary Statistics of the Extracted Image Characteristics for Mass Determination.

Statistic	Area (pixels)	Eq. Diameter (pixels)	Mj. Diameter (pixels)	Bb. Area (pixels)
Min.	47853.00	45.04	353.70	63099.00
1st Qu.	85491.50	54.66	539.37	124088.75
Median	119453.00	61.10	637.89	177727.00
Mean	120299.22	60.39	641.62	181674.66
3rd Qu.	149223.75	65.81	749.59	226137.50
Max.	229970.00	76.01	1039.91	457331.00

4.3.2 Quantification of Volume from Extracted Image Features

Overall, the best and most stable model during training was the random forest model, with an RMSE of 15.80, R^2 of 99.8 %, and MAE of 8.47. The accuracy metrics of svmLinear were the worst. The other models displayed moderate values during training. A similar pattern was observed during testing, where Random Forest was the best-performing model and svmLinear was the worst. In the testing dataset, the svmRadial and svmPoly flipped performance positions were compared to their training positions. Generally, there was a small decrease in performance from training to testing (Table 4.4)

Table 4.4: Comparative Performance of ML Volume Models on Training and Testing Data – Unveiling Insights into RMSE, R-squared, and MAE Metrics

Model	TRAINING				TESTING		
	RMSE	R-squared	MAE		RMSE	R-squared	MAE
Random Forest	15.796	0.998	8.465		50.819	0.980	22.988
svmRadial	56.396	0.973	37.894		70.961	0.961	46.967
svmPoly	59.657	0.970	41.152		69.157	0.962	43.366
svmLinear	65.770	0.964	45.311		72.456	0.958	47.666

In the validation dataset, the svmPoly model was best and closely matched by svmLinear in terms of the R^2 value. In addition, the SVM linear model yielded the best RMSE and MAE values. On the other hand, the RF model displayed a balanced combination of RMSE, R^2, and MAE values. The SVM radial model showed the worst performance in terms of all the metrics (Table 4.5).

Table 4.5: Comparative Performance of ML Volume Models on Single Fruit Image Features from Navrongo Data – Unveiling Insights into RMSE, R-squared, and MAE Metrics.

Model	RMSE	R-squared	MAE
svmPoly	95.24137	0.9716203	86.10354
svmLinear	60.18458	0.9657215	41.32424
Random Forest	108.80602	0.9103636	78.20715
svmRadial	251.34992	0.7367830	211.48176

A plot of the estimated volumes of single fruits against those observed by the water displacement method from the validation dataset summarizes the performance of the models. The plotted points were closely aligned to the 1:1 line, indicating accuracy in estimation except for svmRadial, which deviated, and svmPoly, which appeared to consistently underestimate the fruit volume (Figure 4.8).

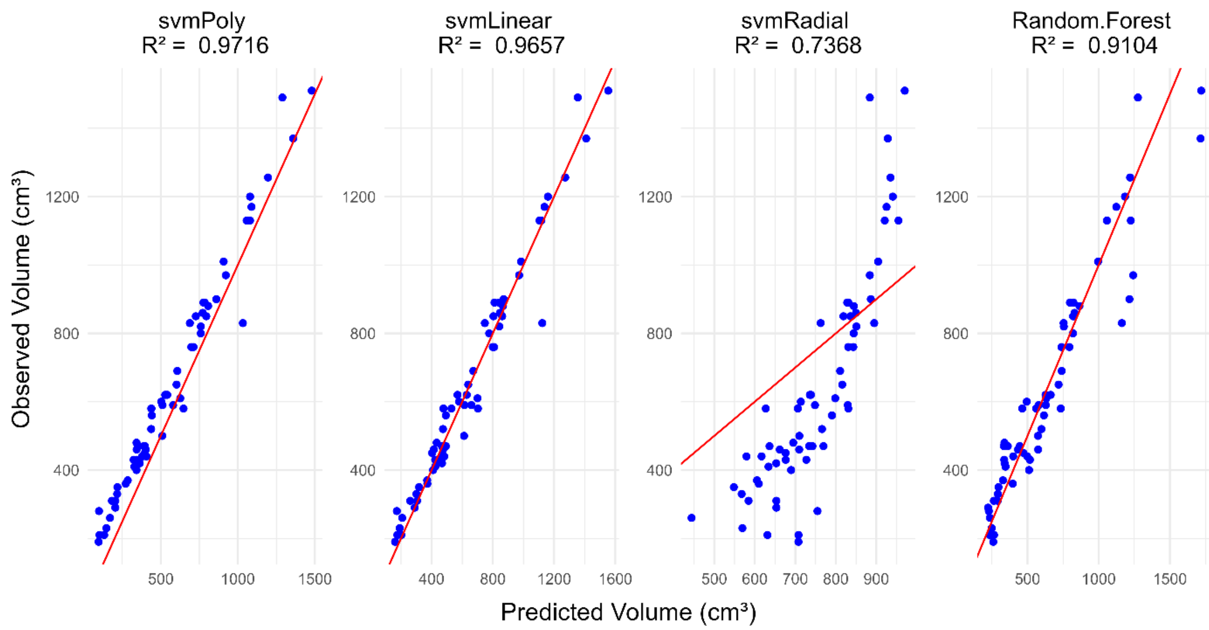

Figure 4.8: Plot of the Observed (WDM) Volume from Navrongo and the Predicted Volume from Machine Learning Models.

The 1:1 Line Indicates Perfect Predicted = Observed. The Model R^2 shows Agreement Between Observed and Predicted Values.

In the study by Omid *et al.* (2010), computer vision techniques were used to estimate fruit volume, achieving R^2 values of 0.962 for lemons, 0.970 for limes, 0.985 for oranges, and 0.959 for tangerines, indicating high accuracy. In contrast, the random forest model in this study attained an R^2 of 99.8 % on the training dataset, demonstrating superior predictive performance. This suggests that the random forest method effectively captures complex, non-linear relationships.

Fitriyah (2022) observed that single-view images have limitations when estimating the volume of fruits with non-axis-symmetric shapes. However, this study demonstrates that high prediction accuracy can be achieved using only single-view 2D images, even for irregularly shaped fruits. This finding broadens the application of image-based volume estimation. Nyalala *et al.* (2019) reported that combining 2D and 3D image features improves the prediction of fruit volume, but

2D models still offer significant practical advantages. They include simpler data acquisition, faster processing times, and lower computational costs, which make them more feasible for large-scale deployment in low-resource environments. This study challenges previous assumptions about the limitations of 2D imagery for complex fruit shapes and highlights the potential of cost-efficient machine learning approaches, such as the random forest model, in achieving high accuracy without relying on complex 3D imaging systems.

In this study, the volumes predicted by the SVM radial model consistently either underestimated or overestimated the volume, depending on the fruit size. Relying on them for decision-making could result in financial losses, pricing errors, and inefficiencies in resource allocation and supply chain operations.

4.3.2.1 Statistical Analysis

The mean difference between volume approximations from each of the svmPoly, svmLinear, and random forest models and the water displacement method (WDM) was not statistically significant ($P \geq 0.05$), except for svmRadial ($P = 0.01$).

The Bland–Altman plots in Figure 4.9 show that the differences in volumes estimated by the model and those estimated by the WDM were normally distributed.

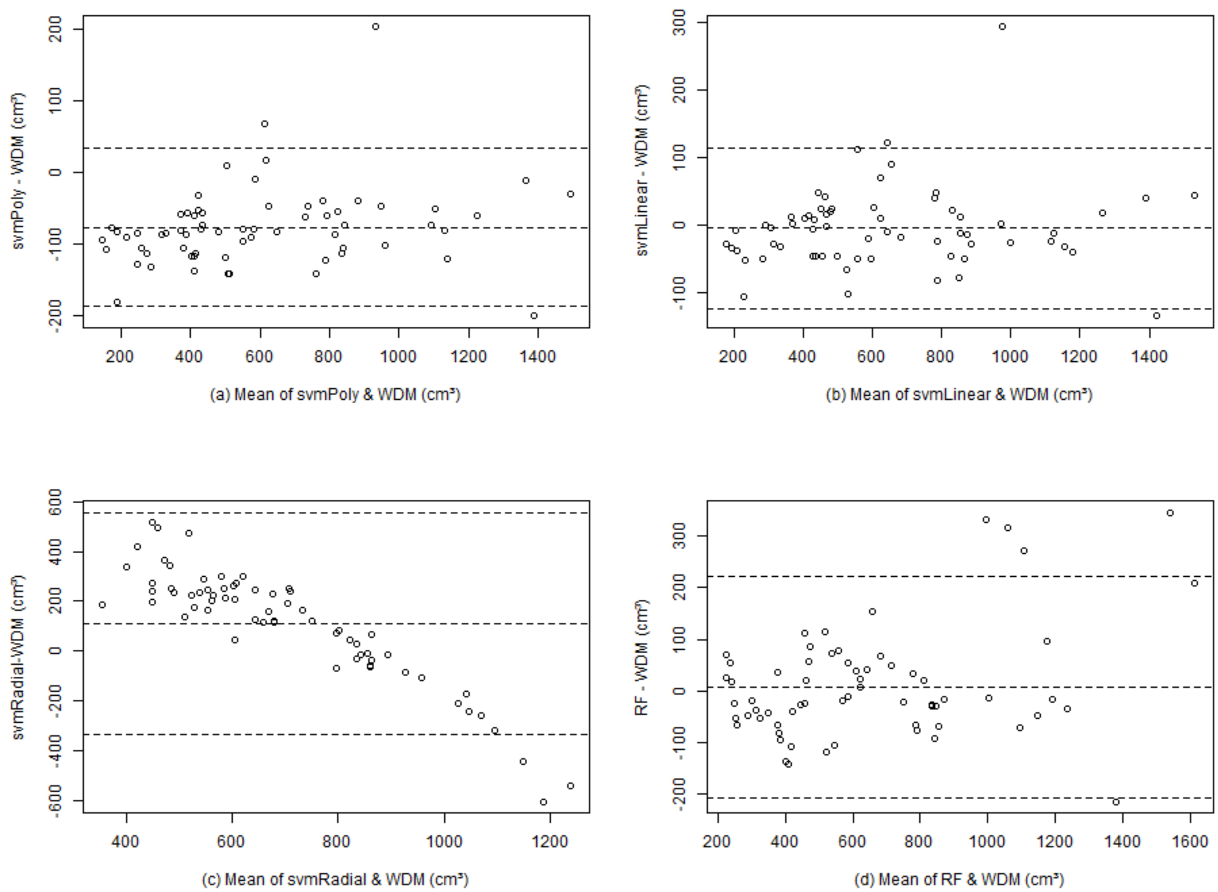

Figure 4.9: Bland–Altman Plot for the Comparison of Volumes Estimated by Machine Learning Models and the Water Displacement Method (WDM).

The Outer Lines indicate the 95 % Limits of Agreement, and the Centerline shows the Average Difference.

The 95 % of the volume differences are expected to lie between the dotted lines (95 % limits of agreement). The volume differences between the model quantifications and WDM can be seen in Figure 4.9 (parts a, b, c, and d). The differences were normally distributed for svmLinear (Figure 4.9: part a), svmPoly (Figure 4.9: part b), and random forest (Figure 4.9: part d).

Figure 4.9 (part c) shows that for small *Adansonia digitata* fruits, the volume estimated by the SVM radial method was greater than that estimated by the WDM, and vice versa. Thus, the model overestimates the volume of small fruits and understates large fruits. This may be because the relationship between the extracted image features and the volume is nonlinear.

4.3.2.2 Important Image Features for Volume Determination

The area of the segmented fruit region and the equivalent diameter were the dominant variables, contributing nearly 100 % of the variance explained by the SVM models. All other features contributed less than 80 %. The major diameter contributed 68.25 %. Positional features were mostly inconsequential or of very small importance.

In the random forest model, the major diameter was the most important variable, contributing nearly 100 % of the variance explained. The area of the segmented fruit region and the equivalent diameter were not very useful variables, as they had less than 40 % explanatory power. Compared with positional features, 2D geometric features are useful estimators of Adansonia digitata fruit volume. The major diameter is the most useful for the random forest and variants of the support vector machines. The area of the segmented region and equivalent diameter are better alternatives to the major diameter when considering support vector machine models alone.Previous studies have focused on using 2-dimensional image features such as the projection area, perimeter, eccentricity, major-axis length, minor-axis length, radial distance, horizontal length of the bounding box, and vertical length of the bounding box to estimate volume via regression (Fitriyah, 2022; Nyalala *et al*., 2019). Despite the successes achieved, emphasis has mostly been placed on axis-symmetric fruits. The equivalent diameter introduced in this study and shown to be relevant in regression by support vector machines provides an interesting basis for further study of the volume of axis-nonsymmetric fruits (Nyalala *et al*., 2019).

4.3.3 Single Variable Mass Regression Modeling

Figure 4.10 (part a) shows a scatter plot of the observed mass against volume.

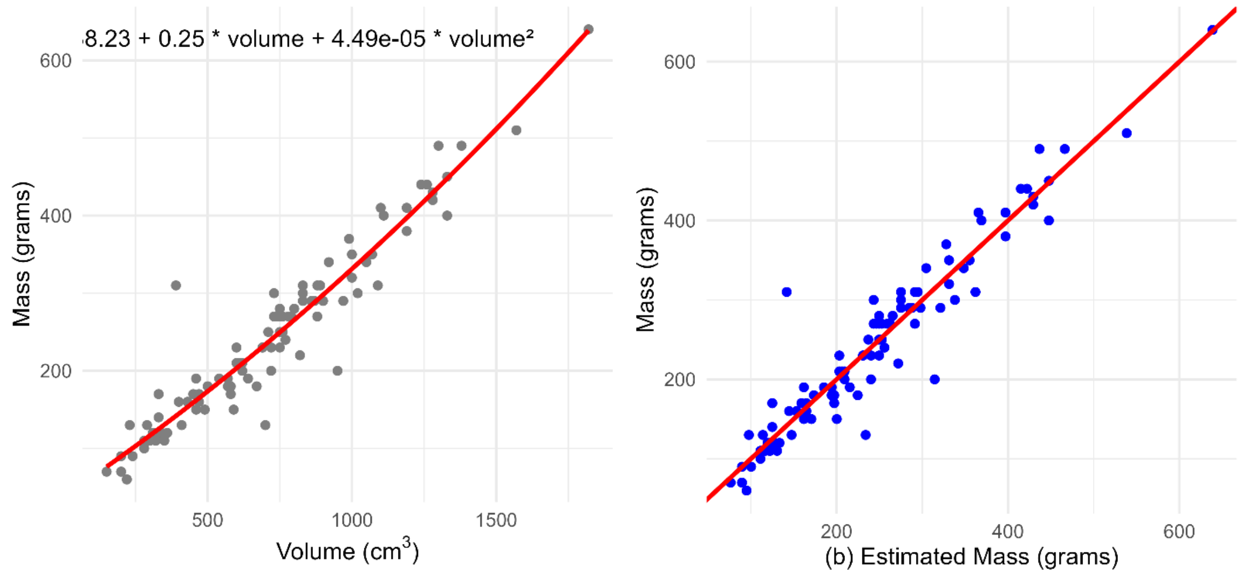

Figure 4.10: Regression of Observed Mass to Volume, Mass = 38.23 + 0.25 * Volume + 4.49e-05 * Volume^2, R^2 = 92 %, and (Part b) Scatter Plot of Observed Mass to Estimated Mass around the 1:1 Line (Part b)

A quadratic relationship was observed between mass (g) and volume (cm^3), with an intercept of 38.23, a slope of 0.25, a coefficient of the quadratic term of 4.49×10^{-5}, and an adjusted R^2 of 92 %. The predicted mass was further regressed against the observed mass, Figure 4.10 (part b). The values were randomly clustered along the 1:1 line with gradient 1 and intercept 0.

In certain production, marketing, or research settings, where mass may be a preferred measurement, measured volumes and estimates obtained from machine learning models can be converted to corresponding mass values, using the univariate relationship between mass and volume.

4.3.4 Modeling Probability Density Functions

The prior probability density functions (PDFs) of the sampling distribution of 1 million bootstrapped means of mass and volume were gamma-distributed, but the density was log-normally distributed. The distributions of the standard deviations were gamma, normal, and log-normal for mass, volume, and density, respectively (Table 4.6).

Table 4.6: Prior Distribution of Parameters used in the Stan

Data	Parameter	PDF	Approximation
Mass	Mean	Gamma (717.75, 3.17)	Normal (266.15, 8.44)
	Sd	Gamma (268.10, 2.47)	-
Volume	Mean	Gamma (676.25, 990.98)	Normal (682.40, 26.24)
	Sd	Normal (337.66, 18.61)	-
Density	Mean	Lognormal (-1.08, 0.01)	Normal (0.340, 0.005)
	Sd	Lognormal (-2.79, 0.16)	-

The Rhat ($\breve{R}$) values computed for all the models were unity, indicating convergence of the Monte Carlo Markov chain sampling process. The autocorrelation decreased with increasing lag to values close to zero at a lag of approximately five for the samples. In addition, there was a strong central tendency with randomly distributed aberrations that did not depict any trend or distinctions between individual chains.

In Figure 4.11, the posterior distributions are shown in blue, and the industry distribution is shown in red. The plot shows that the majority of fruits collected from Nandom were collected from a population with an average mass of 218.87 ± 7.00 g and a standard deviation of 8.04 ± 0.42 g. The posterior distribution of volume followed a distribution similar to that of the population. It had a mean value of 671.39 ± 22.03 cm^3 and a standard deviation of 25.84 ± 1.25 cm^3. On the other hand, the distribution of density further decreased compared with that observed for mass and density. It had a mean value of 0.33 ± 0.00 g/cm^3 and a standard deviation of 0.004 ± 0.00 g/cm^3 (Figure 4.11).

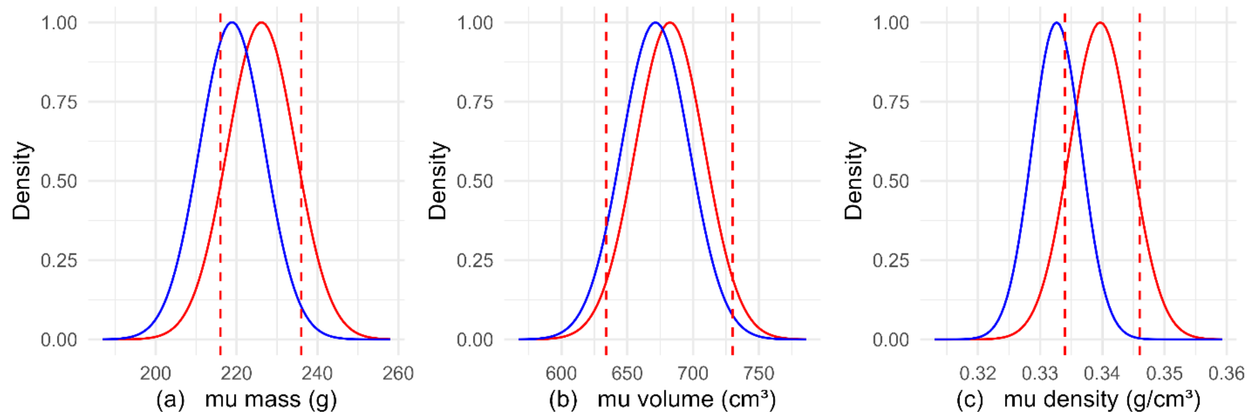

Figure 4.11: Comparison of Prior (red) and Posterior (blue) Population Distributions of Samples Obtained from Nandom

The probability below the lower threshold was the highest in the density distribution and the lowest in the volume distribution. The situation reverses between the thresholds. Beyond the upper threshold, the probabilities decreased from mass to volume to density (Table 4.7).

Table 4.7: Cumulative Probability Below, Between, and Above the Threshold for Mass, Volume, and Density Posterior Distributions

Probability	**Mass (g)**	**Volume (cm^3)**	**Density (g/cm^3)**
Below min threshold	0.39 ± 0.26	0.13 ± 0.16	0.60 ± 0.28
Between max-min threshold	0.55 ± 0.21	0.82 ± 0.15	0.39 ± 0.26
Above max threshold	0.05 ± 0.09	0.04 ± 0.08	0.01 ± 0.03

Fruit size distribution is important for sorting and grading fruits. In the *Adansonia digitata* fruit industry, fruit size is linked to sweetness, consumer preferences, and market value (Gurashi and Kordofani, 2014; Odoom, 2021). The weight and proportion of pulp are also taken into account when grading *Adansonia digitata* fruits (Omondi *et al.*, 2019). According to a study by Venter and Witkowski (2011), larger fruits contain more seeds and pulp, and sorting by size can lead to more accurate predictions. In their study, they categorized mature *Adansonia digitata* fruits into small, medium, and large sizes using fruit length and diameter as indicators. However, the approach could be complex if applied to classify many fruits due to multiple indicators. Instead, this study simplified the process by using mass, volume, and density distributions. Analyzing the area under the probability density function (PDF) within set thresholds allows for easier and more consistent classification to facilitate storage and transportation planning. It can also help sellers to standardize prices to enhance trade transparency.

4.4 Conclusion and Recommendations

This study has shown that computer vision and machine learning techniques are applicable for morphological characterization of *Adansonia digitata* fruits. It developed a computer vision framework for detecting and segmenting *Adansonia digitata* fruits for uncontrolled background and lighting conditions. The framework extracts morphological characteristics from 2D images of *Adansonia digitata* fruits to estimate their volume and mass by statistical regression and machine learning. It further undertakes probabilistic classification of the point estimate into different size categories by Bayesian extension. The approach overcomes challenges associated with estimating volumes of non-axis-symmetric fruits under field conditions and addresses inefficiencies of traditional methods.

The framework achieved a segmentation mask accuracy of 97.8 %. The 2D features that were extracted from the image for regression included the segmented area, major diameter, and equivalent diameter. The major diameter was the best estimator of fruit volume in the random forest model. The random forest model outperformed the variants of support vector machines (R^2 of 99.8 %, RMSE of 15.8 cm^3) for volume prediction. A quadratic relationship (R^2 = 92%) was also found between volume and mass, allowing for reliable mass estimation based on volume and conversion during post-harvest operations.

Adansonia digitata fruits from Nandom were larger and heavier (241.6 g) than those from Navrongo(202.2 g). Meanwhile, fruits from Navrongo had a higher density (3.2 g/cm^3) compared to those from Nandom (2.9 g/cm^3). This indicates that environmental factors affect fruit morphology and emphasizes the need to consider the effect of ecological variability in research and commercial applications.

The transformation of point estimates of mass volume and density to their posterior distributions through integration of Bayesian statistics enhanced the analytical framework. The distributions enabled probabilistic classification of fruits into size categories (small, medium, large) and provided credible intervals to account for uncertainty. This approach is valuable for production planning, sorting, grading, and inventory management, as it directly affects operational efficiency and market competitiveness.

Overall, the study demonstrates the potential of computer vision and Bayesian modeling to transform the process of determining the morphological characteristics of fruit trees. The framework developed offers a scalable, non-invasive, and cost-effective solution for fruit mass, volume, and density quantification and sorting, with practical applications for *Adansonia digitata* powder and seed oil production in a commercial setting. Future research should focus on enhancing model generalizability by including data from sites across diverse climate zones to account for the effect of environmental factors. Perspective correction should be incorporated to reduce distortion due to the camera lens. The method can be used to develop field-deployable tools for decision support.

This work provides a foundation for the wider application of computer vision and Bayesian modeling in managing production and logistics in the *Adansonia digitata* value chain.

References

Assogbadjo, A. E., Sinsin, B., Codjia, J. T. C., & Van Damme, P. (2006). Ecological diversity and pulp, seed and kernel production of the baobab (*Adansonia digitata*) in Benin. *Belgian Journal of Botany, 139*(1), 47–56.

Bland, J. M., & Altman, D. G. (1999). Measuring agreement in method comparison studies. *Statistical Methods in Medical Research*, *8*(2), 135–160. https://doi.org/10.1177/096228029900800204

Egbadzor, K. F. (2020). Studies on baobab diversity, seed germination, and early growth. *South African Journal of Botany*, *133*, 178–183. https://doi.org/10.1016/j.sajb.2020.07.024

Fitriyah, H. (2022). Accuracy of various methods to estimate volume and weight of symmetrical and non-symmetrical fruits using computer vision. *Journal of ICT Research and Applications*, *16*(3), 210–225. https://doi.org/10.5614/itbj.ict.res.appl.2022.16.3.2

Gouwakinnou, G. N., Assogbadjo, A. E., Lykke, A. M., & Sinsin, B. (2011). Phenotypic variations in fruits and selection potential in *Sclerocarya birrea* subsp. birrea. *Scientia Horticulturae*, *129*(4), 777–783. https://doi.org/10.1016/j.scienta.2011.05.041

Gray, D. O., & Hayman, A. R. (1986). *Adansonia digitata* - African Baobab. In *Phytochemistry* (Vol. 26, Issue 3, pp. 839–841).

Gurashi, N. A., & Kordofani, M. A. (2014). Morphological variation in fruit shapes of *Adansonia digitata* L. from Blue Nile and North Kordofan States, Sudan. *Journal of Forest Products & Industries*, *3*(2), 106–111.

Hoffman, M. D., & Gelman, A. (2014). The no-U-turn sampler: Adaptively setting path lengths in Hamiltonian Monte Carlo. *Journal of Machine Learning Research*, *15*(2008), 1593–1623.

Hyde, R., Hartley, S., & Millar, K. (2017). European novel foods policy at a critical juncture: Drawing lessons for future Novel Food Governance through a retrospective examination of Regulation 258/97. *Food and Drug Law Journal*, *72*(3), 472–505.

Ifmalinda, Putri, R. E., & Rasinta, I. (2022). Estimation of size, volume and weight of oranges using digital images processing. *IOP Conference Series: Earth and Environmental Science*, *1059*(1). https://doi.org/10.1088/1755-1315/1059/1/012016

Kheiralipour, K., & Kazemi, A. (2020). A new method to determine morphological properties of fruits and vegetables by image processing technique and nonlinear multivariate modeling. *International Journal of Food Properties*, *23*(1), 368–374. https://doi.org/10.1080/10942912.2020.1729177

Khojastehnazhand, M., Omid, M., & Tabatabaeefar, A. (2010). Determination of tangerine volume using image processing methods. *International Journal of Food Properties*, *13*(4), 760–770. https://doi.org/10.1080/10942910902894062

Koc, A. B. (2007). Determination of watermelon volume using ellipsoid approximation and image processing. *Postharvest Biology and Technology*, *45*(3), 366–371. https://doi.org/10.1016/j.postharvbio.2007.03.010

Mansuri, S. M., Gautam, P. V., Jain, D., Nickhil, C., & Pramendra. (2022). Computer vision model for estimating the mass and volume of freshly harvested Thai apple ber (*Ziziphus mauritiana* L.) and its variation with storage days. *Scientia Horticulturae*, *305*, 111436. https://doi.org/10.1016/j.scienta.2022.111436

Marcelis, L. F. M., Heuvelink, E., & Goudriaan, J. (1998). Modelling biomass production and yield of horticultural crops: A review. *Scientia Horticulturae, 74*(1–2), 83–111. *https://doi.org/10.1016/S0304-4238(98)00083-1*

Ministry of Food and Agriculture (MOFA), Ghana. (2022). Savannah agriculture value chain development project (SADP)-Nandom Municipality: Environmental and social impact assessment (ESIA). *SAL Consult Limited, P. O. Box GP20200, Accra, Ghana*, *June*.

Miyoshi, G. T., Imai, N. N., Tommaselli, A. M. G., de Moraes, M. V. A., & Honkavaara, E. (2020). Evaluation of hyperspectral multitemporal information to improve tree species identification in the highly diverse Atlantic forest. *Remote Sensing*, *12*(2), 1–22. https://doi.org/10.3390/rs12020244

Mkwezalamba, I., Munthali, C. R. Y., & Missanjo, E. (2015). Phenotypic variation in fruit morphology among provenances of *Sclerocarya birrea* (A. Rich.) Hochst. *International Journal of Forestry Research*, *2015*, 1–8. https://doi.org/10.1155/2015/735418

Munthali, C. R. Y., Chirwa, P. W., & Akinnifesi, F. K. (2012). Phenotypic variation in fruit and seed morphology of *Adansonia digitata* L. (Baobab) in five selected wild populations in Malawi. *Agroforestry Systems*, *85*(2), 279–290. https://doi.org/10.1007/s10457-012-9500-1

Nyalala, I., Okinda, C., Chao, Q., Mecha, P., Korohou, T., Yi, Z., Nyalala, S., Jiayu, Z., Chao, L., & Kunjie, C. (2021). Weight and volume estimation of single and occluded tomatoes using machine vision. *International Journal of Food Properties*, *24*(1), 818–832. https://doi.org/10.1080/10942912.2021.1933024

Nyalala, I., Okinda, C., Nyalala, L., Makange, N., Chao, Q., Chao, L., Yousaf, K., & Chen, K. (2019). Tomato volume and mass estimation using computer vision and machine learning algorithms: Cherry tomato model. *Journal of Food Engineering*, *263*, 288–298. https://doi.org/10.1016/j.jfoodeng.2019.07.012

Odoom, D. A. (2021). Characterization of Baobab (*Adansonia digitata* L.) in the Builsa District of Ghana. *Journal of Food Technology and Preservation*, *2*(1). https://doi.org/10.36266/JFTP/116

Omondi, M., Rimberia, F. K., Wainaina, C. M., Mukundi, J. B. N., Orina, J., Gebauer, J., & Kehlenbeck, K. (2019). Fruit morphological diversity and productivity of baobab (*Adansonia digitata* L.) in coastal and lower eastern Kenya. *Forests Trees and Livelihoods*, *28*(4), 266–280. https://doi.org/10.1080/14728028.2019.1659861

Parkouda, C., Sanou, H., Tougiani, A., Korbo, A., Nielsen, D. S., Tano-Debrah, K., Ræbild, A., Diawara, B., & Jensen, J. S. (2012). Variability of Baobab (*Adansonia digitata* L.) fruits' physical characteristics and nutrient content in the West African Sahel. *Agroforestry Systems*, *85*(3), 455–463. https://doi.org/10.1007/s10457-011-9406-3

Raja Sekar L, Ambika N, D. V. & K. T. (2018). Fruit classification system using computer vision: A review. *International Journal of Trend in Research and Development*, *5*(1), 2394–9333. www.ijtrd.com

Sanchez, A. C., De Smedt, S., Haq, N., & Samson, R. (2011). Comparative study on baobab fruit morphological variation between western and south-eastern Africa: Opportunities for domestication. *Genetic Resources and Crop Evolution*, *58*(8), 1143–1156. https://doi.org/10.1007/s10722-010-9647-4

Siswantoro, J., Prabuwono, A. S., & Abdulah, A. (2013). Volume Measurement of food product with irregular shape using computer vision and Monte Carlo method: A framework. *Procedia Technology*, *11*(Iceei), 764–770. https://doi.org/10.1016/j.protcy.2013.12.256

Stan Development Team. (2024). *{RStan}: the {R} interface to {Stan}*. https://mc-stan.org/

The Commission of the European Communities. (2008). Commission decision of 27 June 2008 authorising the placing on the market of Baobab dried fruit pulp as a novel food ingredient under Regulation (EC) No 258/97 of the European Parliament and of the Council. *Official Journal of the European Union*, *258*, 38–39.

Venter, S. M., & Witkowski, E. T. F. (2011). Baobab (*Adansonia digitata* L.) fruit production in communal and conservation land-use types in Southern Africa. *Forest Ecology and Management*, *261*(3), 630–639. https://doi.org/10.1016/j.foreco.2010.11.017

Welford, L., & Breton, G. Le. (2008). Bridging the gap: Phytotrade Africa's experience of the certification of natural products. *Forests Trees and Livelihoods*, *18*(1), 69–79. https://doi.org/10.1080/14728028.2008.9752618

Zheng, C., Liu, T., Abd-Elrahman, A., Whitaker, V. M., & Wilkinson, B. (2023). Object-Detection from Multi-View remote sensing Images: A case study of fruit and flower detection and counting on a central Florida strawberry farm. *International Journal of Applied Earth Observation and Geoinformation*, *123*, 103457. https://doi.org/10.1016/j.jag.2023.103457

CHAPTER FIVE

A WEB-BASED APPLICATION TO ESTIMATE PHYSICAL PROPERTIES OF *ADANSONIA DIGITATA* FRUITS FROM IMAGES

5.1 Introduction

In recent years, image-based analysis, coupled with machine learning and statistical modeling, has become a valuable tool for observing, describing, and estimating the physical properties of fruits (Dono *et al.*, 2024; Kheiralipour and Kazemi, 2020; Tran *et al.*, 2023). These models aim to facilitate efficient high-throughput assessments of fruits, informing ecological monitoring, production planning, and natural resource management. However, despite their potential, these innovations provide little practical value to end users unless the gap between research and real-world deployment is addressed through application development or by translating the outcome into accessible tools.

The process of translating the outcomes of computer vision, machine learning, and statistical modeling for practical use often requires expertise in one or more programming languages, posing a barrier for potential users who are non-experts. Another difficulty comes from the need for advanced computational resources such as high-performance computing environments, cloud infrastructure, and specialized hardware, which are costly, even though essential (Tyagi and Rekha, 2019). Again, adapting the system for resource-constrained devices such as mobile phones adds another layer of complexity (Sinha *et al.*, 2023). Therefore, expertise, technical difficulty, high costs, and specialized infrastructure restrict widespread adoption, especially in resource-constrained environments.

In contrast, an interactive web-based application offers easy access for users to interact with code, data, and visualizations through a web browser, which can help to disseminate research findings (Saia *et al.*, 2022). Again, it is suitable for increasing exposure to computer vision research and innovation because it eliminates the need for software installation, integrates with cloud computing for high-performance processing, is cost-effective, and can run on multiple devices and browsers (Sturm *et al.*, 2017). Their user-friendly interfaces simplify advanced technologies such as machine learning and computer vision, making these tools accessible to non-experts.

This study builds upon the methodology proposed by Dono *et al.* (2024) to develop an interactive web application using the R (R Core Team, 2024) code and the Shiny (Chang *et al.*, 2024) framework. It provides users with a user-friendly interface to enable them to upload images of *Adansonia digitata* fruits, in order to perform instance segmentation, extract morphological features, and estimate physical properties (volume, mass, and density) for statistical inference regarding their population. The morphological features may be exported for further downstream modeling.

5.2 Material and Methods

5.2.1 R Shiny

R Shiny is an R package from RStudio (Posit). It allows users to create interactive web applications even when they do not have knowledge of HTML, CSS, or JavaScript (Chang *et al.*, 2024). It uses a reactive programming model to automatically update other fields when input fields are changed, to improve the user experience. A Shiny app includes a user interface (UI) for layout and controls, and a server function for processing inputs (SSCC, 2024). It can generate various outputs like tables and plots, and is deployed on platforms like shinyapps.io. It is often used for developing interactive data applications in fields like healthcare, finance, engineering, forestry, and ecological science (Fay *et al.*, 2021; Longstaff, 2017; Regenstein, 2018; Silva *et al.*, 2022).

5.2.2 The Web Application

The web-based application was developed by following the computer vision, machine learning, and statistical methods outlined in Dono *et al.* (2024). The Application integrates R, Python, and the RShiny package. It utilized a pretrained, Python-based Mask R-CNN for instance segmentation and feature extraction, R-based machine learning models for estimating physical properties, and Bayesian statistics for assessing the population distribution of *Adansonia digitata* fruits.

The Mask R-CNN model was developed in Detectron2 and loaded via Reticulate for segmentation and feature extraction of the *Adansonia digitata* fruits. The model was trained to segment every instance of *Adansonia digitata* fruit in the image, assign a unique identifier, and extract morphological features such as centroid coordinates, area, bounding box dimensions, and diameters.

Physical properties (volume, mass, and density) are estimated from the extracted features using a pretrained random forest model. The model was trained on a dataset of features obtained from *Adansonia digitata* fruit images whose volume, mass, and density were measured. Bayesian inference is conducted with RStan to estimate the population distribution of physical properties. The model assumes that mean values of mass, volume, and density are normally distributed, and their standard deviations are log-normally distributed. It produces point estimates, credible intervals, and convergence diagnostics, such as Rhat and effective sample size (n_eff).

5.3 Installation

5.3.1 Software Environment Setup

In order to install and run the R Shiny application, first set up the required software environment, including R, RStudio, and relevant dependencies for both R and Python. Download and install **R 4.3.1** or **later** for Windows from the Comprehensive R Archive Network (*CRAN*). Run the installer and follow the on-screen instructions. When the installation of R is complete, download and install RStudio (*RStudio Download*) for Windows by following the setup instructions.

Once R and RStudio are installed, open RStudio and install the necessary R packages, shiny, reticulate, rstan, ggplot2, and caret (Allaire *et al.*, 2025; Chang *et al.*, 2024; Kuhn, 2024; S. D. Team, 2025; Wickham *et al.*, 2024) by running the following commands in the R console:

```
install.packages("shiny")

install.packages("reticulate")

install.packages("rstan")

install.packages("ggplot2")

install.packages("caret")
```

The packages enable the Shiny framework, Python integration, Bayesian modeling, data visualization, and machine learning functionalities.

5.3.2 Python and Dependencies

The application uses Detectron-2, which requires Python-based dependencies. If Python is not installed, download Python 3.8 or later from *python.org/downloads* and install. Make sure the "Add Python to PATH" box is checked during installation. Subsequently, install the required Python packages, pip, antlr4-python3-runtime, yacs, portalocker, pathspec, omegaconf, mypy-extensions, iopath, hydra-core, black, fvcore, torch, torchvision, torchaudio, opencv-python, numpy, pycocotools, and cloudpickle (Burns, 2023; Developer team mypy, 2023; Developer team pycocotools, 2024; FAIR, 2022b, 2022a; Girshick, 2020; Łukasz Langa, 2025; Oliphant and Al., 2025; OpenCV Team, 2025; Rick van Hattem, 2024; Soumith Chintala David Pollack, 2025; P. C. Team, 2025; T. cloudpickle developer Team, 2025; Terence Parr, 2024; The pip Developers, 2025; Wang *et al.*, 2016; Yadan, 2022, 2023) using the reticulate package in R:

```
library(reticulate)
install_python_packages <- function() {
 packages <- c("pip", "antlr4-python3-runtime", "yacs", "portalocker", "pathspec",
      "omegaconf", "mypy-extensions", "iopath", "hydra-core",
      "black", "fvcore", "torch", "torchvision", "torchaudio",
      "opencv-python", "numpy", "pycocotools", "cloudpickle")

 for (pkg in packages) {
  py_install(pkg)
 }
```

```
}
install_python_packages()
```

Before this task, ensure that Python is accessible via **reticulate,** otherwise, install it through the R console (Appendix 5).

5.3.3 Download and Run the Application.

Download the application files from the link *here* and extract the zipped file's contents, ensuring the original folder and file structure are maintained. Copy the extracted folder to the desired location on your computer. Navigate to the "BaoSOFT" folder within the extracted contents and verify that it contains the R Shiny application script (app.R). Open RStudio and load the shiny library:

```
library(shiny)
```

Launch the app by executing:

```
runApp("path/to/BaoSOFT")
```

Replace "path/to/BaoSOFT" with the path to the folder on your computer.

5.3.4 Results and Discussion

The application offers an intuitive interface with command buttons, a combo box, and check boxes to enhance workflow, as illustrated in Figure 5.1.

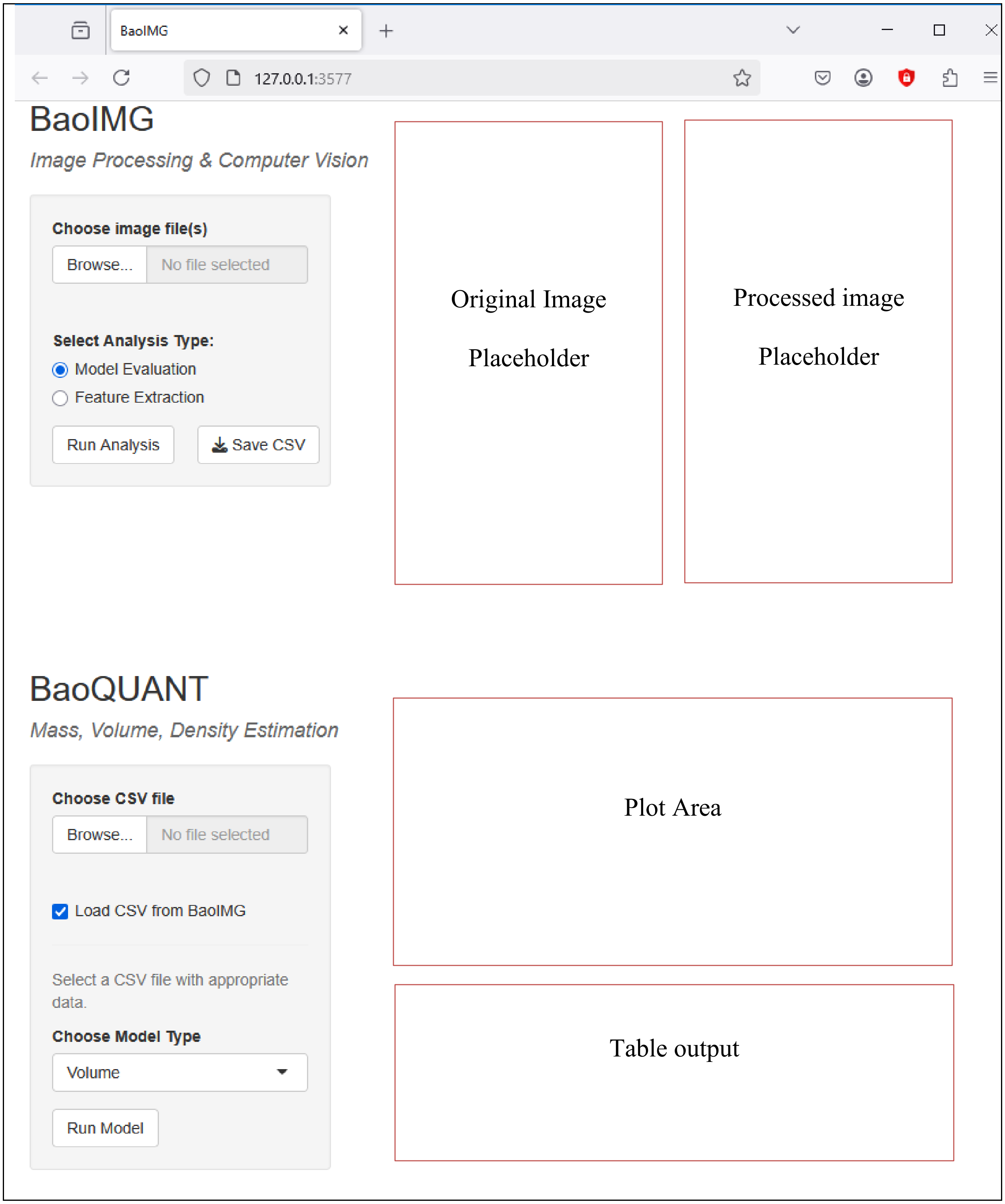

Figure 5.1: Web Application Interface for BaoIMG (Image Processing and Segmentation) and BoaQUANT (Mass, Volume, Density Estimation)

The workflow for estimating the physical properties of *Adansonia digitata* fruits was implemented in two stages: BaoIMG and BaoQUANT, respectively. The first stage manages image processing and computer vision tasks that result in the extraction of fruit morphological features, while the second stage utilizes a pretrained random forest model to assess their physical characteristics and Bayesian statistics for distribution properties.

5.3.4.1 BaoIMG

To use BaoIMG, launch the application and click the "Browse" button. Navigate to the folder containing the image you want to upload and select it. Once the image is uploaded, a blue indicator will appear below the "Browse" button to confirm that the upload was successful.

To view the original image alongside the processed output, which displays the segmented fruits with bounding boxes and annotations, select "Model Evaluation" under the Analysis Type and click "Run Analysis." (Figure 5.2).

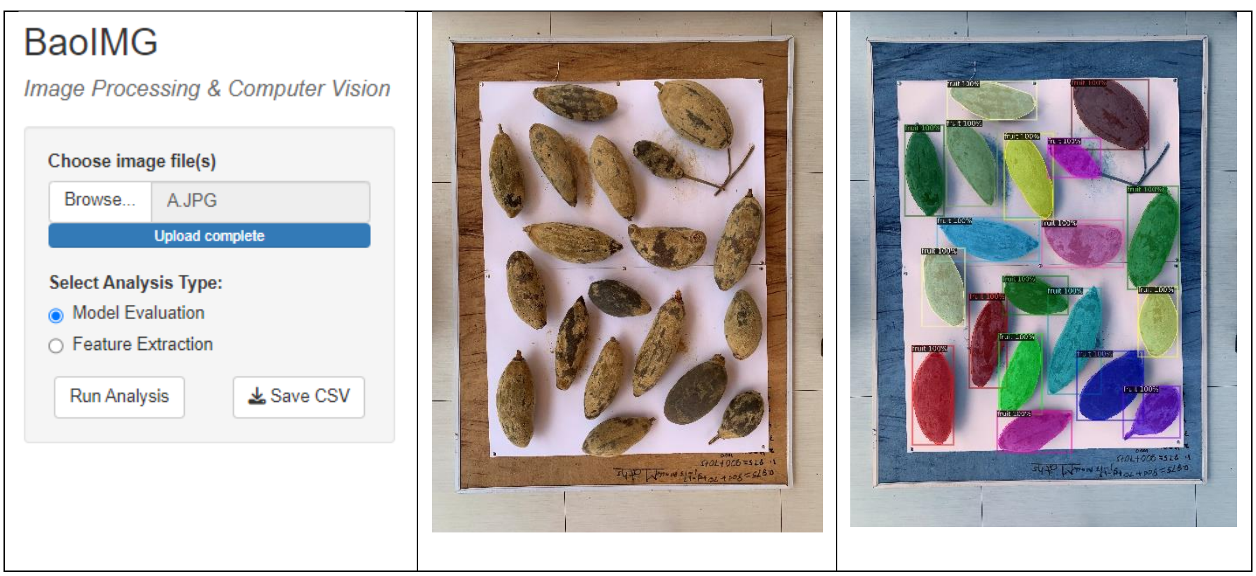

Figure 5.2: BaoIMG Displaying Original and Processed Image (left-right) with Segmentation and Bounding Boxes

If you need to perform further analysis within BoaQuant or plan to conduct downstream analysis outside the application, choose "Feature Extraction" as the Analysis Type and click "Run Analysis." To save the extracted features for external use, simply click "Save CSV." A sample of the CSV file is shown in Figure 5.3

File Name	Class Name	Object Number	Area	Centroid	Solidity	BoundingBox	Equiv_Diameter	Major_Diameter1	Major_Diameter2
A.JPG	fruit	1	125992	(0.0, 3280.3663804051052, 1427.625190488285)	inf	(0, 3126, 1155, 1, 3447, 1730)	62.19872027	651.8459757	651.8459757
A.JPG	fruit	2	146611	(1.0, 1261.0660387010525, 576.8819392815)	inf	(1, 893, 428, 2, 1598, 728)	65.42182343	764.9582369	764.9582369
A.JPG	fruit	3	181558	(2.0, 3015.1016920212824, 655.8594333491226)	inf	(2, 2616, 485, 3, 3386, 806)	70.25419404	826.9060459	826.9060459
A.JPG	fruit	4	196607	(3.0, 1783.2735253576932, 2368.1504219076637)	inf	(3, 1371, 2167, 4, 2173, 2567)	72.1439834	895.6839728	895.6839728
A.JPG	fruit	5	107204	(4.0, 3129.399817171001, 2393.7509234730046)	inf	(4, 2931, 2150, 5, 3334, 2580)	58.93918451	542.5334275	542.5334275
A.JPG	fruit	6	186452	(5.0, 2583.979844678523, 1759.2377233818893)	inf	(5, 2164, 1544, 6, 2990, 1959)	70.87985297	968.1593949	968.1593949
A.JPG	fruit	7	179173	(6.0, 2942.3487020923912, 2050.399864935007)	inf	(6, 2655, 1790, 7, 3196, 2291)	69.94521042	719.8857532	719.8857532
A.JPG	fruit	8	130927	(7.0, 2846.012426772171, 1333.4204938629923)	inf	(7, 2522, 1169, 8, 3150, 1489)	63.00043258	732.4377805	732.4377805
A.JPG	fruit	9	147401	(8.0, 2153.024647051241, 730.3342243268363)	inf	(8, 1850, 569, 9, 2462, 892)	65.53911951	711.7025913	711.7025913
A.JPG	fruit	10	140109	(9.0, 2573.5333062115924, 1077.3381224617976)	inf	(9, 2206, 941, 10, 2940, 1221)	64.44004035	810.1597085	810.1597085
A.JPG	fruit	11	150165	(10.0, 1270.962254852995, 1405.102374055206)	inf	(10, 954, 1211, 11, 1618, 1584)	65.94623908	785.7656447	785.7656447
A.JPG	fruit	12	152700	(11.0, 1154.8642436149312, 959.0019711853307)	inf	(11, 853, 755, 12, 1519, 1137)	66.31525922	777.788449	777.788449
A.JPG	fruit	13	170876	(12.0, 1807.1209005360613, 1830.2122065123247)	inf	(12, 1642, 1512, 13, 2004, 2135)	68.84844708	707.6905258	707.6905258
A.JPG	fruit	14	145829	(13.0, 693.7598900081603, 1116.9633886264048)	inf	(13, 546, 777, 14, 844, 1450)	65.30529944	745.311806	745.311806
A.JPG	fruit	15	231971	(14.0, 791.5439386819904, 2043.831793629376)	inf	(14, 535, 1743, 15, 1077, 2334)	76.23335339	787.4471612	787.4471612
A.JPG	fruit	16	126350	(15.0, 2428.7256588840523, 2405.9232528690145)	inf	(15, 2153, 2252, 16, 2702, 2559)	62.25757608	602.0659148	602.0659148
A.JPG	fruit	17	77819	(16.0, 1147.3519320474434, 1744.7801950680425)	inf	(16, 993, 1549, 17, 1300, 1947)	52.96988228	503.3923751	503.3923751
A.JPG	fruit	18	175013	(17.0, 1780.548953506311, 1087.031157685429)	inf	(17, 1625, 705, 18, 1952, 1476)	69.39964182	832.764112	832.764112
A.JPG	fruit	19	106593	(18.0, 2224.5662285515937, 1438.5422494910547)	inf	(18, 2072, 1205, 19, 2370, 1702)	58.82699816	567.8568822	567.8568822

Figure 5.3: Sample Comma-Separated Value File Content from BaoIMG

5.3.4.2 BaoQUANT

To use **BaoQUANT**, begin by selecting a model type (Volume, Mass, or Density) and clicking "**Run Model**" to estimate the mean and posterior distribution results in Figure 5.4. This approach assumes that your images were processed using the "**Feature Extraction**" option in **BaoIMG**, and "**Load CSV from BaoIMG**" is selected in **BoaQuant**.

If you prefer to use a previously saved CSV file, click "**Browse**", navigate to the file location, and upload it. A blue marker labeled "**Upload Complete**" will appear below the "**Browse**" button once the file is successfully uploaded. Before running the model, uncheck the box labeled "**Load CSV**

from BaoIMG" and then click "**Run Model**" to display the estimated mean values and posterior distribution results in Figure 5.4.

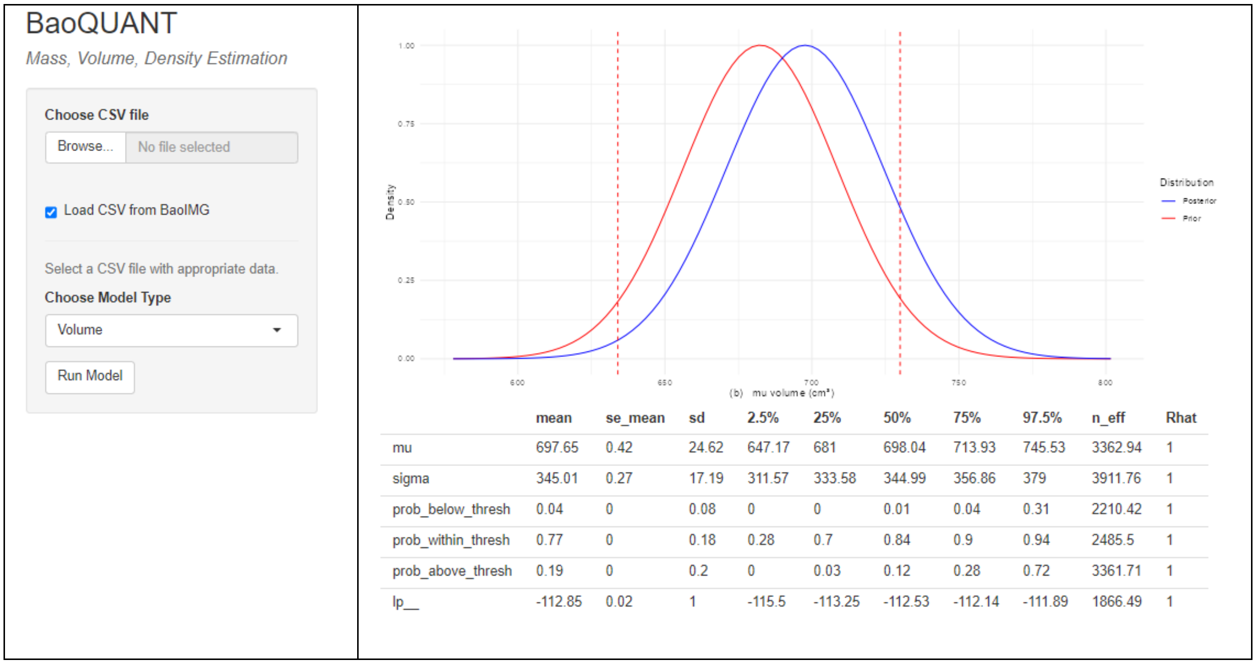

	mean	se_mean	sd	2.5%	25%	50%	75%	97.5%	n_eff	Rhat
mu	697.65	0.42	24.62	647.17	681	698.04	713.93	745.53	3362.94	1
sigma	345.01	0.27	17.19	311.57	333.58	344.99	356.86	379	3911.76	1
prob_below_thresh	0.04	0	0.08	0	0	0.01	0.04	0.31	2210.42	1
prob_within_thresh	0.77	0	0.18	0.28	0.7	0.84	0.9	0.94	2485.5	1
prob_above_thresh	0.19	0	0.2	0	0.03	0.12	0.28	0.72	3361.71	1
lp__	-112.85	0.02	1	-115.5	-113.25	-112.53	-112.14	-111.89	1866.49	1

Figure 5.4: Computed Results and Summary Statistics from BaoQuant

5.4 Future Improvements

Future work on the application should focus on key areas to enhance its performance and usability. One major improvement involves refining the image segmentation model by increasing the size and diversity of the training dataset. A larger dataset with more variations in lighting, background, fruit orientation, cluster, and size will improve the robustness of the segmentation algorithm, ensuring more accurate segmentation and feature extraction. The machine learning models that were used to estimate mass, volume, and density can also be improved by training with additional data.

Another critical enhancement will involve the implementation of perspective correction to ensure reliable morphological estimates. Currently, the measurements are most accurate when the images are captured at a fixed distance of 1.3 meters directly above the fruits. When perspective corrections are incorporated, the application can compensate for variations in camera angles and distances, which will enhance consistent and reliable feature extraction regardless of how the image is taken. This will improve the accuracy of mass, volume, and density predictions and ease the difficulty associated with image data capture, to make the application more robust for field use.

Alternative methods can be used to estimate the sample population distribution. This can be explored to complement the current Bayesian approach implemented in rstan. Non-parametric kernel density estimation techniques or classical frequentist statistical models can be used to provide additional insights or to validate results. These alternative approaches can improve the robustness of the population distribution analysis and provide a deeper understanding of *Adansonia digitata* fruit properties.

The application's accessibility and usability can be improved through cloud deployment, which would allow users to access it from different devices without requiring local installations. In a cloud environment, it becomes more convenient for field researchers and production planners to use. The cloud-based infrastructure can be further enhanced to facilitate real-time data sharing and collaborative analysis, allowing for a more dynamic research environment.

Finally, an important extension would be to adapt the application to other tree species. While the current focus is on *Adansonia digitata* fruits, the underlying methodology can be applied to the morphological analysis of other fruit-bearing native multipurpose species such as *Parkia biglobosa, Bombax costatum,* and even *Ziziphus mauritiana* and *Lannea spp*. These improvements will expand the application's scope and make it a more versatile tool for researchers and industries involved in fruit production and classification.

5.1 Conclusion and Recommendations

This chapter presented the development of an R Shiny application for *Adansonia digitata* fruit morphological analysis and Bayesian population estimation. The application automates the characterization of *Adansonia digitata* fruit and provides a statistical framework for inferring the sample fruit population. It can be applied more broadly in ecological research and *Adansonia digitata* fruit production and demonstrates the transformative potential of computer vision and machine learning in natural resource management.

The application will continue to evolve by implementing recommendations based on feedback from real-world users in *Adansonia digitata* production and research. Several R packages and Python libraries have been used to provide critical functions that enhance the application's performance. To ensure long-term usability, these dependencies must be monitored and updated whenever there are new releases that affect compatibility. By integrating the user-driven improvements and staying updated with new releases of libraries and packages, the application can maintain its relevance and effectiveness in ecological research and production planning.

References

Burns, C. P. (2023). pathspec. https://pypi.org/project/pathspec/

Chang, W., Cheng, J., Borges, B., Allaire, J. J., & Xie, Y. (2024). Shiny: Web application framework for R. RStudio, PBC. https://cran.r-project.org/package=shiny

Developer team mypy. (2023). mypy-extensions. https://pypi.org/project/mypy-extensions/

Developer team pycocotools. (2024). pycocotools. https://pypi.org/project/pycocotools/

Dono, F. X., Baatuuwie, B. N., Abagale, F. K., & Sørensen, P. B. (2024). Application of computer vision and machine learning in morphological characterization of *Adansonia digitata* fruits. *Smart Agricultural Technology*, 9. https://doi.org/10.1016/j.atech.2024.100528

FAIR. (2022a). fvcore. https://pypi.org/project/fvcore/

FAIR. (2022b). iopath. https://pypi.org/project/iopath/

Fay, C., Rochette, S., Guyader, V., & Girard, C. (2021). Engineering production-grade Shiny apps. In sustainability (Switzerland) (1st Edition, Vol. 11, Issue 1). Chapman and Hall/CRC. https://doi.org/https://doi.org/10.1201/9781003029878

Girshick, R. (2020). yacs. https://pypi.org/project/yacs/

Kheiralipour, K., & Kazemi, A. (2020). A new method to determine morphological properties of fruits and vegetables by image processing technique and nonlinear multivariate modeling. *International Journal of Food Properties*, 23(1), 368–374. https://doi.org/10.1080/10942912.2020.1729177

Longstaff, C. (2017). Development of Shiny app tools to simplify and standardize the analysis of hemostasis assay data: communication from the SSC of the ISTH. *Journal of Thrombosis and Haemostasis*, 15(5), 1044–1046. https://doi.org/10.1111/jth.13656

Łukasz Langa. (2025). black. https://pypi.org/project/black/

Oliphant, T. E., & Al., E. (2025). numpy. https://pypi.org/project/numpy/

OpenCV Team. (2025). opencv-python. https://pypi.org/project/opencv-python/

R Core Team. (2024). R: A Language and environment for statistical computing. https://www.r-project.org/

Regenstein, J. (2018). Reproducible finance with R. https://doi.org/10.1201/9781351052627

Rick van Hattem. (2024). portalocker. https://pypi.org/project/portalocker/

Saia, S. M., Nelson, N. G., Young, S. N., Parham, S., & Vandegrift, M. (2022). Ten simple rules for researchers who want to develop web apps. *PLoS Computational Biology*, 18(1), 1–18. https://doi.org/10.1371/journal.pcbi.1009663

Silva, C. A., Hudak, A. T., Vierling, L. A., Valbuena, R., Cardil, A., Mohan, M., de Almeida, D. R. A., Broadbent, E. N., Almeyda Zambrano, A. M., Wilkinson, B., Sharma, A., Drake, J. B., Medley, P. B., Vogel, J. G., Prata, G. A., Atkins, J. W., Hamamura, C., Johnson, D. J., & Klauberg, C. (2022). treetop: A Shiny-based application and R package for extracting forest information from LiDAR data for ecologists and conservationists. *Methods in Ecology and Evolution*, 13(6), 1164–1176. https://doi.org/10.1111/2041-210X.13830

Sinha, M. S., Shukla, R., & Rastogi, E. (2023). Computer vision applications and challenges: A review. *International Research Journal of Modernization in Engineering*, 3404(12), 3404–3414. www.irjmets.com

Soumith Chintala David Pollack, S. N. P. G. M. H. C. C. J. H. Z. N. X. Z. (2025). torchaudio. https://pypi.org/project/torchaudio/

SSCC, S. S. C. C. (2024). The structure of a Shiny app.

Sturm, R., Pollard, C., & Craig, J. (2017). Managing web-based applications. application performance management (APM) in the digital enterprise, 83–93. https://doi.org/10.1016/b978-0-12-804018-8.00007-3

Team, P. C. (2025). torchvision. https://pypi.org/project/torchvision/

Team, T. cloudpickle developer. (2025). cloudpickle. https://pypi.org/project/cloudpickle/

Terence Parr, S. (2024). antlr4-python3-runtime. https://pypi.org/project/antlr4-python3-runtime/

The pip Developers. (2025). pip. https://pypi.org/project/pip/

Tran, H. M., Pham, K. T., Vo, T. M., Le, T. H., Huynh, T. T. M., & Dao, S. V. T. (2023). A new approach for estimation of physical properties of irregular-shaped fruit. *IEEE Access*, 11, 46550–46560. https://doi.org/10.1109/ACCESS.2023.3273777

Tyagi, A. K., & Rekha, G. (2019). Challenges and applications for implementing machine learning in computer vision, *IGI Global,* 92–118. https://doi.org/10.4018/978-1-7998-0182-5.ch004

Wang, F., Wu, D., Yamamoto, H., Xing, S., & Zang, L. (2016). Digital image analysis of different crown shape of *Platycladus orientalis*. *Ecological Informatics*, 34, 146–152. https://doi.org/10.1016/j.ecoinf.2016.06.002

Yadan, O. (2022). omegaconf. https://pypi.org/project/omegaconf/

Yadan, O. (2023). hydra-core. https://pypi.org/project/hydra-core/

CHAPTER SIX

ESTIMATING YIELD OF *PARKIA BIGLOBOSA* FRUITS FROM FIELD DATA AND IMAGE-BASED PREDICTIVE MODELS

6.1 Introduction

Accurate estimates of tropical tree fruit yields are essential for the socioeconomic development of many African countries. These yield estimates help to assess the productivity of individual trees, implement effective management practices, and estimate market supply in the face of changing climatic conditions. Therefore, a solid understanding of the factors that influence yield size is crucial for making improved yield predictions under various conditions. Morphology, soil properties, management practices and local climatic conditions determine the yields of trees. Tree morphological variables were utilized by Liu *et al.* (2023) for non-destructive biomass assessment of tropical trees, demonstrating the importance of structural characteristics in understanding tree productivity.

Spectral properties of the crown may disclose the health condition of the tree and thus properties relevant for the yield of fruit harvest. Recent advancements in global positioning systems (GPS), geographic information systems (GIS), remote sensing and drone technology have improved landscape visualization and governing factors (Naqvi and Naqvi, 2022). These technologies combined with yield data, allow for better prediction of yield. Tree traits and climate are important predictors of production, which can be estimated accurately from remotely sensed images (Panagiotidis *et al.*, 2017) by both manual and automated methods. In several cases, there has been considerable success in predicting yield with spectral indices (Panda *et al.*, 2010). For instance, cotton yields have been accurately estimated from spectral indices and texture features derived from RGB images (Yiru *et al.*, 2022).

Plant traits influence the spectral signals captured by drones and satellites, enabling studies on vegetation health, production, distribution, and functionality over large areas (Hauser *et al.*, 2021; Houborg *et al.*, 2015; X. Ma *et al.*, 2019; Thomson *et al.*, 2018). Variation in tree leaf colour, shape, canopy cover (Ribeiro da Luz and Crowley, 2010), and yield (Apolo-Apolo *et al.*, 2020b; Barbosa *et al.*, 2021) can be determined from spectral characteristics.

In contrast to spectral signals, which provide indirect measures of vegetation health and productivity through indices derived from reflectance patterns, tree traits provide direct insights into tree yield. The tree growth rate, annual circumference, and wood density are key traits that can significantly influence the productivity and yield of trees (Prado-Junior *et al.*, 2016). The impact of these traits on the tree yields can vary based on human pressure, climatic, and management conditions (Prado-Junior *et al.*, 2016).

In the case of the *Parkia biglobosa,* a multipurpose native tree heavily dependent on by folks for its nutritional, health, and socio-economic benefits, estimating its annual production of fruits is a challenge due to human pressure (Prado-Junior *et al.*, 2016) and technological changes. Fruits are randomly harvested and used by local people, hindering systematic data collection (Houndonougbo *et al.*, 2020). However, pod yield is correlated with crown diameter and diameter at breast height, though stronger with crown diameter, and it fluctuates significantly across years due to climate and management practices (Bokary *et al.*, 2022).

Among savanna shrub species in West Africa, crown volume is the stronger predictor of fruit production than stem diameter, with larger trees yielding more fruits under climate influence (Ounyambila *et al.*, 2018). In their model, Ounyambila *et al.* (2018) incorporated climatic factors and this research extends their approach by adding both soil, drone, and satellite spectral characteristics to assess the fruit yield of *Parkia biglobosa* using a modified version of their model.

While significant research exists on yield, tree form, vegetation health, climate, and soil, the factors are rarely integrated into a unified framework for yield studies. This study combines tree form, vegetation health indices (from drones and satellite images), and existing soil variables into a mathematical model to wholistically assess their interactions and contribution to the yield of *Parkia biglobosa* pods, and to assess the potential for larger scale applications. Thus, the study intends to address the challenges in the yield estimation of this multipurpose native tree to help estimate market supply and implement sustainable management practices in the face of changing climatic conditions.

6.2 Materials and Methods

6.2.1 Study Area

The study was conducted in three sites in northern Ghana; Nandom Municipal (2°41′-2°54′ W and 10°44′-11°00′ N) in the Upper West Region, Kasena-Nankana Municipal (1°10′-0°53′ W, and 10°30′-11°01′ N) in the Upper East Region, and Kumbungu District (1°14′-0°53′ W and 09°25′-0°11′ N) in the Northern Region (Figure 6.1).

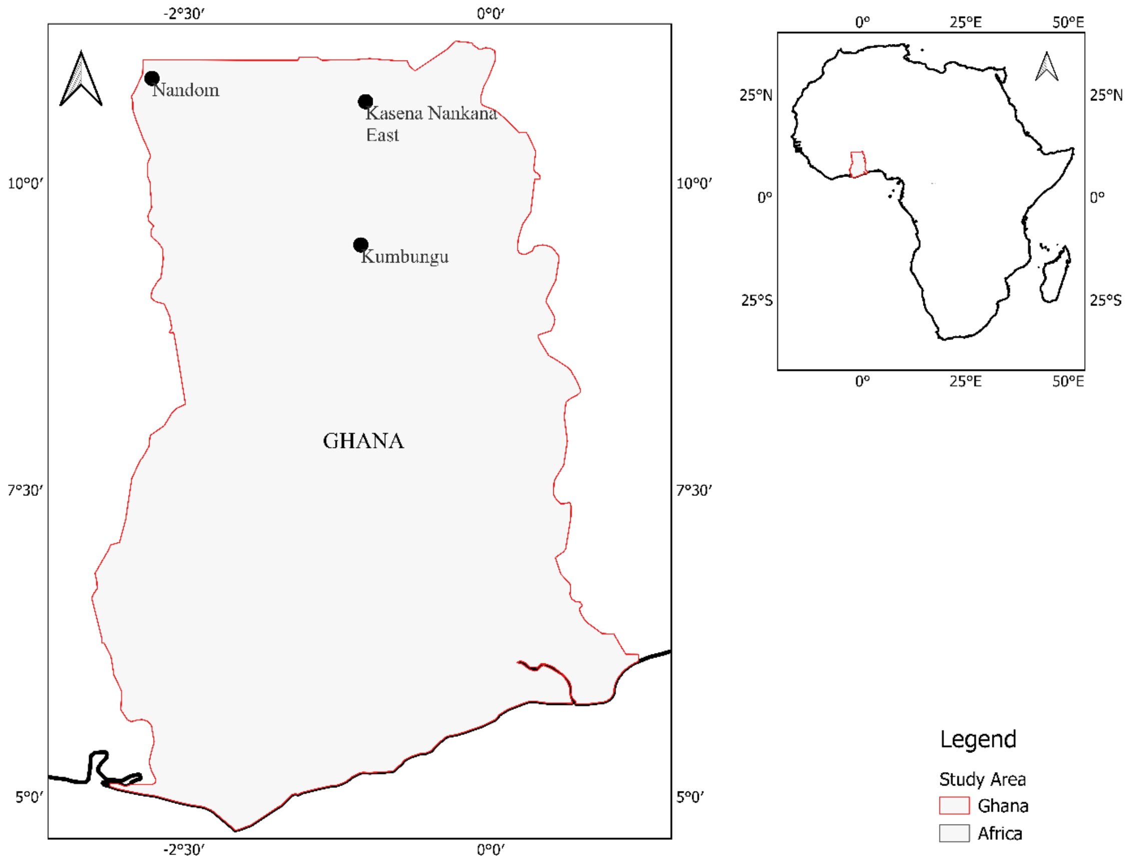

Figure 6.1: Study Areas in Northern Ghana

The study areas experience a unimodal rainfall pattern from May to October. Average annual rainfall varies by location, with Nandom receiving approximately 999 mm, Kasena-Nankana 1002 mm, and Kumbungu 1078 mm. The monthly average temperatures are 28.9°C in Nandom, 29.1°C in Kasena-Nankana, and 28.8°C in Kumbungu (Harris *et al.*, 2020).

The soil types common to all three study areas are Lixisols and Fluvisols. In addition, Nandom has Arenosols and Vertisols, Kasena-Nankana has Leptosols, and Kumbungu has Planosols, Plinthosols, and Acrisols (Soil Research Institute, 1999). Coupled with erosion, a widespread phenomenon, the various soil types vary in their sand and clay content.

Agriculture is the primary economic activity supported by the soils in the study areas. Most households are involved in subsistence farming, growing crops such as millet, sorghum, maize, and groundnuts (Nandom Municipal Assembly, 2016). Additionally, livestock contributes extra income and food. The trade of *Parkia biglobosa* is particularly important for livelihood support. During the dry season, bushfires threaten *Parkia biglobosa* by damaging both seedlings and trees. The impact on yield loss is exacerbated by climate change and poor land management practices.

6.2.2 Study Species

Parkia biglobosa is common in the Sudanian zones up to the edge of the Sahel in West and Central Africa and occurs in savannas, fields, and fallows. It is a deciduous tree up to 20–30 m high, and it belongs to the family Fabaceae (Komolafe *et al.*, 2024). It starts fruiting at the age of eight years and yields 25-100 kg of pods/tree/year when it is 15 to 20 years old (Pasiecznik, 2022). The fruit is a slightly curved, brown, indehiscent pod, 30-40 cm long and 2-3 cm wide. It produces 5 to 20 seeds per pod (Ayanrinde *et al.*, 2023).

6.2.3 Field Sampling Data

Mature *Parkia biglobosa* trees were sampled using a grid-based spatial sampling framework. A 300 × 300 m grid was overlaid on each study site, and grid cells within settlement areas with relatively high tree density were identified. Within these cells, unharvested mature trees were selected, georeferenced, and linked to orthomosaic images derived from drone surveys for crown-level analysis. A total of 105 trees were sampled, comprising 32 in Kumbungu, 49 in Nandom, and 24 in Navrongo. Differences in sample size across sites reflect variation in tree density and the availability of eligible trees within the sampled grids. Harvesting was between March and April when the pods turned brown and dry. All fruits were harvested using climbing and sickle-plucking techniques, then weighed in-situ to determine the yield per tree in kilograms.

6.2.4 Drone Images

The sites were overflown with the DJI mini 2 drone equipped with 12-megapixel RGB (red, green, blue) sensors of focal length 35 mm. Flight missions were planned and completed using Dronelink software (Dronelink, 2022). Forward and lateral overlaps were 80 % and 70 %, respectively (Federman *et al*., 2017). Images were automatically geotagged using the onboard global positioning system.

The images were used to derive orthomosaic maps. *Parkia biglobosa* populations were identified on the maps by their location coordinates. The crown area for an identified tree was measured in square meters by calculating the area of a polygon delineated around the crown in QGIS. The red, green, and blue spectral bands were extracted, and their average values were calculated as R.x, G.x, and B.x respectively. In addition, the tree health indices Normalized Green Red Difference Index (NGRDI), Green Leaf Index (GLI), Simple Ratio (SR), Chlorophyll Index (CI), Brightness, Greenness, Wetness were calculated and their impact on yield was investigated together with the crown radius and soil parameters.

6.2.5 Satellite Images, Climate and Soil Data

Satellite images from the Norway International Climate and Forest Initiative (NICFI) satellite data program with 5-meter resolution were obtained and used to compute tree health indices. The boundary shapefiles for the study sites were used to extract the red, green, blue and near-infrared bands. Averages for the red, green, blue, and near-infrared bands were calculated for each crown region as R.y, G.y, B.y, and N respectively. The Normalized Difference Vegetation Index (NDVI) was calculated in addition to the pervious indices differentiated by suffix ".x" and ". y" for common-named drone and satellite indices respectively. The spectral indices were used to capture complementary aspects of canopy condition, as no single index fully represents vegetation structure, chlorophyll content, and stress. Combining indices improves sensitivity to different biophysical properties and enhances yield prediction robustness (Xue & Su, 2017)

Macro climatic variables were extracted from the gridded Climatic Research Unit Time-series data version 4.07 (Harris *et al.*, 2020). The data contained month-by-month variations in precipitation and daily mean temperature from 1901 to 2022 on 0.5° x 0.5° grids. The boundary shapefiles were used to extract precipitation, and temperature values for the three study areas. They were filtered for records within the year preceding the year 2023 and used to construct annual mean precipitation and temperature metrics.

Soil data was obtained from a global soil data product (SoilGrids) generated by the International Soil Reference and Information Centre (ISRIC) at six standard depth intervals and a spatial resolution of 250 meters (Poggio *et al.*, 2021). Using the tree locations, the soil sand, clay, and silt content, nitrogen, soil pH in water (pH), bulk density (BD), cation exchange capacity at pH 7 (CEC), Coarse fragments volumetric (CFVO), and soil organic carbon (SOC) were extracted at intervals from a depth of 5 to 200 centimeters and their impact on yield was investigated.

6.2.6 Relationships Modelling

We assumed that the yield per tree (measured in kilograms) exhibited a nonlinear relationship with crown radius, where doubling the crown radius resulted in a greater-than-proportional increase in yield. This assumption reflects the three-dimensional nature of the crown structure, where increases in diameter lead to exponential increases in crown volume and hence yield. Again, we expected trees of different sizes to produce varying amounts of harvest, with larger trees showing more variation in their production than smaller trees. To simplify this complex relationship, the model utilized logarithms to transform it into a linear relationship. This was done in the following format.

The yield of a tree was modelled as a product of the global yield coefficient term, explanatory variables (drone-based spectral indices, satellite-based spectral indices, and soil properties), a categorical variable (location, climate, etc.), and interaction terms. These were analyzed using Ordinary Linear Least Squares (OLS) models of the logarithmic yield as a function of variables and their interactions. All models include an error term (ε), specified in equations (1), but omitted in subsequent expressions for simplicity. The errors, however, are accounted for in estimation and validation. The generalized exponential model was specified as:

$$Y_j = \beta_0 \cdot r^n \cdot \prod_{i=1}^{I}\left[e^{\beta_i \cdot X_i}\right] \cdot f(Location, interactions).\,\varepsilon \qquad \ldots (1)$$

$$Y_j = \underbrace{\beta_0 \cdot r^n}_{\text{Global Term}} \cdot \underbrace{\prod_{i=1}^{I}\left[e^{\beta_i \cdot X_i}\right]}_{\text{Explanatory Variable (Predictors)}} \cdot \underbrace{e^{(\gamma_j + \sum_{k=1}^{I} \alpha_{jk} \cdot X_k)}}_{\text{Location, interactions}} \qquad \ldots (2)$$

Where Y represents the yield of the tree, and the global coefficient β_0 provides the baseline yield estimate. The global term $\beta_0 \cdot r^n$ estimates the expected yield from a tree with crown radius *r*, representing a global mean value. The exponent n defines the relationship between size and yield: when n=2, yield is proportional to the surface area of an ideal spherical crown, and when n=3, yield is proportional to the crown volume. The fitted n value adjusts for structural traits.

X_i represents the i^{th} variable in a set of total i explanatory variables, with β_i as the coefficient, quantifying the influence of the variable X_i on the yield Y. These variables include factors like soil properties, climate, and spectral characteristics of the crown, which may influence or indicate yield. Each location has its own coefficient γ_j, quantifying its influence on yield, for location j, where the total number of locations is J. The variable α_{jk} models the interaction between explanatory variables X_k (e.g. drone, satellite, soil) and the location.

The logarithm model is derived from Equation 2 as

$$\ln(Y_j) = \ln(\beta_0) + n \cdot \ln(r) + \sum_{i=1}^{I} \beta_i \cdot X_i + \gamma_j + \sum_{j=1}^{J} \sum_{k=1}^{I} \alpha_{jk} \cdot X_k \qquad \ldots (3)$$

Estimating interaction coefficients α_{jk} can be challenging if the dataset does not sufficiently capture all combinations of location X_i values. In such cases, neglecting the interactions simplified Equation 3 to:

$$\ln(Y_j) = \ln(\beta_0) + n \cdot \ln(r) + \sum_{i=1}^{I} \beta_i \cdot X_i + \gamma_j \qquad \ldots (4)$$

Since $\ln(\beta)$ is a constant, it can be replaced with β_0' for all practical purposes

Typically, the variation due to X_i and between locations and individual trees as reflected by the β_i and γ_j values will not be highly dominant, therefore, the Taylor approximation of the exponential function ($e^x \approx 1 + x$) for small numeric values of x is useful for inference as:

$$Y_j \approx \beta_0 \cdot r^n \prod_{i=1}^{I} (1 + \beta_i \cdot X_i) \cdot (1 + \gamma_j) \qquad \dots (5)$$

Hence, if the effect of location j is γ_j=0.2, then the location is approximately 20 % higher in yield compared to the other location under the same conditions for all other factors and the same size of tree. Where γ_j are the coefficients corresponding to each location.

Interactive-Form-Models were specified out of Equation 3 to include soil, drone, and satellite-based parameters, location, and their interactions (Table 6.1).

Table 6.1: Models with Interaction Terms

$\ln(yield) = \beta_0' + n \times \ln(r) + \beta_1 \times soil + \beta_2 \times Location + \beta_3 \times soil \times Location$	… (3.1)
$\ln(yield) = \beta_0' + n \times \ln(r) + \beta_1 \times drone + \beta_2 \times Location + \beta_3 \times drone \times Location$	… (3.2)
$\ln(yield) = \beta_0' + n \times \ln(r) + \beta_1 \times satellite + \beta_2 \times Location + \beta_3 \times satellite \times Location$	… (3.3)
$\ln(yield) = \beta_0' + n \times \ln(r) + \beta_1 \times drone + \beta_2 \times soil + \beta_3 \times Location + \beta_4 \times soil \times Location$	… (3.4)
$\ln(yield) = \beta_0' + n \times \ln(r) + \beta_1 \times satellite + \beta_2 \times soil + \beta_3 \times Location + \beta_4 \times soil \times Location$	… (3.5)
$\ln(yield) = \beta_0 + n \times \ln(r) + \beta_1 \times drone + \beta_2 \times satellite + \beta_3 \times soil + \beta_4 \times Location + \beta_5 \times soil \times Location$	… (3.6)

Basic-Form-Models (models without interaction terms) were also specified from Equation 4 (Table 6.2).

Table 6.2: Models with No Interaction Terms

$\ln(yield) = \beta_0' + n \times \ln(r) + \beta_1 \times Location$	… (4.1)
$\ln(yield) = \beta_0' + n \times \ln(r) + \beta_1 \times soil + \beta_2 \times Location$	… (4.2)
$\ln(yield) = \beta_0' + n \times \ln(r) + \beta_1 \times drone + \beta_2 \times soil + \beta_3 \times Location$	… (4.3)
$\ln(yield) = \beta_0' + n \times \ln(r) + \beta_1 \times satellite + \beta_2 \times soil + \beta_3 \times Location$	… (4.4)

6.2.6.1 Selection and Validation of Models

A series of simple OLS models combining the global term with different drone, satellite, and soil variables was used to avoid model overfitting (Madin and Nelson, 2023). A repeated random sampling of data with holdout for final validation was adopted for model selection. The data was divided into two parts: 80 % for training and 20 % for final validation and a balanced representation from each location was ensured. Using 80 % of the training dataset, we sampled a balanced representation repeatedly over 4000 iterations to build models. The Akaike information criterion was used in each iteration to select the best model which was stored. After all iterations were completed, the most frequently occurring model was selected. The selected model was validated using the reserved validation dataset to assess its performance. The process was implemented using the caret package for data partitioning, while the lm() function in R was used for fitting the linear models.

The selected models were used to estimate yield on the validation dataset and evaluated using R^2, root mean squared error (RMSE) and mean average error (MAE) as metrics to assess how well they would perform in production.

6.3 Results and Discussion

6.3.1 Field Sampling Data

The yield of *Parkia biglobosa* fruits ranged from 4.0 kg to 218.0 kg per tree with a median yield of 56.0 kg and an average yield of 57.0 kg. The highest and lowest yields were recorded in Kumbungu, where the median yield was 26.5 kg, and the average yield was 37.6 kg. The yield from Nandom ranged from 27.0 to 139.0 kg with a median of 68.0 kg and an average of 69.5 kg. The yield from Navrongo ranged from 10.0 to 90.0 kg with a median of 64.0 kg and an average of 57.3 kg (Figure 6.2, part a).

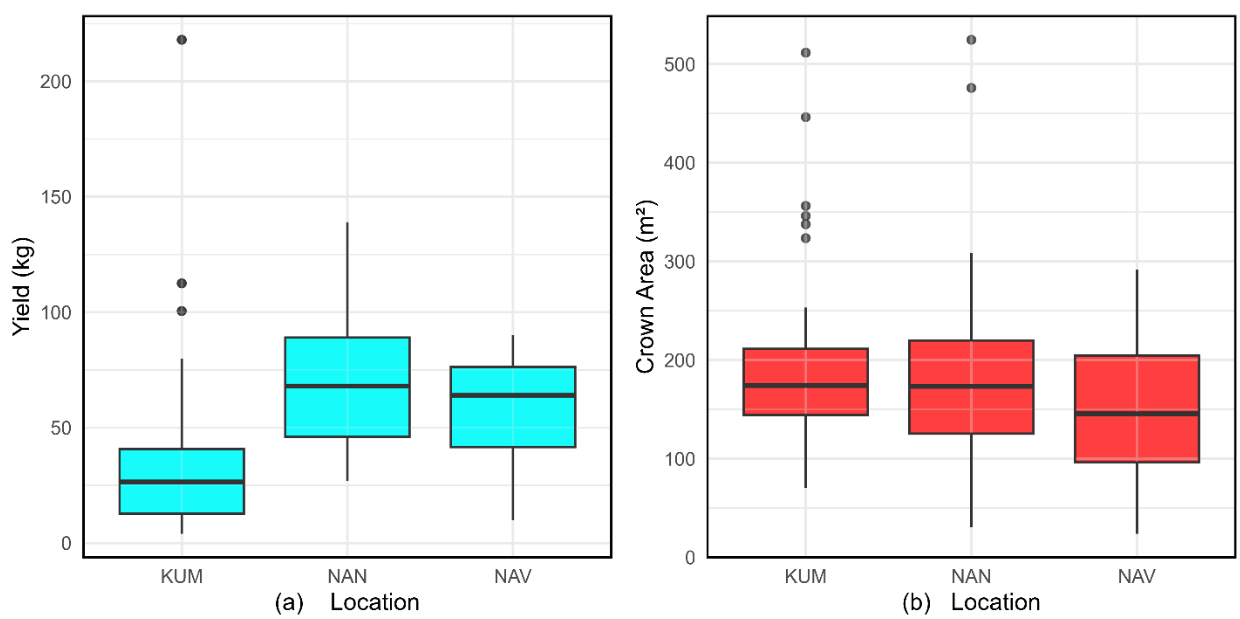

Figure 6.2: Overview of Yield (a) and Crown Area (b) in the Three Study Areas.

Tree production varied across the study sites and the range of values observed closely aligned with previously reported ranges in the literature, i.e., 25 - 100 kg/tree (Pasiecznik, 2022) and 25-130 kg/tree (Houndonougbo *et al.*, 2020), while others deviated significantly. The variation suggested that there could be differences in conditions and practices in production. These could be due to soil quality, climate, or vegetation health conditions not considered. The range widens, 0.25 - 200 kg/tree, when climate and management practices are taken into consideration (Bokary *et al.*, 2022).

Generally, crown areas range from 23.87 to 524.6 m^2 per tree. The median and average crown areas were 167.9 and 180.3 m^2 per tree, respectively. In Kumbungu the crown areas varied from 70.3 to 511.6 m^2 per tree, with a median and mean of 174.1 and 203.5 m^2 per tree, respectively. The range of values from Nandom was 30.5 to 524.6 m^2 per tree, with median and mean values of 173.3 and 179.5 m^2 per tree, respectively. Values from Navrongo were from 23.9 to 291.8 m^2 per tree, with median and mean values of 145.6 and 151.0 m^2 per tree, respectively, Figure 6.2 (part b). Thus, the largest and smallest tree crowns were found in Nandom and Navrongo, respectively.

The variability of canopy areas of *Parkia biglobosa* across the study sites points to the influence of management and environmental factors on tree growth. Areas with higher mean precipitation exhibited larger canopy areas, suggesting that moisture availability impacts canopy growth. They could also be due to differences in soil factors (Alo and Aweto, 2018). The canopy sizes observed in this study were consistent with reports on canopy diameter of 12-19 m, which approximately ranges from 113 - 284 m^2, assuming circular canopies.

6.3.2 Relationships Modelling

6.3.2.1 Selection of Models

The models with interaction terms (interactive-form models) that were used to explain the yield in the training data accounted for 53.7 % to 64.4 % of the variation in yield. Model 3.6 was the best in R^2 (64.4 %) but not the lowest in AIC (115). The model combined the natural log of crown radius (r), drone CI (CI.x), Near-Infra-Red (N) from satellite images, location-specific effects and interactions with N. The most parsimonious was Model 3.4, with AIC (112.5), a strong R^2 (63.1 %) and lowest standard deviation (0.039) (Table 6.3).

Table 6.3: Summary of Performance Metrics of Interactive-Form Models for Estimation of Fruit Yield.

The variables B.x and B.y represent average spectral reflectance values obtained from drone and satellite images, respectively. [D] and [E] denote soil depth intervals of 30–60 cm and 60–100 cm, respectively.

Model	Formula: ln(Yield) ~	Mean AIC	Mean R^2 (%)	SD R^2
3.1	ln(r) + Sand[D] * Location	115.1	60.9	0.042
3.2	ln(r) + B.x * Location	127.8	53.7	0.046
3.3	ln(r) + B.y * Location	126.3	55.4	0.039
3.4	ln(r) + NGRDI.x + Sand[D] * Location	112.5	63.1	0.039
3.5	ln(r) + N + Nitrogen[E] * Location	114.0	63.0	0.050
3.6	ln(r) + CI.x + N + Nitrogen[E] * Location	115.0	64.4	0.051

The models with no interaction terms (basic-form models) showed progressive improvement in their ability to explain variation in yield from the training data. Model 3.5 exhibited the highest explanatory power of 60.9 % in the training data. The model incorporated the natural log of crown radius, drone NGRDI, N, and CEC[F] at 100–200 cm depth and accounted for location effect. It was also the most parsimonious with the least AIC (117.6) and standard deviation (0.035) (Table 6.4).

Table 6.4: Summary of Performance Metrics of Basic-Form Models for Estimation of Fruit Yield.

The variables B.x and B.y represent average spectral reflectance values obtained from drone and satellite images, respectively. [D] and [F] refer to soil depth intervals of 30–60 cm and 100–200 cm, respectively.

Model	Formula: ln(Yield) ~	Mean AIC	Mean R^2 (%)	Std. R^2
4.1	ln(r) + Location	138.2	42.5	-
4.2	ln(r) + CEC[F] + Location	122.1	55.1	0.040
4.3	ln(r) + NGRDI.x + CEC[F] + Location	119.6	58.2	0.038
4.4	ln(r) + N + pH[D] + Location	119.3	58.1	0.049
4.5	ln(r) + NGRDI.x + N + CEC[F] + Location	117.6	60.9	0.035

6.3.2.1.1 Model Validation

The RMSE values for interactive-form models (model 3.1- 3.6) ranged from 0.38 to 0.45 and MAE from 0.28 to 0.36. Model 3.3 was the highest performing model in the group. It achieved an MAE of 0.31, RMSE of 0.38 and R^2 of 75 % (Table 6.5).

Table 6.5: Validation Metrics for Interactive-Form Models

Model	R^2 (%)	RMSE	MAE
3.1	65.2	0.44	0.35
3.2	64.5	0.45	0.36
3.3	75.0	0.38	0.31
3.4	67.1	0.43	0.33
3.5	72.6	0.39	0.28
3.6	67.7	0.43	0.35

It indicated a better fit and stronger predictive capability (Figure 6.3 Part A).

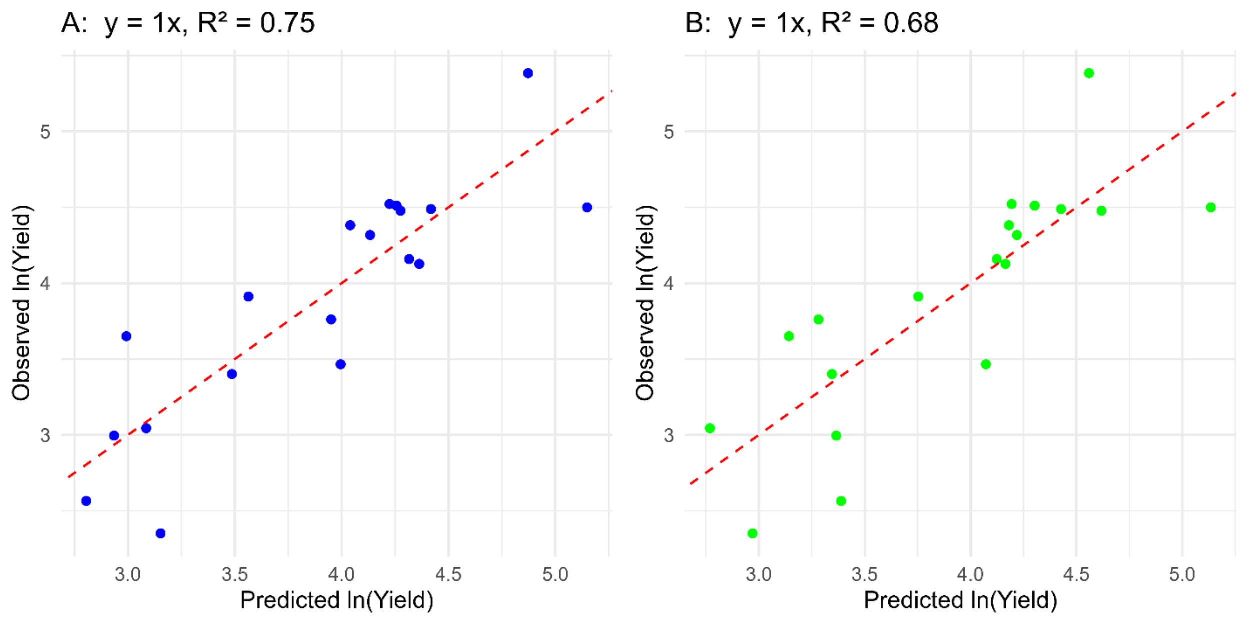

Figure 6.3: Regression of Natural Logarithm Values of Observed Yield of Parkia biglobosa Pods on their Predicted Values.

The interactive terms enhanced the predictive accuracy; thus, the interaction effect is important in *Parkia biglobosa* yield prediction.

The RMSE values of the basic-form models (model 4.1-4.5) ranged from 0.43 to 0.46, their MAE values were between 0.34 and 0.39, and R^2 values ranged from 0.63 % and 0.69 % (Table 6.6).

Table 6.6: Validation Metrics for Basic-Form Models.

Model	R^2 (%)	RMSE	MAE
4.1	62.9		
4.2	62.9	0.46	0.39
4.3	64.9	0.45	0.37
4.4	67.8	0.43	0.34
4.5	64.9	0.45	0.37

Model 4.4 achieved the best fit in the validation data, with RMSE of 0.43, MAE of 0.34, and R^2 of 0.68 (Figure 6.3 Part B).

6.3.3 Model Coefficients

The coefficient of the natural logarithm of the crown radius, i.e., ln(r), consistently exhibited a positive effect on yield across all models. In interactive-form models, the effect of nitrogen varied across location: it was consistently negative in Navrongo, variable in Nandom, and positive in Kumbungu. Variables such as sand and the average of the blue spectral bands of drone and satellite images (B.x and B.y, respectively) also showed mixed significance across models. In the presence of nitrogen interactions, CI.x and N were mostly impactful. Thus, yield is influenced by ln(r), effect of sand, spectral bands, and nitrogen interactions (Appendix 3).

Considering the basic-form models, the effect of CEC[F] was mostly similar, though negative. Nandom and Navrongo mostly showed positive impacts. Other variables such as NGRDI.x, pH[D], and N exhibited mixed significance (Appendix 4).

6.3.4 Best Models

The best interactive-form model was model 3.3 (Appendix 3), it generalized well in the validation data, and indicated that yield depended on the combination of the base factor and the response to crown radius (r), average blue (B.y) from satellite images, location-specific effects and interactions with B.y. There was a strong balance between model explanatory power (R^2 = 75 %) and predictive accuracy (RMSE = 0.38, MAE = 0.31) (Table 6.5). The exponentiated equation was stated as:

$$Y_j = e^{5.322} \cdot r^{1.037} \cdot e^{-0.008 \cdot B.y} \cdot (Location\ Effect)_j \qquad \ldots (6)$$

Where:

$$Location\ Effect = \begin{cases} J = 1: & e^{-2.857+0.009 \cdot B.y}, \quad Nandom \\ J = 2: & e^{-5.975+0.013 \cdot B.y}, \quad Navrongo \\ J = 3: & 1, \quad Kumbungu \end{cases}$$

The best basic-form model was model 4.4 (Appendix 4). It indicated that yield depends on the combination of base factors and the response to crown radius (r), near-infrared (N) from satellite images, soil pH at 30 - 60 cm depth (pH[D]) and location-specific effects. The R^2 was 67.8 %, RMSE 0.43 and MAE 0.34 (Appendix 6.6). The exponentiated equation was stated as:

$$Y_j = e^{-15.699} \cdot r^{0.989} \cdot e^{0.001N+0.242pH[D]} \cdot (Location\ Effect)_j \qquad \ldots (7)$$

Where:

$$Location\ Effect = \begin{cases} J = 1: & e^{0.153}, \quad Nandom \\ J = 2: & e^{-0.488}, \quad Navrongo \\ J = 3: & 1, \quad Kumbungu \end{cases}$$

The global coefficient $e^{-15.699}$ is approximately 1.52 x 10^{-7}, a number close to zero, indicating that the intercept plays a minimal role in predicting yield. Thus, the effect of the variables are the major determinants of yield.

Yield is influenced by an interplay of physical, biological, and environmental factors. The exponential relationship between tree traits, as depicted in the global term, has been extensively used in allometric studies and yield predictions (Chave *et al.*, 2014; Duncanson *et al.*, 2015; Liu *et al.*, 2023; Peters *et al.*, 1988). The results of the global term have been enhanced by incorporating climate (Ounyambila *et al.*, 2018), soil, and management practices (Madin and Nelson, 2023), each of which is considered separately. A more comprehensive approach is adopted in this study by combining soil, tree health, and effects of locality to the global term in a generalized exponential framework to improve results over earlier approaches.

In respect of *Parkia biglobosa,* found that yield is significantly explained by crown diameter (or radius) in a linear relationship (Bokary *et al.*, 2022). In this study, it was observed that the relationship is not linear, but nonlinear with a power close to 1. When interaction terms are not considered, it increases by increasing crown size at a decreasing rate (n = 0.989). On the contrary, when interaction terms are considered, it increases at an increasing rate (n = 1.037). A more extreme nonlinear effect (about twice) was observed in shrubs of the Sudanian zone (*Ximenia americana*), where yield grows at an increasingly faster rate as crown radius increases (Ounyambila *et al.*, 2018). This could be explained by differences in physical and biological properties, since trees and shrubs may respond to environmental and management factors in unique ways.

The near-linear relationships observed could be explained by the age of the tree branches, harvesting practices, and environmental stressors. Younger branches tend to produce more fruits, while older ones experience reduced fruit-bearing capacity due to physiological changes, reduced nutrient flow, and diminished utility (Boffa, 1999; Zhou and Melgar, 2020). Common harvesting practices that use sickle blades to cut off fruit-bearing branch tips create scars, which lead to reduced fruit production. Environmental stressor further increases yield loss in *Parkia biglobosa*. Bushfires, for instance, can damage lower branches by burning undergrowth that serves as fuel, leading to localized flower abortion, uneven fruiting, and reduced yield.

Improvements in Models 3.3 and 4.4, achieved by adding soil conditions and/or satellite spectral characteristics to the structural trait of *Parkia biglobosa*, led to better yield predictions. Compared to the linear model from Bokary *et al.* (2022). Over 67 % of explanatory power suggests that it is capturing complexities effectively. It, however, agrees with his assertion that *biglobosa* crown diameter (or radius) is a good predictor of its fruit yield. Compared to similar non-linear models for predicting yield in distinct climates (R^2 = 46.0 %) (Ounyambila *et al.*, 2018), an R^2 margin of improvement between 21 and 29 percentage points was observed.

6.4 Conclusions and Recommendations

The yield of *Parkia biglobosa* is influenced by its crown radius, soil properties, spectral characteristics, and location-specific variations in a non-linear relationship. Integrating these factors leads to a more accurate prediction of yield, which can inform better decision-making and yield optimization strategies.

The model is applicable in scenarios where multiple variables influence yield. In regional yield studies with field measurements from drones, satellite imagery, and soil parameters, the images can be used to estimate crown radius, then the model can be used to capture the nonlinear dynamics, providing a more realistic forecast.

Model 3.3 expresses yield as an exponential function of crown radius (r), blue reflectance (B.y) from satellite images, and location-specific effects. It is the best model for estimating yield when considering interactions between predictors and location-specific effects. It provides the strongest balance between model fit, explanatory power (R^2 = 75 %), and predictive accuracy (lowest RMSE and MAE). Model 4.4 is simpler, with no interaction terms, and expresses yield as an exponential function of crown radius (r), near-infrared reflectance (N), soil pH at 30 – 60 cm (pH[D]), and specific-location effects.

Depending on whether interaction terms are considered or not, the rate of yield growth could gradually increase with increasing crown radius or vice versa, highlighting the importance of considering the influence of local environmental factors, which can modify the crown radius-yield relationship differently across regions.

In addition, location-specific management practices should be implemented to optimize soil health and enhance the accuracy of large-scale *Parkia biglobosa* yield predictions by leveraging spectral indices derived from remote sensing. To maintain yield estimates, targeted policies are needed for bushfire control, less invasive harvesting techniques, and monitoring of nitrogen levels, soil pH, and tree crown radius. Effective bushfire management and undergrowth protection training are vital for tree health and productivity.

References

Alo, E. A., & Aweto, A. O. (2018). The Properties of soil under the canopy of the locust bean *tree (Parkia biglobosa),* in relation to tree biomass, in farmland in Oyo area, South Western Nigeria. *Journal of Environmental and Earth Sciences, 8*(8), 38–46.

Apolo-Apolo, O. E., Martínez-Guanter, J., Egea, G., Raja, P., & Pérez-Ruiz, M. (2020b). Deep learning techniques for estimation of the yield and size of citrus fruits using a UAV. *European Journal of Agronomy*, *115*, 126030. https://doi.org/10.1016/j.eja.2020.126030

Asad Naqvi, S. A., & Naqvi, R. Z. (2022). Geographical information systems (GIS) in industry 4.0: Revolution for sustainable development. *Handbook of Smart Materials, Technologies, and Devices: Applications of Industry 4.0: Volume 1-3*, *3*, 2289–2315. https://doi.org/10.1007/978-3-030-84205-5_83

Ayanrinde, F. A., Oyewole, S. O., Ayanrinde, O. A., & Oyewole, A. L. (2023). Importance of *Parkia biglobosa* (African Locust Beans) to the women livelihoods in Ibarapa North and Ibarapa Central local government areas of Oyo State, Nigeria. *Journal of Applied Sciences and Environmental Management*, *27*(9), 2097–2100. https://doi.org/10.4314/jasem.v27i9.27

Barbosa, B. D. S., Ferraz, G. A. e. S., Costa, L., Ampatzidis, Y., Vijayakumar, V., & dos Santos, L. M. (2021). UAV-based coffee yield prediction utilizing feature selection and deep learning. *Smart Agricultural Technology*, *1*, 100010. https://doi.org/10.1016/j.atech.2021.100010

Boffa, J.-M. (1999). Agroforestry parklands in sub-Saharan Africa. Food and Agriculture Organization of the United Nations. https://www.fao.org/4/x3940e/X3940E06.htm#ch4.

Bokary, A. K., Amadou Malé, K., & Sidiki, G. D. (2022). Effect of climatic zone and land use practices on pod, seed, and pulp yield of *Parkia biglobosa* in Southern Mali. *International Journal of Scientific Research Updates*, *4*(1), 312–321. https://doi.org/10.53430/ijsru.2022.4.1.0138

Chave, J., Réjou-Méchain, M., Búrquez, A., Chidumayo, E., Colgan, M. S., Delitti, W. B. C., Duque, A., Eid, T., Fearnside, P. M., Goodman, R. C., Henry, M., Martínez-Yrízar, A., Mugasha, W. A., Muller-Landau, H. C., Mencuccini, M., Nelson, B. W., Ngomanda, A., Nogueira, E. M., Ortiz-Malavassi, E., … Vieilledent, G. (2014). Improved allometric models to estimate the aboveground biomass of tropical trees. *Global Change Biology*, *20*(10), 3177–3190. https://doi.org/10.1111/gcb.12629

Dronelink, I. (2022). *Dronelink Software*.

Duncanson, L., Rourke, O., & Dubayah, R. (2015). Small sample sizes yield biased allometric equations in temperate forests. *Scientific Reports*, *5*, 1–13. https://doi.org/10.1038/srep17153

Federman, A., Santana Quintero, M., Kretz, S., Gregg, J., Lengies, M., Ouimet, C., & Laliberte, J. (2017). UAV photogrammetric workflows: A best practice guideline. *International Archives of the Photogrammetry, Remote Sensing and Spatial Information Sciences (ISPRS Archives), XLII-2/W5*, 237–244. *https://doi.org/10.5194/isprs* archives-XLII-2-W5-237-2017

Harris, I., Osborn, T. J., Jones, P., & Lister, D. (2020). Version 4 of the CRU TS monthly high-resolution gridded multivariate climate dataset. *Scientific Data*, *7*(1), 1–18. https://doi.org/10.1038/s41597-020-0453-3

Hauser, L. T., Timmermans, J., van der Windt, N., Sil, Â. F., César de Sá, N., Soudzilovskaia, N. A., & van Bodegom, P. M. (2021). Explaining discrepancies between spectral and in-situ plant diversity in multispectral satellite earth observation. *Remote Sensing of Environment*, *265*. https://doi.org/10.1016/j.rse.2021.112684

Houborg, R., Fisher, J. B., & Skidmore, A. K. (2015). Advances in remote sensing of vegetation function and traits. *International Journal of Applied Earth Observation and Geoinformation*, *43*, 1–6. https://doi.org/10.1016/j.jag.2015.06.001

Houndonougbo, J. S. H., Kassa, B., Mensah, S., Salako, V. K., Glèlè Kakaï, R., & Assogbadjo, A. E. (2020). A global systematic review on conservation nd domestication of *Parkia biglobosa* (Jacq.) R. Br. ex G. Don, an indigenous fruit tree species in Sub-Saharan African traditional parklands: current knowledge and future directions. *Genetic Resources and Crop Evolution*, *67*(4), 1051–1066. https://doi.org/10.1007/s10722-020-00892-w

Komolafe, K., Olaleye, M. T., Huang, H. C., & Pacurari, M. (2024). Contemporary insights into the biological mechanisms of *Parkia biglobosa*. *International Journal of Environmental Research and Public Health*, *21*(4). https://doi.org/10.3390/ijerph21040394

Liu, B., Bu, W., & Zang, R. (2023). Improved allometric models to estimate the aboveground biomass of younger secondary tropical forests. *Global Ecology and Conservation*, *41*, e02359. https://doi.org/10.1016/j.gecco.2022.e02359

Ma, X., Mahecha, M. D., Migliavacca, M., van der Plas, F., Benavides, R., Ratcliffe, S., Kattge, J., Richter, R., Musavi, T., Baeten, L., Barnoaiea, I., Bohn, F. J., Bouriaud, O., Bussotti, F., Coppi, A., Domisch, T., Huth, A., Jaroszewicz, B., Joswig, J., … Wirth, C. (2019). Inferring plant functional diversity from space: the potential of Sentinel-2. *Remote Sensing of Environment*, *233*, 111368. https://doi.org/10.1016/j.rse.2019.111368

Madin, M. B., & Nelson, K. S. (2023). Effects of landscape simplicity on crop yield: A reanalysis of a global database. *PLoS ONE*, *18*(12 December), 1–16. https://doi.org/10.1371/journal.pone.0289799

Nandom Municipal Assembly. (2016). *Geology and soils*. Nandom District. https://www.nandomdistrict.gov.gh/2016/09/14/1-1-4-geology-and-soils/

Ounyambila, L., Anne, M. L., Benjamin, L., & Amadé, O. (2018). Influence of climate on fruit production of the yellow plum, *Ximenia americana*, in Burkina Faso, West Africa. *Journal of Horticulture and Forestry*, *10*(4), 36–42. https://doi.org/10.5897/jhf2017.0517

Panagiotidis, D., Abdollahnejad, A., Surový, P., & Chiteculo, V. (2017). Determining tree height and crown diameter from high-resolution UAV imagery. *International Journal of Remote Sensing*, *38*(8–10), 2392–2410. https://doi.org/10.1080/01431161.2016.1264028

Panda, S. S., Ames, D. P., & Panigrahi, S. (2010). Application of vegetation indices for agricultural crop yield prediction using neural network techniques. *Remote Sensing*, *2*(3), 673–696. https://doi.org/10.3390/rs2030673

Pasiecznik, N. (2022). *Parkia biglobosa (néré)*. CABI Compendium. https://doi.org/10.1079/cabicompendium.44162

Peters, R. H., Cloutier, S., Dubé, D., Evans, A., Hastings, P., Kaiser, H., Kohn, D., & Sarwer-Foner, B. (1988). The allometry of the weight of fruit on trees and shrubs in Barbados. *Oecologia*, *74*(4), 612–616. https://doi.org/10.1007/BF00380061

Poggio, L., De Sousa, L. M., Batjes, N. H., Heuvelink, G. B. M., Kempen, B., Ribeiro, E., & Rossiter, D. (2021). SoilGrids 2.0: Producing soil information for the globe with quantified spatial uncertainty. *Soil*, *7*(1), 217–240. https://doi.org/10.5194/soil-7-217-2021

Prado-Junior, J. A., Schiavini, I., Vale, V. S., Raymundo, D., Lopes, S. F., & Poorter, L. (2016). Functional traits shape size-dependent growth and mortality rates of dry forest tree species. *Journal of Plant Ecology*, *10*(6), rtw103. https://doi.org/10.1093/jpe/rtw103

Ribeiro da Luz, B., & Crowley, J. K. (2010). Identification of plant species by using high spatial and spectral resolution thermal infrared (8.0-13.5 μm) imagery. *Remote Sensing of Environment*, *114*(2), 404–413. https://doi.org/10.1016/j.rse.2009.09.019

Soil Research Institute. (1999). *Soil Map of Ghana*. Land Suitability Section, Soil Research Institute, CSIR, Ghana.

Thomson, E. R., Malhi, Y., Bartholomeus, H., Oliveras, I., Gvozdevaite, A., Peprah, T., Suomalainen, J., Quansah, J., Seidu, J., Adonteng, C., Abraham, A. J., Herold, M., Adu-Bredu, S., & Doughty, C. E. (2018). Mapping the leaf economic spectrum across West African tropical forests using UAV-acquired hyperspectral imagery. *Remote Sensing*, *10*(10). https://doi.org/10.3390/rs10101532

Xue, J., & Su, B. (2017). Significant remote sensing vegetation indices: A review of developments and applications. *Journal of Sensors, 2017*, 1–17. *https://doi.org/10.1155/2017/1353691*

Yiru, M., Ma, L., Zhang, Q., Huang, C., Yi, X., Chen, X., Hou, T., Lv, X., & Zhang, Z. (2022). Cotton yield estimation based on vegetation indices and texture features derived from RGB image. *Frontiers in Plant Science*, *13*, 1–17. https://doi.org/10.3389/fpls.2022.925986

Zhou, Q., & Melgar, J. C. (2020). Tree age influences nutrient partitioning among annually removed aboveground organs of peach. *HortScience*, *55*(4), 560–564. https://doi.org/10.21273/HORTSCI14731-19

CHAPTER SEVEN

GENERAL CONCLUSION, LIMITATIONS AND RECOMMENDATIONS

7.1 Conclusion

This study analyzed and evaluated machine learning models for general tree detection from images, investigated the use of computer vision, machine learning, and remote sensing techniques for characterizing *Adansonia digitata* (baobab) fruits captured with a smartphone, developed a deployable web application for automating *Adansonia digitata* fruits, and formulated a predictive modelling framework for estimating the pod yield of *Parkia biglobosa* using multi-source image and soil data. The findings are presented according to the study objectives.

Two main groups of models were identified: deep learning models, mainly convolutional neural networks (CNNs) and object detection frameworks, and traditional machine learning models such as random forest and support vector machines. Deep learning models consistently outperform traditional methods because they automatically learn relevant features from images, while traditional models rely on manual feature engineering. Among the deep learning approaches, modified Mask R-CNN architectures, such as ACE R-CNN, achieved very high performance (sensitivity ≈ 99.6%, specificity ≈ 99.3%, Bayesian AUC ≈ 98.6%). However, random forest models remained effective, particularly in situations with limited data and computational resources.

The study demonstrated that a computer vision system can detect, segment, and characterize *Adansonia digitata* fruits captured with a smartphone. Mask R-CNN achieved an accuracy of about 97.8% for detection and segmentation, and random forest was effective for estimating fruit physical properties such as volume, mass, and density. The relationship between mass and volume followed a quadratic form ($R^2 \approx 92\%$), indicating that fruits of similar size can have different densities. Bayesian statistical methods were used to classify fruits into size and quality classes based on posterior distributions. This allows for estimation of the proportion of fruits within each class and provides a practical basis for improving sorting, storage, pricing, and production planning.

To improve usability, a Shiny-based web application was developed to operationalize the detection and characterization workflow. The application allows users to upload images, visualize segmentation outputs, and obtain estimates of fruit properties and classification results in real time. Its interactive interface makes the results accessible and supports practical use in field conditions, ensuring that the research outputs can be applied beyond academic contexts.

The study further investigated the factors influencing *Parkia biglobosa* pod yield and showed that yield varies widely (4–218 kg per tree), with crown area ranging from 23.9 m^2 to 524.6 m^2. Yield differences were mainly driven by crown size, spectral reflectance, and soil characteristics. Models with interaction terms identified crown size, blue-band reflectance, and locality-specific factors as key predictors, while models without interaction terms identified crown size, near-infrared (NIR) reflectance, and soil pH (30–60 cm depth). In both cases, relationships followed an exponential form, indicating that small changes in these variables can lead to large differences in yield. These results confirm that integrating multi-source environmental and structural data enables reliable landscape-scale yield estimation under heterogeneous conditions.

The results demonstrate that low-cost and scalable technologies can significantly improve the efficiency and accuracy of tree resource assessment. Images captured with the smartphone enables effective fruit characterization, while drone and satellite data support landscape-level yield estimation. The integration of multiple data sources provides a comprehensive understanding of tree characteristics and productivity.

The study has important implications for food security, poverty reduction, biodiversity conservation, and climate resilience. Improved monitoring and yield estimation can support better resource management, enhance value chain development, and promote sustainable harvesting practices.

7.2 Limitations of the Study

Despite its contributions, the study has limitations that should be acknowledged. First, the analysis did not explicitly incorporate microclimate variables such as localized temperature variations, humidity, and rainfall distribution, which may influence fruit development and yield. Including such variables could improve model accuracy and provide a more comprehensive understanding of environmental drivers.

Second, the study relied on relatively limited sample sizes and spatial coverage, particularly for the fruit-level analysis. Although data augmentation and resampling techniques were used to enhance the dataset, larger and more diverse datasets would improve model generalization and robustness.

Third, while the use of smartphone imagery provides a low-cost and accessible solution, no perspective correction was applied to the images because all Adansonia digitata fruits were captured from a fixed distance away from camera. Varying distances may introduce variability that may affect detection and estimation accuracy under certain conditions.

Finally, the yield modelling approach focused primarily on structural and soil variables, with limited consideration of management practices, tree age, and genetic variability, which are also important determinants of productivity.

7.3 Recommendations

7.3.1 Methodological Recommendations

1. Computer vision and machine learning approaches should be adopted for indigenous tree assessment. Mask R-CNN is recommended for the detection and segmentation of *Adansonia digitata* fruits, while Random Forest is effective for estimating their mass, volume and density from morphological properties.
2. *Parkia biglobosa* pod yield should be estimated using tree-level models that integrate crown metrics, vegetation indices, soil properties, and locality factors. This approach enables reliable landscape-scale estimation.

7.3.2 Policy and Implementation

Government agencies, including the Ministry of Food and Agriculture (MoFA) and the Forestry Commission, should adopt digital inventory and yield-monitoring systems for indigenous tree species. These systems should be supported by:

- Community-level training on smartphone-based tools
- Periodic monitoring using UAV and satellite imagery
- Integration into national agricultural and forestry databases

This will enhance sustainable harvesting, improve market planning, and strengthen value chain development.

7.3.3 Future Research

Future studies should:

- Apply perspective correction techniques to correct errors introduced by varying the object-to-camera distance, for consistent image-based analysis in the computer vision model for detecting segmenting and characterizing *Adansonia digitata* Fruits.
- Investigate computational frameworks that incorporate microclimate and temporal variables, for estimating the pod yield of *Parkia biglobosa,* to improve model accuracy
- Expand datasets, for both *Adansonia digitata* fruits characterization and *Parkia biglobosa* pod yield estimation, across ecological zones to enhance generalizability.

APPENDICES

Appendix 1: Scientific Communications

i. Published Article

Dono, F. X., Baatuuwie, B. N., Abagale, F. K., & Sørensen, P. B. (2024). Application of computer vision and machine learning in morphological characterization of *Adansonia digitata* fruits. *Smart Agricultural Technology*, 9. *https://doi.org/10.1016/j.atech.2024.100528*

Smart Agricultural Technology 9 (2024) 100528

ELSEVIER

Contents lists available at ScienceDirect

Smart Agricultural Technology

journal homepage: www.journals.elsevier.com/smart-agricultural-technology

Application of computer vision and machine learning in morphological characterization of *Adansonia digitata* fruits

Franklin X. Dono [a,b,c,*], Bernard N. Baatuuwie [a,d], Felix K. Abagale [a], Peter Borgen Sørensen [e]

[a] West African Center for Water Irrigation and Sustainable Agriculture (WACWISA), University for Development Studies, P.O. Box TL 1882, Tamale, Ghana
[b] Department of Environmental Management and Sustainability, University for Development Studies, P.O. Box TL 1882, Tamale, Ghana
[c] Ghana Atomic Energy Commission (GAEC), Nuclear Power Institute (NPI), P.O. Box LG 80, Legon, Accra Ghana
[d] Department of Natural Resources and Geo-Information Sciences, Faculty of Natural Resources and Environment, University for Development Studies, P.O. Box TL 1882, Tamale, Ghana
[e] Institute of Ecoscience, Faculty of Technical Sciences, Aarhus University, C.F. Møllers Allé 4, 8000 Aarhus, Denmark

ARTICLE INFO

Keywords:
Baobab fruit
Computer vision
Machine learning
Image processing

ABSTRACT

Measuring fruit mass and volume is a time-consuming and tedious task that can affect production planning. This study developed a computer vision system to estimate the volume and mass of baobab fruits from single-view images captured from inexpensive and readily available cameras such as those in smartphones. The baobab fruits were collected from two study fields within the savanna ecological zone. Their images were captured, and subsequently, they were detected and segmented with over 97 % accuracy. The segmented images were binarized, and two-dimensional (2D) features such as the segmented area, centroid, bounding box, equivalent diameter, and major diameter were extracted from them. The volumes of the fruits were estimated from the 2D features using random forest, linear, polynomial, and radial support vector machine models. All the models achieved high goodness of fit; however, the random forest model delivered the best performance, with an R^2 value of 99.8 %. The relationship between mass and volume was a quadratic equation (mass = 38.23 + 0.25 × volume + 4.49e−05 × volume^2) and had an R^2 value of 92 %. Correlations were validated via plots and statistical tests, and credible intervals of point estimates were determined from the posterior distributions of their samples. This highlights the potential of artificial intelligence methods to be applied in a less constrained environmental setting for ecological research and agricultural management. Commercial companies producing baobab powder and seed oil should apply these models for effective production planning. To enhance the model, it would be beneficial to gain a better understanding of how climate gradients affect the morphological characteristics of baobab fruits.

ii. Published Article

Dono, F. X., Baatuuwie, B. N., Lykke, A. M., Abagale, F. K., & Sørensen, P. B. (2026). Estimating the yield of *Parkia biglobosa* fruits from field data and image-based predictive models. *Ecological Modelling*, 514. *https://doi.org/10.1016/j.ecolmodel.2026.111497*

Ecological Modelling 514 (2026) 111497

Contents lists available at ScienceDirect

Ecological Modelling

journal homepage: www.elsevier.com/locate/ecolmodel

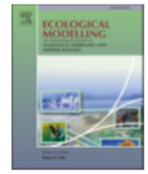

Estimating the yield of Parkia biglobosa fruits from field data and image-based predictive models

Franklin X. Dono [a,b,c,*], Bernard N. Baatuuwie [a,d], Anne Mette Lykke [e], Felix K. Abagale [a], Peter Borgen Sørensen [e]

[a] West African Center for Water Irrigation and Sustainable Agriculture (WACWISA), University for Development. Studies, Tamale, Ghana
[b] Department of Environmental Management and Sustainability, University for Development Studies, Tamale, Ghana
[c] Ghana Atomic Energy Commission (GAEC), Nuclear Power Institute (NPI), Legon, Accra-Ghana
[d] Department of Natural Resources and Geo-Information Sciences, Faculty of Natural Resources and Environment, University for Development. Studies, Tamale, Ghana
[e] Institute of Ecoscience, Faculty of Technical Sciences, Aarhus University, Aarhus, Denmark

A R T I C L E I N F O

Keywords:
Remote sensing
Yield estimation
Mathematical Modelling
Soil Properties
Morphology

A B S T R A C T

Accurate estimates of tropical tree fruit yields are essential for assessing individual tree productivity and landscape-scale applications. This study examines the productivity of *Parkia biglobosa* pods by integrating tree morphology, vegetation health indices from drone and satellite images, and soil properties into a mathematical model. The model evaluates interactions between these factors and their contribution to yield. Fruits were harvested from 105 mature trees within three study sites in the savanna ecological zones of Ghana and weighed. The crown radius of selected trees was measured in meters from mosaics derived from drone images in QGIS. Satellite images and data on the physical and chemical soil properties were obtained from the Norway International Climate and Forest Initiative (NICFI) and the Soil Reference and Information Centre (ISRIC), respectively. The yield was estimated by an exponential relationship involving the tree crown radius, average blue band reflectance from satellite images, and interaction with the locality. The model explained 75 % of the variation in yield. Excluding interaction terms, the best model estimated yield from tree crown radius, average near infrared reflectance of the crown, and soil pH at 30 – 60 cm depth. It indicated that crown radius, soil pH, Blue and Near-infrared spectral characteristics, along with variations in locality, such as soil and tree management practices, influenced the yield of *Parkia biglobosa*. Collectively, they explained 67.8 % of the variation in the yield. Policies to control tree stand undergrowth, prevent bushfires, promote less invasive harvesting techniques, and monitor soil nitrogen and pH levels are recommended for localities to enhance tree health and productivity.

iii. Scientific Oral Presentation

Topic: Application of Computer Vision and Machine Learning in Mprphological Characterization of *Adansonia digitata*
Authors: Dono, F. X., Baatuuwie, B. N., Abagale, F. K., & Sørensen, P. B. and Lykke, A.M
Event: 4th International Conference on Irrigation and Agricultural Development (IRAD), University for Development Studies (UDS), Ghana – 21^{st} -22^{nd} February 2024.

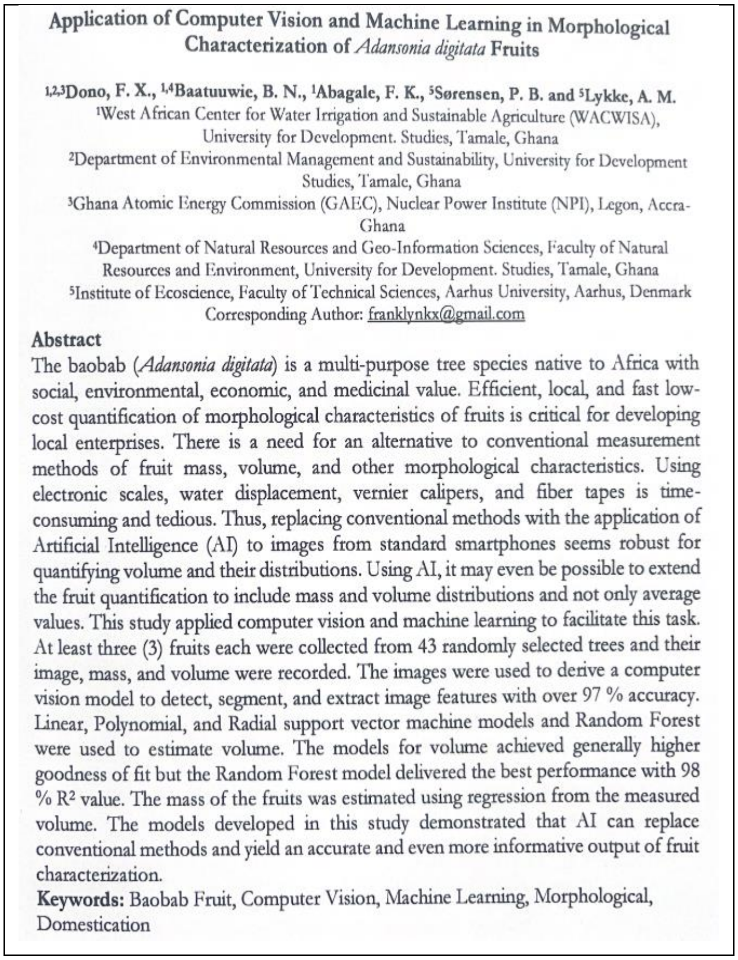

Application of Computer Vision and Machine Learning in Morphological Characterization of *Adansonia digitata* Fruits

[1,2,3]Dono, F. X., [1,4]Baatuuwie, B. N., [1]Abagale, F. K., [5]Sørensen, P. B. and [5]Lykke, A. M.
[1]West African Center for Water Irrigation and Sustainable Agriculture (WACWISA), University for Development. Studies, Tamale, Ghana
[2]Department of Environmental Management and Sustainability, University for Development Studies, Tamale, Ghana
[3]Ghana Atomic Energy Commission (GAEC), Nuclear Power Institute (NPI), Legon, Accra-Ghana
[4]Department of Natural Resources and Geo-Information Sciences, Faculty of Natural Resources and Environment, University for Development. Studies, Tamale, Ghana
[5]Institute of Ecoscience, Faculty of Technical Sciences, Aarhus University, Aarhus, Denmark
Corresponding Author: franklynkx@gmail.com

Abstract

The baobab (*Adansonia digitata*) is a multi-purpose tree species native to Africa with social, environmental, economic, and medicinal value. Efficient, local, and fast low-cost quantification of morphological characteristics of fruits is critical for developing local enterprises. There is a need for an alternative to conventional measurement methods of fruit mass, volume, and other morphological characteristics. Using electronic scales, water displacement, vernier calipers, and fiber tapes is time-consuming and tedious. Thus, replacing conventional methods with the application of Artificial Intelligence (AI) to images from standard smartphones seems robust for quantifying volume and their distributions. Using AI, it may even be possible to extend the fruit quantification to include mass and volume distributions and not only average values. This study applied computer vision and machine learning to facilitate this task. At least three (3) fruits each were collected from 43 randomly selected trees and their image, mass, and volume were recorded. The images were used to derive a computer vision model to detect, segment, and extract image features with over 97 % accuracy. Linear, Polynomial, and Radial support vector machine models and Random Forest were used to estimate volume. The models for volume achieved generally higher goodness of fit but the Random Forest model delivered the best performance with 98 % R^2 value. The mass of the fruits was estimated using regression from the measured volume. The models developed in this study demonstrated that AI can replace conventional methods and yield an accurate and even more informative output of fruit characterization.

Keywords: Baobab Fruit, Computer Vision, Machine Learning, Morphological, Domestication

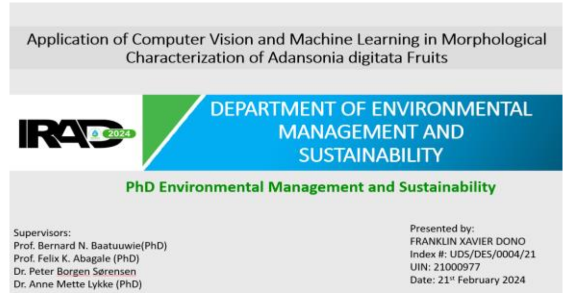

Appendix 2: Summary of Tree Species Studies in Articles

Order	Family	Reference	Model Architecture and Backbone	Species list
Alismatales	Hydrocharitaceae	Chabot *et al.*, 2018	Random Forest	*Stratiotes aloides*
Arecales	Arecaceae	Ferreira *et al.*, 2020	DeepLabV3+/IRU Encoder/ResNet-18	*Attalea butyracea, Euterpe precatoria, Iriartea deltoidei*
		Miyoshi *et al.*, 2020	Random Forest	*Syagrus roman*
		Ochoa and Guo, 2019	Modified YOLO	*Cocos nucifera (Coconut)*
Brassicales	Caricaceae	Ochoa and Guo,	Modified YOLO	*Carica papaya (Papaya)*

Order	Family	Reference	Model Architecture and Backbone	Species list
		2019		
Ericales	Lecythidaceae	Ferreira *et al.*, 2021	DeepLabV3+/IRU Encoder/ResNet-18	*Bertholletia excelsa*
Ericales	Theaceae	Li *et al.*, 2022	Mask R-CNN/ResNet-50 ACE R-CNN/ACNet	*Camellia oleifera Abel*
Fabales	Fabaceae	Li *et al.*, 2022	Mask R-CNN/ResNet-50 ACE R-CNN/ACNet	*Acacia melanoxylon*
		Miyoshi *et al.*, 2020	Random Forest	*Apuleia leiocarpa,* *Copaifera langsdorffii,* *Hymenaea courbaril,* *Inga vera,*
		Moura *et al.*, 2021	Faster R-CNN/InceptionV2	*Pterodon pubescens,* *Anadenanthera* sp., *Bauhinia acreana*
		Torres *et al.*, 2020	FCN-CRF /U-Net /SegNet /FC-DenseNet DeepLabV3+ /Xception /MobileNetV2	*Hymenaea courbaril,*
Fagales	Betulaceae	Li *et al.*, 2022	Mask R-CNN/ResNet-50 ACE R-CNN/ACNet	*Betula alnoides Hamilt*
		Mayra *et al.*, 2021	Random Forest LightGBM SVM ANN 3D-CNN	*Birch (Betula pubescens and Betula pendula)*
Fagales	Fagaceae	Li *et al.*, 2022	Mask R-CNN/ResNet-50 ACE R-CNN/ACNet	*Castanopsis hystrix* Miq.
Lamiales	Bignoniaceae	Moura *et al.*, 2021	Faster R-CNN/InceptionV2	*Handroanthus serratifolius*
Laurales	Lauraceae	Miyoshi *et al.*, 2020	Random Forest	*Endlicheria paniculata*
Magnoliales	Magnoliaceae	Li *et al.*, 2022	Mask R-CNN/ResNet-50	*Michelia macclurei Dandy*

Order	**Family**	**Reference**	**Model Architecture and Backbone**	**Species list**
			ACE R-CNN/ACNet	
Malpighiales	Salicaceae	Mayra *et al.*, 2021	Random Forest LightGBM SVM ANN 3D-CNN	*Populus tremula* (European aspen)
Myrtales	Myrtaceae	Li *et al.*, 2022	Mask R-CNN/ResNet-50 ACE R-CNN/ACNet	*Eucalyptus urophyllus*
Pinales	Pinaceae	Li *et al.*, 2022	Mask R-CNN/ResNet-50 ACE R-CNN/ACNet	*Pinus elliottii*
		Mayra *et al.*, 2021	Random Forest LightGBM SVM ANN 3D-CNN	*Picea abies* (Norway spruce) *Pinus sylvestris* (Scots pine)
		Ouattara *et al.*, 2020	Faster R-CNN/InceptionV2	*Picea* spp. (young spruce)
Poales	Poaceae	Ochoa and Guo, 2019	Modified YOLO	*Mangifera Indica* (Mango)
Rosales	Urticaceae	Moura *et al.*, 2021	Faster R-CNN/InceptionV2	*Cecropia juranyiana*
Sapindales	Anacardiaceae	Moura *et al.*, 2021	Faster R-CNN/InceptionV2	*Anacardium occidentale*
Sapindales	Rutaceae	Miyoshi *et al.*, 2020	Random Forest	*Helietta apiculate*
Unknown	Unknown	Chabot *et al.*, 2018	Random Forest	*Floating Leaved Vegetation, Other Emergent Vegetation, Other submerged features, Other submerged vegetation,*
		Dong *et al.*, 2018	Cascade Neural Network	Palm, small seedlings, red maples, or longan trees
		Li *et al.*, 2022	Mask R-CNN/ResNet-50 ACE R-CNN/ACNet	*Soft Broads*
Zingiberales	Musaceae	Ochoa and Guo, 2019	Modified YOLO	*Musa* sp. (Banana)

Appendix 3: Coefficients Table for Interactive-Form Models.

The table summarizes the coefficients of models for predicting yield of *Parkia biglobosa* pods with interaction terms. Soil depth intervals are represented as [A]: 0–5 cm, [B]: 5–15 cm, [C]: 15–30 cm, [D]: 30–60 cm, [E]: 60–100 cm, and [F]: 100–200 cm.

Term	Estimate	Std.	P. Value	Significance
Model 3.1: ln(Yield) ~ ln(r) + Sand[D] * Location				
(Intercept)	-0.581	0.864	0.503	
ln(r)	1.026	0.210	0.000	***
Sand[D]	0.005	0.002	0.013	*
LocationNandom	4.824	6.737	0.476	
LocationNavrongo	-13.572	4.310	0.002	**
Sand[D]: LocationNandom	-0.009	0.014	0.540	
Sand[D]: LocationNavrongo	0.031	0.010	0.001	**
Model 3.2: ln(Yield) ~ ln(r) + B.x * Location				
(Intercept)	1.392	0.475	0.004	**
ln(r)	1.198	0.215	0.000	***
B.x	-0.004	0.004	0.330	
LocationNandom	0.522	0.697	0.456	
LocationNavrongo	-2.529	0.982	0.012	*
B.x: LocationNandom	0.011	0.015	0.453	
B.x: LocationNavrongo	0.050	0.014	0.001	**
Model 3.3: ln(Yield) ~ ln(r) + B.y * Location				
(Intercept)	5.322	1.584	0.001	**
ln(r)	1.037	0.215	0.000	***
B.y	-0.008	0.003	0.009	**
LocationNandom	-2.857	1.793	0.114	
LocationNavrongo	-5.975	1.740	0.001	**
B.y: LocationNandom	0.009	0.004	0.024	*
B.y: LocationNavrongo	0.013	0.003	0.000	***
Model 3.4: ln(Yield) ~ ln(r) + NGRDI.x + Sand[D] * Location				

Term	Estimate	Std.	P. Value	Significance
(Intercept)	-0.881	0.888	0.324	
ln(r)	1.086	0.214	0.000	***
NGRDI.x	-2.485	1.811	0.173	
Sand[D]	0.006	0.002	0.005	**
LocationNandom	4.942	6.707	0.463	
LocationNavrongo	-13.654	4.291	0.002	**
Sand[D]: LocationNandom	-0.010	0.014	0.497	
Sand[D]: LocationNavrongo	0.031	0.010	0.001	**
Model: ln(Yield) ~ ln(r) + N + Nitrogen[E] * Location				
(Intercept)	-4.672	1.744	0.009	**
ln(r)	0.907	0.213	0.000	***
N	0.001	0.000	0.113	
Nitrogen[E]	0.110	0.033	0.001	**
LocationNandom	5.156	1.798	0.005	**
LocationNavrongo	11.275	2.389	0.000	***
Nitrogen[E]: LocationNandom	-0.100	0.043	0.024	*
Nitrogen[E]: LocationNavrongo	-0.327	0.081	0.000	***
Model 3.5: ln(Yield) ~ ln(r) + CI.x + N + Nitrogen[E] * Location				
(Intercept)	-6.049	1.801	0.001	**
ln(r)	0.946	0.209	0.000	***
CI.x	-2.420	1.025	0.020	*
N	0.001	0.000	0.014	*
Nitrogen[E]	0.159	0.039	0.000	***
LocationNandom	6.902	1.906	0.000	***
LocationNavrongo	11.207	2.335	0.000	***
Nitrogen[E]: LocationNandom	-0.149	0.047	0.002	**
Nitrogen[E]: LocationNavrongo	-0.310	0.080	0.000	***

Where p. value < 0.001: ***, p. value < 0.01: **, p. value < 0.05: *, p. value < 0.1: .

Appendix 4: Coefficient Table for Basic-Form Models.

The table summarizes the coefficients of models for predicting yield of *Parkia biglobosa* pods without interaction terms. Soil depth intervals are represented as [A]: 0–5 cm, [B]: 5–15 cm, [C]: 15–30 cm, [D]: 30–60 cm, [E]: 60–100 cm, and [F]: 100–200 cm.

Term	Estimate	Std. Error	P.Value	Significance
Model 4.1: ln(Yield) ~ ln(r) + Location				
(Intercept)	-1.552	1.182	0.209	
ln(r)	2.898	0.674	0.001	***
LocationNandom	0.884	0.275	0.006	**
LocationNavrongo	1.082	0.359	0.009	**
Model 4.2: ln(Yield) ~ ln(r) + CEC[F] + Location				
(Intercept)	4.148	1.032	0.000	***
ln(r)	1.166	0.211	0.000	***
CEC[F]	-0.021	0.007	0.002	**
LocationNandom	0.721	0.171	0.000	***
LocationNavrongo	0.836	0.161	0.000	***
Model 4.3: ln(Yield) ~ ln(r) + NGRDI.x + CEC[F] + Location				
(Intercept)	5.035	1.179	0.000	***
ln(r)	1.228	0.213	0.000	***
NGRDI.x	-2.906	1.912	0.132	
CEC[F]	-0.026	0.007	0.001	**
LocationNandom	0.369	0.287	0.202	
LocationNavrongo	0.714	0.179	0.000	***
Model 4.4: ln(Yield) ~ ln(r) + N + pH[D] + Location				
(Intercept)	-15.699	4.205	0.000	***
ln(r)	0.989	0.215	0.000	***
N	0.001	0.000	0.016	*
pH[D]	0.242	0.070	0.001	**
LocationNandom	0.153	0.351	0.664	
LocationNavrongo	-0.488	0.503	0.334	

Term	Estimate	Std. Error	P.Value	Significance
Model 4.5: ln(Yield) ~ ln(r) + NGRDI.x + N + CEC[F] + Location				
(Intercept)	2.279	1.737	0.193	
ln(r)	1.101	0.218	0.000	***
NGRDI.x	-3.712	1.916	0.056	.
N	0.001	0.000	0.036	*
CEC[F]	-0.023	0.007	0.002	**
LocationNandom	0.501	0.289	0.086	.
LocationNavrongo	0.879	0.192	0.000	***

Where p. value < 0.001: ***, p. value < 0.01: **, p. value < 0.05: *, p. value < 0.1: .

Appendix 5: Code

The R Shiny application code

```
library(shiny)
library(reticulate)
library(rstan)
library(ggplot2)
library(caret)


ui <- fluidPage(
    titlePanel("BaoIMG"),

    tags$div(
        h4("Image Processing & Computer Vision", style = "color: #666; font-style: italic; mar
gin-bottom: -10px; margin-bottom: 20px;")
    ),
    sidebarLayout(
        sidebarPanel(
            fileInput("file1", "Choose image file(s)",
                multiple = TRUE,
                accept = c("image/jpeg",
                    "image/png",
                    "image/JPG",
                    "image/TIFF",
                    "image/jpg")),
            radioButtons("analysisType", "Select Analysis Type:",
                choices = c("Model Evaluation", "Feature Extraction"),
```

```
                selected = "Model Evaluation"),  # Set default selection
          #actionButton("runAnalysisButton", "Run Analysis")

          fluidRow(
               column(width = 6,
                    align = "center",
                    style = "max-width: 100%; max-height: 100%;",
                    actionButton("runAnalysisButton", "Run Analysis")
               ),
               column(width = 6,
                    align = "center",
                    style = "max-width: 100%; max-height: 100%;",
                    downloadButton("saveOutputButton", "Save CSV")
               )
          )
     ),

     mainPanel(
          fluidRow(
               column(width = 6,
                    align = "center",
                    style = "max-width: 100%; max-height: 100%; overflow: auto;",
                    imageOutput("test_image")
               ),
               column(width = 6,
                    align = "center",
                    style = "max-width: 100%; max-height: 100%; overflow: auto;",
                    imageOutput("output_image")
               )
          )
     )
),
titlePanel("BaoQUANT"),

tags$div(
     h4("Mass, Volume, Density Estimation", style = "color: #666; font-style: italic; margin
-bottom: -10px; margin-bottom: 20px;")
),
sidebarLayout(
     sidebarPanel(
          fileInput("file", "Choose CSV file",
                accept = c("text/csv",
                       "text/comma-separated-values,text/plain",
                       ".csv")),
          checkboxInput("loadFromBaoIMG", "Load CSV from BaoIMG", value = TRUE
```

```
),
            tags$hr(),
            helpText("Select a CSV file with appropriate data."),
            selectInput("model_type", "Choose Model Type",
                  choices = c("Volume", "Mass", "Density")),
            actionButton("run_button", "Run Model")
        ),

        mainPanel(
            plotOutput("plot"),
            tableOutput("table")
        )
    )

)

server <- function(input, output) {

#     reticulate::install_python(version = '3.10')
#     #virtualenv_dir <- Sys.getenv('VIRTUALENV_NAME')
#     virtualenv_dir <- 'boafruit_env'
#
#     #python_path <- Sys.getenv('PYTHON_PATH')
#
#     if (!reticulate::virtualenv_exists(virtualenv_dir)) {
#          reticulate::virtualenv_create(envname = virtualenv_dir, python = python3)
#     }

#     reticulate::virtualenv_install(virtualenv_dir, packages = packages, ignore_installed = FA
LSE)
#     reticulate::use_virtualenv(virtualenv_dir, required = TRUE)
#
#     print(Sys.which('python'))
#     print(Sys.which('python3'))
#
#     reticulate::py_run_string('
# import sys
# import os
# print(os.environ["PYTHONPATH"])
# print(sys.path)
# ')
    reticulate::source_python('baobab_cv.py')

    destination_dir_path <- file.path(tempdir(), "baobab")
    if (!file.exists(destination_dir_path)) {
```

```
            dir.create(destination_dir_path, recursive = TRUE)
      }
      observeEvent(input$file1, {
            file.remove(list.files(destination_dir_path, full.names = TRUE))
      })

      observeEvent(input$runAnalysisButton, {
            #print(tempdir())
            #unlink(tempdir(), recursive = TRUE)
            if (input$analysisType == "Model Evaluation") {
                  if (dim(input$file1)[1] <= 1) {
                        image_path <- input$file1$datapath
                        if (file.exists(image_path)) {
                              output$test_image <- renderImage({
                                    list(src = image_path, contenType = "image/jpeg")
                              }, deleteFile = FALSE)
                        }
                        py$noname <- image_path
                        reticulate::py_run_string('singlePredict(noname)')
                        output$output_image <- renderImage({
                              outpUt_image_file <- py$output_image_file
                              list(src = output_image_file, contenType = "image/jpeg")  # Set width t
o 100% of container
                        },
                        deleteFile = FALSE)
                  }
                  else{
                        showNotification("Evaluate model performance on One image at a time")
                        return()
                  }
            }
            else{
                  for (i in seq_along(input$file1$name)) {
                        destination_file_path <- file.path(destination_dir_path, input$file1$name[i])
                        file.copy(input$file1$datapath[i], destination_file_path)
                        if (!file.exists(destination_file_path)){
                              print("FILE NOT FOUND")
                        }
                  }

                  showNotification("Feature extraction:....Busy")
                  py$input_images_directory <- destination_dir_path
                  reticulate::py_run_string('output_csv_path = featureExtraction(input_images_dir
ectory)')
                  showNotification("Feature extraction:....Finished")
```

```
        }
    })

    # Event handler for the download button
    output$saveOutputButton <- downloadHandler(
        filename = function() {
            paste("output_objects.csv")
        },
        content = function(file) {
            # Save the output CSV file to the specified path
            file.copy("temp/output_objects.csv", file)
        }
    )

    observeEvent(input$run_button, {
        #req(input$file)

        if (input$loadFromBaoIMG && file.exists("temp/output_objects.csv")) {
            original_single <- read.csv("temp/output_objects.csv")
        }
        else{
            # Read data

            if (!is.null(input$file)){
                original_single <- read.csv(input$file$datapath)
            }
            else{
                showNotification("No CSV file found, Run BaoIMG Feature Extraction or
Upload CSV File")
                return()
            }
        }

        # Determine model type
        model <- switch(input$model_type,
                "Volume" = "volume",
                "Mass" = "mass",
                "Density" = "density")

        # Run the appropriate model
        result <- switch(model,
                 "volume" = run_volume_model(original_single),
                 "mass" = run_mass_model(original_single),
                 "density" = run_density_model(original_single))
```

```
        output$plot <- renderPlot({
            if (!is.null(result)) {
                result$plot  # Render ggplot
            } else {
                return(NULL)
            }
        })
        output$table <- renderTable({
            if (!is.null(result)) {

                # Extracting and summarizing the fit object
                summary_df <- summary(result$fit)$summary
                summary_df <- round(summary_df,2)

                # Include row titles as a separate column
                summary_df <- cbind(" " = rownames(summary_df), summary_df)
                summary_df

                #print(result$fit)
            } else {
                return(NULL)
            }
        })
    })
}
# Define functions for running models
run_volume_model <- function(original_single) {

    # Rest of your function code
    # Load the trained volume model using the load function
    load("r_ml/volume_model_svmPoly.RData")
    load("r_ml/volume_model_svmLinear.RData")
    load("r_ml/volume_model_svmRadial.RData")
    load("r_ml/volume_model_rf.RData")



    # Read data
    #original_single <- read.csv("temp/output_objects.csv")
    #original_single <- original_single[original_single$Volume1 != 0 &
    #                                   original_single$Count_expected == 1 &
    #                                   original_single$Transformation == "", ]

    original_single <- original_single[order(original_single$File.Name),]
    adan <- original_single
    #adan<- adan[
```

```
#       adan$Area >= 20000 &
#             adan$Area <= 230000 &
#             adan$Field == "nav" &
#             adan$Class.Name != "Unknown",

# FUNCTIONS
# Function to extract centroid coordinates
extract_centroid <- function(centroid_str) {
      coordinates <- as.numeric(unlist(strsplit(gsub("[\\(\\)]", "", centroid_str), ",")))

      # Check if there are at least 3 elements in coordinates
      if (length(coordinates) >= 3) {
            return(list(centroid_id = coordinates[1], centroid_x = coordinates[2], centroid_y
= coordinates[3]))
      } else {
            return(list(centroid_id = NA, centroid_x = NA, centroid_y = NA))  # Return NA
for all values if there are not enough elements
      }
}

# Function to extract bounding box coordinates
extract_bounding_box <- function(bbox_str) {
      coordinates <- as.numeric(unlist(strsplit(gsub("[\\(\\)]", "", bbox_str), ",")))

      # Check if there are at least 6 elements in coordinates
      if (length(coordinates) >= 6) {
            return(list(
                  #bb_id_1 = coordinates[1],
                  bb_x_min = coordinates[2],
                  bb_y_min = coordinates[3],
                  #bb_id_2 = coordinates[4],
                  bb_y_max = coordinates[5],
                  bb_x_min = coordinates[6]
            ))
      } else {
            return(list(
                  #bb_id_1 = NA, bb_id_2 = NA,
                  bb_x_min = NA, bb_y_min = NA,
                  bb_x_max = NA, bb_y_max = NA
            ))  # Return NA for all values if there are not enough elements
      }
}

# Function to compute area
compute_area <- function(tuple_str) {
```

```
            bounding_box <- as.numeric(unlist(strsplit(gsub("[\\(\\)]", "", tuple_str), ",")))

            # Check if there are at least 6 elements in bounding_box
            if (length(bounding_box) >= 6) {
                  height <- bounding_box[5] - bounding_box[2]
                  width <- bounding_box[6] - bounding_box[3]
                  area <- height * width
                  return(list(bb_height = height, bb_width = width, bb_area = area))
            } else {
                  return(list(bb_height = NA, bb_width = NA, bb_area = NA))  # Return NA for al
l values if there are not enough elements
            }
      }

       # Apply the function and create a new data frame for centroid coordinates
      centroid_df <- do.call(rbind, lapply(adan$Centroid, extract_centroid))
      colnames(centroid_df) <- c("centroid_id", "centroid_x", "centroid_y")

      # Merge the new data frame with the original data frame
      adan <- cbind(adan, centroid_df)

      # Apply the function and create a new data frame for bounding box coordinates
      bbox_df <- do.call(rbind, lapply(adan$BoundingBox, extract_bounding_box))
      colnames(bbox_df) <- c("bb_x_min", "bb_y_min", "bb_x_max", "bb_y_max")

      # Merge the new data frame with the original data frame
      adan <- cbind(adan, bbox_df)


      # Apply the function and create a new data frame for height, width, and area
      cbox_df <- do.call(rbind, lapply(adan$BoundingBox, compute_area))
      colnames(cbox_df) <- c("bb_height", "bb_width", "bb_area")

       # Merge the new data frame with the original data frame
      adan <- cbind(adan, cbox_df)
      adan <- adan[ , -c(1,2,3,5,6,7,10,11)]

        # Columns to convert
      columns_to_convert <- c('centroid_x',
                        'centroid_y',
                        'bb_x_min',
                        'bb_x_max',
                        'bb_y_min',
                        'bb_y_max',
                        'bb_area',
```

```
                    'bb_height',
                    'bb_width'
    )

    # Convert each column to numeric
    adan[, columns_to_convert] <- lapply(adan[, columns_to_convert], function(x) as.numeri
c(unlist(x)))


    # Volume Estimate
    start_time <- Sys.time()
    svmPoly_adan_v <- predict(volume_model_svmPoly, adan)
    end_time <- Sys.time()
    svmPoly_v_time_elapsed <- end_time - start_time

    start_time <- Sys.time()
    svmLinear_adan_v <- predict(volume_model_svmLinear, adan)
    end_time <- Sys.time()
    svmLinear_v_time_elapsed <- end_time - start_time

    start_time <- Sys.time()
    svmRadial_adan_v <- predict(volume_model_svmRadial, adan)
    end_time <- Sys.time()
    svmRadial_v_time_elapsed <- end_time - start_time

    start_time <- Sys.time()
    RF_adan_v <- predict(volume_model_rf, adan)
    end_time <- Sys.time()
    RF_v_time_elapsed <- end_time - start_time


    # Creating a data frame to tabulate time elapsed
    time_elapsed_data <- data.frame(
        Model = c("SVM Poly (Volume)", "SVM Linear (Volume)", "SVM Radial (Volume)",
"Random Forest (Volume)"),
        TimeElapsed = c(
            as.numeric(svmPoly_v_time_elapsed),
            as.numeric(svmLinear_v_time_elapsed),
            as.numeric(svmRadial_v_time_elapsed),
            as.numeric(RF_v_time_elapsed)
        )
    )

    # Save the data frame as a CSV file
    write.csv(time_elapsed_data, "temp/test_time_elapsed_data_373.csv", row.names = FALS
```

```
E)

    # Print the table
    print(time_elapsed_data)

    volume_predictions <- cbind(svmPoly_adan_v, svmLinear_adan_v,svmRadial_adan_v, RF
_adan_v)

    act_pred_vol <- cbind(original_single$File.Name, volume_predictions)
    colnames(act_pred_vol) <- c("sample_id", "svmPoly", "svmLinear", "svmRadial", "Rando
m Forest")

    write.csv(act_pred_vol, "temp/test_model_predicted_volumes_nav.csv", row.names = FAL
SE)




    # Load required libraries
    #library(rstan)
    #library(ggplot2)

    # Define the Stan model with updated prior distributions for mu and sigma
    stan_model_volume <- "
    data {
     int<lower=0> N;       // Number of observations
     vector[N] y;          // Data vector
    }

    parameters {
     real<lower=0> mu; // mu parameter of normal distribution
     real<lower=0> sigma; // sigma parameter normal distribution
    }

    model {
     // Prior distributions for mu and sigma
     mu ~ normal(682.39952, 26.23669); // mu parameter prior
     sigma ~ normal(337.66061, 18.61232); // sigma parameter prior

     // Likelihood
     y ~ normal(mu, sigma); // Likelihood function
    }

    generated quantities {
      real prob_below_thresh;  // Probability of posterior below threshold
```

```
    real prob_within_thresh; // Probability of posterior within threshold
    real prob_above_thresh;  // Probability of posterior above threshold

    // Calculate probabilities
    prob_below_thresh = normal_cdf(682 - 2*24, mu, sigma/sqrt(166));         // Below thresho
ld
    prob_within_thresh = normal_cdf(682 + 2*24, mu, sigma/sqrt(166)) - normal_cdf(682 - 2*
24, mu, sigma/sqrt(166)); // Within threshold
    prob_above_thresh = 1 - normal_cdf(682 + 2*24, mu, sigma/sqrt(166));       // Above thres
hold
  }
  "

  # Load data
  set.seed(123)

  y <- read.csv("temp/test_model_predicted_volumes_nav.csv")

  y <- y$svmPoly #Random.Forest #
  N <- length(y)

  # Prepare data list
  data_list <- list(N = N, y = y)

  # Compile the Stan model
  #compiled_model <- stan_model(model_code = stan_model_volume)

  # Save the compiled Stan model to a file
  #saveRDS(compiled_model, file = "stan/compiled_model_volume.stan")

  # Load the compiled Stan model from the file
  compiled_model <- readRDS("stan/compiled_model_volume.stan")

  # Fit the model to the data
  fit <- sampling(compiled_model, data = data_list, chains = 4)

  # Extract posterior samples
  posterior_samples <- extract(fit)

  min_value <- min(682 - 4*26, mean(posterior_samples$mu) - 4*26)
  max_value <- max(682 + 4*26, mean(posterior_samples$mu) + 4*26)

  # Generate prior distribution
  x <- seq(min_value, max_value, length.out = 100)
  prior <- dnorm(x, mean = 682.39952, sd = 26.23669)
```

```
    prior <- prior / max(prior)

    # Generate posterior distribution
    posterior <- dnorm(x, mean = mean(posterior_samples$mu), sd = mean(posterior_samples
$sigma)/sqrt(166))
    posterior <- posterior / max(posterior)

    # Generate likelihood distribution
    likelihood_unnormalized <- prior * posterior
    likelihood <- likelihood_unnormalized / max(likelihood_unnormalized)

    # Plot using ggplot2
    df <- data.frame(x = x, prior = prior, posterior = posterior, likelihood = likelihood)

    # Plot using ggplot2 with thresholds
    vp <- ggplot(df, aes(x)) +
        geom_line(aes(y = prior, color = "Prior")) +
        geom_line(aes(y = posterior, color = "Posterior")) +
        #geom_line(aes(y = likelihood, color = Likelihood)) +
        geom_vline(xintercept = c(682 - 2*24, 682 + 2*24),
                linetype = "dashed", color = "red") +
        labs(title = "",
            x = "(b)   mu volume (cm³)", y = "Density") +
        scale_color_manual(name = "Distribution",
                    values = c(Prior = "red", Posterior = "blue", Likelihood = "green")) +
        theme_minimal()

    vp
    vp.fit <- fit
    # posterior_samples$prob_below_thresh+posterior_samples$prob_within_thresh+posterio
r_samples$prob_above_thresh

    # After all computations are done, prepare the result object
    result <- list(data = df, x = df$volume, y = df$predicted_volume, fit = vp.fit, plot = vp)

    return(result)
}


run_mass_model <- function(original_single) {
    # Your mass model code here

    # Load the trained mass model using the load function
    load( "r_ml/weight_model_svmPoly.RData")
    load("r_ml/weight_model_svmLinear.RData")
```

```
load("r_ml/weight_model_svmRadial.RData")
load("r_ml/weight_model_rf.RData")



# Read data
#original_single <- read.csv("temp/output_objects.csv")
#original_single <- original_single[original_single$Volume1 != 0 &
#                                   original_single$Count_expected == 1 &
#                                   original_single$Transformation == "", ]

original_single <- original_single[order(original_single$File.Name),]


adan <- original_single

#adan<- adan[
#      adan$Area >= 20000 &
#            adan$Area <= 230000 &
#            adan$Field == "nav" &
#            adan$Class.Name != "Unknown",
#
#]


# FUNCTIONS
# Function to extract centroid coordinates
extract_centroid <- function(centroid_str) {
      coordinates <- as.numeric(unlist(strsplit(gsub("[\\(\\)]", "", centroid_str), ",")))

      # Check if there are at least 3 elements in coordinates
      if (length(coordinates) >= 3) {
            return(list(centroid_id = coordinates[1], centroid_x = coordinates[2], centroid_y
= coordinates[3]))
      } else {
            return(list(centroid_id = NA, centroid_x = NA, centroid_y = NA))  # Return NA
for all values if there are not enough elements
      }
}


# Function to extract bounding box coordinates
extract_bounding_box <- function(bbox_str) {
      coordinates <- as.numeric(unlist(strsplit(gsub("[\\(\\)]", "", bbox_str), ",")))
```

```
        # Check if there are at least 6 elements in coordinates
        if (length(coordinates) >= 6) {
            return(list(
                #bb_id_1 = coordinates[1],
                bb_x_min = coordinates[2],
                bb_y_min = coordinates[3],
                #bb_id_2 = coordinates[4],
                bb_y_max = coordinates[5],
                bb_x_min = coordinates[6]
            ))
        } else {
            return(list(
                #bb_id_1 = NA, bb_id_2 = NA,
                bb_x_min = NA, bb_y_min = NA,
                bb_x_max = NA, bb_y_max = NA
            ))  # Return NA for all values if there are not enough elements
        }
    }


    # Function to compute area
    compute_area <- function(tuple_str) {
        bounding_box <- as.numeric(unlist(strsplit(gsub("[\\(\\)]", "", tuple_str), ",")))

        # Check if there are at least 6 elements in bounding_box
        if (length(bounding_box) >= 6) {
            height <- bounding_box[5] - bounding_box[2]
            width <- bounding_box[6] - bounding_box[3]
            area <- height * width
            return(list(bb_height = height, bb_width = width, bb_area = area))
        } else {
            return(list(bb_height = NA, bb_width = NA, bb_area = NA))  # Return NA for al
l values if there are not enough elements
        }
    }



    # Apply the function and create a new data frame for centroid coordinates
    centroid_df <- do.call(rbind, lapply(adan$Centroid, extract_centroid))
    colnames(centroid_df) <- c("centroid_id", "centroid_x", "centroid_y")

    # Merge the new data frame with the original data frame
    adan <- cbind(adan, centroid_df)
```

```r
# Apply the function and create a new data frame for bounding box coordinates
bbox_df <- do.call(rbind, lapply(adan$BoundingBox, extract_bounding_box))
colnames(bbox_df) <- c("bb_x_min", "bb_y_min", "bb_x_max", "bb_y_max")

# Merge the new data frame with the original data frame
adan <- cbind(adan, bbox_df)


# Apply the function and create a new data frame for height, width, and area
cbox_df <- do.call(rbind, lapply(adan$BoundingBox, compute_area))
colnames(cbox_df) <- c("bb_height", "bb_width", "bb_area")


# Merge the new data frame with the original data frame
adan <- cbind(adan, cbox_df)


adan <- adan[ , -c(1,2,3,5,6,7,10,11)]




# Columns to convert
columns_to_convert <- c('centroid_x',
                        'centroid_y',
                        'bb_x_min',
                        'bb_x_max',
                        'bb_y_min',
                        'bb_y_max',
                        'bb_area',
                        'bb_height',
                        'bb_width'
)

# Convert each column to numeric
adan[, columns_to_convert] <- lapply(adan[, columns_to_convert], function(x) as.numeri
c(unlist(x)))

# Mass Estimate
start_time <- Sys.time()
svmPoly_adan_m <- predict(weight_model_svmPoly, adan)
end_time <- Sys.time()
svmPoly_m_time_elapsed <- end_time - start_time
```

```
start_time <- Sys.time()
svmLinear_adan_m <- predict(weight_model_svmLinear, adan)
end_time <- Sys.time()
svmLinear_m_time_elapsed <- end_time - start_time

start_time <- Sys.time()
svmRadial_adan_m <- predict(weight_model_svmRadial, adan)
end_time <- Sys.time()
svmRadial_m_time_elapsed <- end_time - start_time

start_time <- Sys.time()
RF_adan_m <- predict(weight_model_rf, adan)
end_time <- Sys.time()
RF_m_time_elapsed <- end_time - start_time

# Creating a data frame to tabulate time elapsed
time_elapsed_data_m <- data.frame(
	Model = c("SVM Poly (Mass)", "SVM Linear (Mass)", "SVM Radial (Mass)", "Rando
m Forest (Mass)"),
	TimeElapsed = c(
		as.numeric(svmPoly_m_time_elapsed),
		as.numeric(svmLinear_m_time_elapsed),
		as.numeric(svmRadial_m_time_elapsed),
		as.numeric(RF_m_time_elapsed)
	)
)

# Save the data frame as a CSV file
write.csv(time_elapsed_data_m, "temp/test_time_elapsed_data_373_m.csv", row.names =
FALSE)

# Print the table
print(time_elapsed_data_m)

mass_predictions <- cbind(svmPoly_adan_m,svmLinear_adan_m,svmRadial_adan_m, RF_
adan_m)

act_pred_mass <- cbind(original_single$File.Name, mass_predictions)
colnames(act_pred_mass) <- c("sample_id", "svmPoly", "svmLinear", "svmRadial", "Rand
om Forest")

write.csv(act_pred_mass, "temp/test_model_predicted_mass_nav.csv", row.names = FALS
E)
```

```
# Load required libraries
#library(rstan)
#library(ggplot2)

# Define the Stan model with updated prior distributions for mu and sigma
stan_model_mass <- "
data {
 int<lower=0> N;       // Number of observations
 vector[N] y;          // Data vector
}

parameters {
 real<lower=0> mu; // mu parameter of normal distribution
 real<lower=0> sigma; // sigma parameter normal distribution
}

model {
 // Prior distributions for mu and sigma
 mu ~ normal(226.147528, 8.439615); // mu parameter prior
 sigma ~ gamma(268.103048, 2.469385); //normal(108.57076, 6.63074); // sigma parameter
prior

 // Likelihood
 y ~ normal(mu, sigma); // Likelihood function
}

generated quantities {
  real prob_below_thresh;  // Probability of posterior below threshold
  real prob_within_thresh; // Probability of posterior within threshold
  real prob_above_thresh;  // Probability of posterior above threshold

  // Calculate probabilities
  prob_below_thresh = normal_cdf(226 - 2*5, mu, sigma/sqrt(166));          // Below threshol
d
  prob_within_thresh = normal_cdf(226 + 2*5, mu, sigma/sqrt(166)) - normal_cdf(226 - 2*5
, mu, sigma/sqrt(166)); // Within threshold
  prob_above_thresh = 1 - normal_cdf(226 + 2*5, mu, sigma/sqrt(166));        // Above thresh
old
}
"

# Generate some example data
set.seed(123)
```

```r
y <- read.csv("temp/test_model_predicted_mass_nav.csv")
y <- y$Random.Forest  # Navrongo only
N <- length(y)

# Prepare data list
data_list <- list(N = N, y = y)

# Compile the Stan model
#compiled_model <- stan_model(model_code = stan_model_mass)

# Save the compiled Stan model to a file
#saveRDS(compiled_model, file = "stan/compiled_model_mass.stan")

# Load the compiled Stan model from the file
compiled_model <- readRDS("stan/compiled_model_mass.stan")

# Fit the model to the data
fit <- sampling(compiled_model, data = data_list, chains = 4)

# Extract posterior samples
posterior_samples <- extract(fit)

min_value <- min(226 - 4*8, mean(posterior_samples$mu) - 4*8)
max_value <- max(226 + 4*8, mean(posterior_samples$mu) + 4*8)

# Generate prior distribution
x <- seq(min_value, max_value, length.out = 100)
prior <- dnorm(x, mean = 226.147528, sd = 8.439615)
prior <- prior / max(prior)

# Generate posterior distribution
posterior <- dnorm(x, mean = mean(posterior_samples$mu), sd = mean(posterior_samples
$sigma)/sqrt(166))
posterior <- posterior/ max(posterior)

# Generate likelihood distribution
likelihood_unnormalized <- prior * posterior
likelihood <- likelihood_unnormalized / max(likelihood_unnormalized)

# Plot using ggplot2
df <- data.frame(x = x, prior = prior, posterior = posterior, likelihood = likelihood)

# Plot using ggplot2 with thresholds
mp <- ggplot(df, aes(x)) +
      geom_line(aes(y = prior, color = "Prior")) +
```

```
        geom_line(aes(y = posterior, color = "Posterior")) +
        #geom_line(aes(y = likelihood, color = Likelihood)) +
        geom_vline(xintercept = c(226 - 2*5, 226 + 2*5),
                   linetype = "dashed", color = "red") +
        labs(title = "",
             x = "(a)   mu mass (g)", y = "Density") +
        scale_color_manual(name = "Distribution",
                           values = c(Prior = "red", Posterior = "blue", Likelihood = "green")) +
        theme_minimal()

    mp
    mp.fit <- fit
    # posterior_samples$prob_below_thresh+posterior_samples$prob_within_thresh+posterio
r_samples$prob_above_thresh

    # After all computations are done, prepare the result object
    result <- list(data = df, x = df$mass, y = df$predicted_mass, fit = mp.fit, plot = mp)

    return(result)
}

run_density_model <- function(original_single) {
    # Your density model code here
    # Rest of your function code
    # Load the trained volume model using the load function
    load("r_ml/volume_model_svmPoly.RData")
    load("r_ml/volume_model_svmLinear.RData")
    load("r_ml/volume_model_svmRadial.RData")
    load("r_ml/volume_model_rf.RData")


    # Read data
    #original_single <- read.csv("temp/output_objects.csv")
    #original_single <- original_single[original_single$Volume1 != 0 &
    #                                   original_single$Count_expected == 1 &
    #                                   original_single$Transformation == "", ]
    o_s <- original_single
    original_single <- original_single[order(original_single$File.Name),]


    adan <- original_single

    #adan<- adan[
    #    adan$Area >= 20000 &
    #        adan$Area <= 230000 &
```

```
#              adan$Field == "nav" &
#              adan$Class.Name != "Unknown",
#
#]

# FUNCTIONS
# Function to extract centroid coordinates
extract_centroid <- function(centroid_str) {
      coordinates <- as.numeric(unlist(strsplit(gsub("[\\(\\)]", "", centroid_str), ",")))

      # Check if there are at least 3 elements in coordinates
      if (length(coordinates) >= 3) {
            return(list(centroid_id = coordinates[1], centroid_x = coordinates[2], centroid_y
= coordinates[3]))
      } else {
            return(list(centroid_id = NA, centroid_x = NA, centroid_y = NA))  # Return NA
for all values if there are not enough elements
      }
}

# Function to extract bounding box coordinates
extract_bounding_box <- function(bbox_str) {
      coordinates <- as.numeric(unlist(strsplit(gsub("[\\(\\)]", "", bbox_str), ",")))

      # Check if there are at least 6 elements in coordinates
      if (length(coordinates) >= 6) {
            return(list(
                  #bb_id_1 = coordinates[1],
                  bb_x_min = coordinates[2],
                  bb_y_min = coordinates[3],
                  #bb_id_2 = coordinates[4],
                  bb_y_max = coordinates[5],
                  bb_x_min = coordinates[6]
            ))
      } else {
            return(list(
                  #bb_id_1 = NA, bb_id_2 = NA,
                  bb_x_min = NA, bb_y_min = NA,
                  bb_x_max = NA, bb_y_max = NA
            ))  # Return NA for all values if there are not enough elements
      }
}

  # Function to compute area
compute_area <- function(tuple_str) {
```

```
        bounding_box <- as.numeric(unlist(strsplit(gsub("[\\(\\)]", "", tuple_str), ",")))

        # Check if there are at least 6 elements in bounding_box
        if (length(bounding_box) >= 6) {
            height <- bounding_box[5] - bounding_box[2]
            width <- bounding_box[6] - bounding_box[3]
            area <- height * width
            return(list(bb_height = height, bb_width = width, bb_area = area))
        } else {
            return(list(bb_height = NA, bb_width = NA, bb_area = NA))  # Return NA for al
l values if there are not enough elements
        }
    }

    # Apply the function and create a new data frame for centroid coordinates
    centroid_df <- do.call(rbind, lapply(adan$Centroid, extract_centroid))
    colnames(centroid_df) <- c("centroid_id", "centroid_x", "centroid_y")

    # Merge the new data frame with the original data frame
    adan <- cbind(adan, centroid_df)

    # Apply the function and create a new data frame for bounding box coordinates
    bbox_df <- do.call(rbind, lapply(adan$BoundingBox, extract_bounding_box))
    colnames(bbox_df) <- c("bb_x_min", "bb_y_min", "bb_x_max", "bb_y_max")

    # Merge the new data frame with the original data frame
    adan <- cbind(adan, bbox_df)

    # Apply the function and create a new data frame for height, width, and area
    cbox_df <- do.call(rbind, lapply(adan$BoundingBox, compute_area))
    colnames(cbox_df) <- c("bb_height", "bb_width", "bb_area")


    # Merge the new data frame with the original data frame
    adan <- cbind(adan, cbox_df)
    adan <- adan[ , -c(1,2,3,5,6,7,10,11)]

    # Columns to convert
    columns_to_convert <- c('centroid_x',
                  'centroid_y',
                  'bb_x_min',
                  'bb_x_max',
                  'bb_y_min',
                  'bb_y_max',
                  'bb_area',
```

```
                        'bb_height',
                        'bb_width'
    )

    # Convert each column to numeric
    adan[, columns_to_convert] <- lapply(adan[, columns_to_convert], function(x) as.numeri
c(unlist(x)))
    # Volume Estimate
    start_time <- Sys.time()
    svmPoly_adan_v <- predict(volume_model_svmPoly, adan)
    end_time <- Sys.time()
    svmPoly_v_time_elapsed <- end_time - start_time
    start_time <- Sys.time()
    svmLinear_adan_v <- predict(volume_model_svmLinear, adan)
    end_time <- Sys.time()
    svmLinear_v_time_elapsed <- end_time - start_time
    start_time <- Sys.time()
    svmRadial_adan_v <- predict(volume_model_svmRadial, adan)
    end_time <- Sys.time()
    svmRadial_v_time_elapsed <- end_time - start_time
     start_time <- Sys.time()
    RF_adan_v <- predict(volume_model_rf, adan)
    end_time <- Sys.time()
    RF_v_time_elapsed <- end_time - start_time
    # Creating a data frame to tabulate time elapsed
    time_elapsed_data <- data.frame(
        Model = c("SVM Poly (Volume)", "SVM Linear (Volume)", "SVM Radial (Volume)",
"Random Forest (Volume)"),
        TimeElapsed = c(
            as.numeric(svmPoly_v_time_elapsed),
            as.numeric(svmLinear_v_time_elapsed),
            as.numeric(svmRadial_v_time_elapsed),
            as.numeric(RF_v_time_elapsed)
        )
    )
    # Save the data frame as a CSV file
    write.csv(time_elapsed_data, "temp/test_time_elapsed_data_373.csv", row.names = FALS
E)

    # Print the table
    print(time_elapsed_data)

    volume_predictions <- cbind(svmPoly_adan_v, svmLinear_adan_v,svmRadial_adan_v, RF
_adan_v)
```

```
act_pred_vol <- cbind(original_single$File.Name, volume_predictions)
colnames(act_pred_vol) <- c("sample_id", "svmPoly", "svmLinear", "svmRadial", "Rando
m Forest")

write.csv(act_pred_vol, "temp/test_model_predicted_volumes_nav.csv", row.names = FAL
SE)


# Load the trained mass model using the load function
load( "r_ml/weight_model_svmPoly.RData")
load("r_ml/weight_model_svmLinear.RData")
load("r_ml/weight_model_svmRadial.RData")
load("r_ml/weight_model_rf.RData")
# Read data
#original_single <- read.csv("temp/output_objects.csv")
#original_single <- original_single[original_single$Volume1 != 0 &
#                                   original_single$Count_expected == 1 &
#                                   original_single$Transformation == "", ]
original_single <- o_s
original_single <- original_single[order(original_single$File.Name),]
adan <- original_single

# Apply the function and create a new data frame for centroid coordinates
centroid_df <- do.call(rbind, lapply(adan$Centroid, extract_centroid))
colnames(centroid_df) <- c("centroid_id", "centroid_x", "centroid_y")

# Merge the new data frame with the original data frame
adan <- cbind(adan, centroid_df)


# Apply the function and create a new data frame for bounding box coordinates
bbox_df <- do.call(rbind, lapply(adan$BoundingBox, extract_bounding_box))
colnames(bbox_df) <- c("bb_x_min", "bb_y_min", "bb_x_max", "bb_y_max")

# Merge the new data frame with the original data frame
adan <- cbind(adan, bbox_df)


# Apply the function and create a new data frame for height, width, and area
cbox_df <- do.call(rbind, lapply(adan$BoundingBox, compute_area))
colnames(cbox_df) <- c("bb_height", "bb_width", "bb_area")

# Merge the new data frame with the original data frame
adan <- cbind(adan, cbox_df)
adan <- adan[ , -c(1,2,3,5,6,7,10,11)]
```

```
# Columns to convert
columns_to_convert <- c('centroid_x',
                        'centroid_y',
                        'bb_x_min',
                        'bb_x_max',
                        'bb_y_min',
                        'bb_y_max',
                        'bb_area',
                        'bb_height',
                        'bb_width'
)

# Convert each column to numeric
adan[, columns_to_convert] <- lapply(adan[, columns_to_convert], function(x) as.numeri
c(unlist(x)))
# Mass Estimate
start_time <- Sys.time()
svmPoly_adan_m <- predict(weight_model_svmPoly, adan)
end_time <- Sys.time()
svmPoly_m_time_elapsed <- end_time - start_time

start_time <- Sys.time()
svmLinear_adan_m <- predict(weight_model_svmLinear, adan)
end_time <- Sys.time()
svmLinear_m_time_elapsed <- end_time - start_time

start_time <- Sys.time()
svmRadial_adan_m <- predict(weight_model_svmRadial, adan)
end_time <- Sys.time()
svmRadial_m_time_elapsed <- end_time - start_time

start_time <- Sys.time()
RF_adan_m <- predict(weight_model_rf, adan)
end_time <- Sys.time()
RF_m_time_elapsed <- end_time - start_time

# Creating a data frame to tabulate time elapsed
time_elapsed_data_m <- data.frame(
  Model = c("SVM Poly (Mass)", "SVM Linear (Mass)", "SVM Radial (Mass)", "Rando
m Forest (Mass)"),
  TimeElapsed = c(
    as.numeric(svmPoly_m_time_elapsed),
    as.numeric(svmLinear_m_time_elapsed),
    as.numeric(svmRadial_m_time_elapsed),
```

```
            as.numeric(RF_m_time_elapsed)
        )
    )

    # Save the data frame as a CSV file
    write.csv(time_elapsed_data_m, "test_time_elapsed_data_373_m.csv", row.names = FALS
E)
    # Print the table
    print(time_elapsed_data_m)

    mass_predictions <- cbind(svmPoly_adan_m,svmLinear_adan_m,svmRadial_adan_m, RF_
adan_m)

    act_pred_mass <- cbind(original_single$File.Name, mass_predictions)
    colnames(act_pred_mass) <- c("sample_id", "svmPoly", "svmLinear", "svmRadial", "Rand
om Forest")

    write.csv(act_pred_mass, "temp/test_model_predicted_mass_nav.csv", row.names = FALS
E)
    # Load packages
    #library(rstan)
    #library(ggplot2)

    # Define the Stan model
    stan_model_density <- "
    data {
     int<lower=0> N;       // Number of observations
     vector[N] y;          // Data vector
    }

    parameters {
     real<lower=0> mu; // mu parameter of normal distribution
     real<lower=0> sigma; // sigma parameter of normal distribution
    }

    model {
     // Prior distributions for mu and sigma
     mu ~ normal(0.339665715, 0.004903895); // mu parameter prior
     sigma ~ lognormal(-2.7875760, 0.1623906); // normal(0.06238703, 0.01016742); // sigma
parameter prior

     // Likelihood
     y ~ normal(mu, sigma); // Likelihood function
    }
```

```
generated quantities {
  real prob_below_thresh;  // Probability of posterior below threshold
  real prob_within_thresh; // Probability of posterior within threshold
  real prob_above_thresh;  // Probability of posterior above threshold

  // Calculate probabilities
  prob_below_thresh = normal_cdf(0.34 - 2*0.003, mu, sigma/sqrt(166));          // Below thr
eshold
  prob_within_thresh = normal_cdf(0.34 + 2*0.003, mu, sigma/sqrt(166)) - normal_cdf(0.34
- 2*0.003, mu, sigma/sqrt(166)); // Within threshold
  prob_above_thresh = 1 - normal_cdf(0.34 + 2*0.003, mu, sigma/sqrt(166));        // Above t
hreshold
}
"

# Load data
set.seed(123)

y <- read.csv("temp/test_model_predicted_volumes_nav.csv")
y <- y$Random.Forest #
yv <- y

y <- read.csv("temp/test_model_predicted_mass_nav.csv")
y <- y$Random.Forest #
ym <- y

y <- ym/yv # Navrongo only

N <- length(y)

# Prepare data list
data_list <- list(N = N, y = y)

# Compile the Stan model
#compiled_model <- stan_model(model_code = stan_model_density)

# Save the compiled Stan model to a file
#saveRDS(compiled_model, file = "stan/compiled_model_density.stan")

# Load the compiled Stan model from the file
compiled_model <- readRDS("stan/compiled_model_density.stan")

# Fit the model to the data
fit <- sampling(compiled_model, data = data_list, chains = 4)
```

```
# Extract posterior samples
posterior_samples <- extract(fit)

min_value <- min(0.339665715 - 4*0.004903895, mean(posterior_samples$mu) - 4*0.004
903895)
max_value <- max(0.339665715 + 4*0.004903895, mean(posterior_samples$mu) + 4*0.00
4903895)


# Generate prior distribution
x <- seq(min_value, max_value, length.out = 100)
prior <- dnorm(x, mean = 0.339665715, sd = 0.004903895)
prior <- prior / max(prior)

# Generate posterior distribution
posterior <- dnorm(x, mean = mean(posterior_samples$mu), sd = mean(posterior_samples
$sigma)/sqrt(166))
posterior <- posterior / max(posterior)

# Generate likelihood distribution
likelihood_unnormalized <- prior * posterior
likelihood <- likelihood_unnormalized / max(likelihood_unnormalized)

# Plot using ggplot2
df <- data.frame(x = x, prior = prior, posterior = posterior, likelihood = likelihood)

# Plot using ggplot2 with thresholds
dp <- ggplot(df, aes(x)) +
  geom_line(aes(y = prior, color = "Prior")) +
  geom_line(aes(y = posterior, color = "Posterior")) +
  #geom_line(aes(y = likelihood, color = "Likelihood")) +
  geom_vline(xintercept = c(0.34 - 2*0.003, 0.34 + 2*0.003),
        linetype = "dashed", color = "red") +
  labs(title = "",
     x = "(c)   mu density (g/cm³)", y = "Density") +
  scale_color_manual(name = "Distribution",
            values = c(Prior = "red", Posterior = "blue", Likelihood = "green")) +
  theme_minimal()

dp
dp.fit <- fit
# posterior_samples$prob_below_thresh+posterior_samples$prob_within_thresh+posterio
r_samples$prob_above_thresh

# After all computations are done, prepare the result object
```

```
    result <- list(data = df, x = df$density, y = df$predicted_density, fit = dp.fit, plot = dp)

    return(result)
}
# Run the application
shinyApp(ui = ui, server = server)
```